

DENSITY MATRIX RENORMALIZATION GROUP STUDIES  
OF STRONGLY CORRELATED SYSTEMS IN LOW  
DIMENSIONS

by  
Yixuan Huang

A dissertation submitted to the Department of Physics,  
College of Natural Sciences and Mathematics  
in partial fulfillment of the requirements for the degree of

Doctor of Philosophy  
in Physics

Chair of Committee: Chin-Sen Ting

Committee Member: Pavan Hosur

Committee Member: Zhifeng Ren

Committee Member: Kevin E. Bassler

Committee Member: Nikolaos V. Tsekos

University of Houston  
May 2020

Copyright 2020, Yixuan Huang

## ACKNOWLEDGMENTS

I would like to thank my advisor Prof. C.S. Ting for providing me the opportunity to work on numerical methods for strongly correlated systems, and the continuous support of my study, research, patience, and motivation which is an excellence guidance throughout my research. I would also like to thank Prof. D.N. Sheng for the numerous and fruitful discussions about the implementations of numerical algorithms, the physical meaning of the numerical observables, and their relations to the real materials and experiments. My gratitude also goes to Prof. Pavan Hosur who has helped me a lot in understanding the leading edge knowledge of the many-body physics. He has provided me with lots of insights in the analytical approaches to different physical problems. Also, I would like to thank my other dissertation committee members, Prof. Kevin E. Bassler, Prof. Zhifeng Ren, and Prof. Nikolaos V. Tsekos for the professional comments and advice from their point of view, which helps me a lot in improving my research. At last, I would like to thank my friends and family for supporting me throughout my Ph.D. program and the helpful discussions on the research-related issues.

## ABSTRACT

The density matrix renormalization group method (DMRG) is a powerful numerical method for strongly correlated systems, which often cannot be solved analytically either by the mean field approach or through perturbation. The DMRG was originally proposed as an iterative search of the ground state in one dimension. With more researchers involved in the development of the algorithms based on DMRG, now it has become an optimized unbiased method for the strongly correlated problems. Compared with other numerical methods, the DMRG has one drawback that it cannot handle the lattices in three dimension. However, many materials with layered structure like the high-Tc superconductors can be approximated by the two dimensional lattice, and some models can be simplified or transformed into lower dimensions without losing information under certain situations. Here we have studied models of the electron systems in one dimension, and the spin systems in two dimension with large scale DMRG. For the Kondo lattice model we have found two charge-ordered phases in the doped regime which have not been found before. We also investigate the spin- $\frac{1}{2}$  XY model on the honeycomb lattice and identify a chiral spin liquid with additional chiral interactions. The chiral spin liquid has a non-trivial topological order with chiral edge states. Regarding the twisted bilayer graphene which is found experimentally to emerge a superconducting phase at low temperature, we construct an auxiliary model and provide insights to the exotic ferromagnetic Mott state that may exists in the twisted bilayer graphene. We also try to study the Kondo impurity problem in the presence of a superconductor and discuss the potential models with realistic interactions for future studies.

# TABLE OF CONTENTS

<b>ACKNOWLEDGMENTS</b> . . . . .	iii
<b>ABSTRACT</b> . . . . .	iv
<b>LIST OF FIGURES</b> . . . . .	xi
<b>1 Introduction</b> . . . . .	<b>1</b>
1.1 Condensed matter physics and strongly correlated systems . . . . .	1
1.2 Numerical and analytical methods . . . . .	3
1.3 Fundamental lattice models . . . . .	7
1.3.1 The Hubbard model . . . . .	7
1.3.2 The Heisenberg model . . . . .	9
1.3.3 The Kondo model . . . . .	11
<b>2 Density Matrix Renormalization Group Method</b> . . . . .	<b>14</b>
2.1 Introduction . . . . .	14
2.2 Finite temperature DMRG . . . . .	18
2.3 DMRG in matrix product state . . . . .	21
2.4 Other methods based on DMRG . . . . .	23
<b>3 The Kondo lattice model</b> . . . . .	<b>25</b>
3.1 Introduction . . . . .	25
3.2 One dimensional phase diagram . . . . .	26
3.3 Charge density wave . . . . .	30
3.4 Dimer order and bond order wave . . . . .	40
<b>4 The spin-<math>\frac{1}{2}</math> XY honeycomb model</b> . . . . .	<b>47</b>
4.1 Topological phase of matter . . . . .	47
4.2 Analytical prediction of the chiral spin liquid . . . . .	49
4.3 Global phase diagram . . . . .	51
4.4 Numerical evidence of the chiral spin liquid . . . . .	59
<b>5 The magic angle physics in twisted bilayer graphene</b> . . . . .	<b>66</b>
5.1 Constructing an effective two-leg ladder . . . . .	66
5.2 Ferromagnetic Mott state . . . . .	68

<b>6</b>	<b>The Kondo impurity in a superconductor</b>	<b>77</b>
6.1	Kondo screening in a superconductor . . . . .	77
6.2	Kondo singlet state and doublet state . . . . .	81
<b>7</b>	<b>Summary</b>	<b>87</b>
	<b>Bibliography</b>	<b>92</b>

## LIST OF FIGURES

1.1	The crystal structure of $Per_2[M(mnt)_2]$ . The conducting Per stack has a much larger resistivity within the plane than perpendicular to the plane, making it an effective one dimensional conducting chain. . . . .	2
1.2	Some common lattice configurations in two dimensions. . . . .	4
1.3	The magnetic susceptibility for various temperatures in one dimensional Heisenberg model. The numerical results is obtained by density matrix renormalization group method. . . . .	10
1.4	The demonstration of the Kondo insulator. The finite energy needed to break the singlet state and move an electron leads to an insulating ground state. .	12
2.1	The whole system in DMRG is made of the system block and the environment block, and each time there is one site added to each block. . . . .	16
2.2	The schematic graph for the sweeping process in finite size DMRG algorithm, where 'Sys' refers to the system block and 'Env' refers to the environment block.	18
2.3	The schematic graph of the interactions in Trotter decomposition. . . . .	20
2.4	The schematic representation of the matrix product state and matrix product operator. . . . .	22
3.1	The uniform spin susceptibility of the one dimensional Kondo lattice model at half filling for various temperatures in Figure 3.1(a). Figure 3.1(b) shows the same susceptibility for the temperatures close to zero. The results are obtained at $J = 1$ . . . . .	27
3.2	The ground state phase diagram of the one dimensional Kondo lattice model. The ferromagnetic (paramagnetic) state is represented by the blue (white) regime, and the solid line at $n = 1$ is the Kondo insulator. The two dashed lines at $n = 0.5$ and $n = 0.75$ indicate the commensurate dimer phase and charge density wave phase, respectively. . . . .	28

3.3	(a) is the electron density at $J = 0.9, L = 160, n = \frac{3}{4}$ . Only half of the lattice is shown. (b) is Fourier transform of the density oscillation in (a). The dominant peak shows up at $k = \frac{\pi}{2}$ . The inset of (b) shows the intensity of the $k = \frac{\pi}{2}$ peak divided by the length. (c) is the $J$ dependence of the oscillation amplitude in the middle after finite size extrapolation. The extrapolation in (d) is conducted in this way. If the fitting agrees well with the power decay of the Friedel oscillation in TLL then the order parameter is considered zero when $L \rightarrow \infty$ , otherwise we use a least-square fit to the second order of polynomials in $1/L$ . For $J$ close to the transition we find it better to fit to $1/\sqrt{L}$ as the similar scaling in TLL. . . . .	32
3.4	(a) is the log-log plot of the Friedel oscillation amplitude in the middle of various lengths. The Luttinger parameter $k_L$ is determined by the <i>slope</i> = $-2k_L$ . The error of $k_L$ is given by the standard deviation of the least square fit. The Luttinger parameter decreases as we lower $J$ into the weak coupling region, which agrees with previous studies. For $J = 1$ it cannot be linearly fit, indicating the onset of CDW. (b) is the finite size extrapolation of the charge gap at $n = \frac{3}{4}$ . Four examples of $J$ are given for the least-square fit. The inset of (b) shows the extrapolated charge gap for various $J$ . . . . .	34
3.5	The finite size extrapolation of the charge gap at $n = \frac{1}{4}$ . . . . .	36
3.6	The nearest-neighbor (Figure 3.6(a)) and long range dimer-dimer (Figure 3.6(b)) correlation of the localized spins at $J = 0.9, L = 208, n = \frac{3}{4}$ . In (a) the average correlation is around -2.0, which is $L$ independent. The incommensurate oscillation refers to the upper bound in the middle with $k = \frac{\pi}{L}$ . The amplitude of the incommensurate oscillations has almost no dependence of the lattice length. The inset of (a) shows the dominant oscillation of the correlation with a period of 4, which is the same period as the CDW. In (b) we calculate the correlation at $x = 29$ to minimize the boundary effect. The plot uses logarithmic scale on both axis in order to identify the decay mode. The dimer-dimer correlation also has an oscillation period of 4. The 4 color dashed lines are nothing but the correlation of every four points connected, because they each has a different pattern. The correlation functions of the TLL are not shown here as they have monotonic power law decays which agrees with the bosonization theory. . . . .	38
3.7	The dimer order (a) and bond order wave (b) at $n = 0.5, J = 0.6$ obtained by the finite size lattice of $L = 112$ . Only half of the lattice is shown. . . . .	40
3.8	(a) refers to the finite size scaling of the dimer order for various $J$ . We use a least-square fit to the second order of polynomials in $1/L$ . The order parameter of the dimer phase and bond order wave phase is plotted along with the charge gap in (b). These quantities are obtained after finite size scaling similar to (a). . . . .	42
3.9	The entanglement entropy at $n = 0.5, J = 0.6$ obtained by the finite size lattice of $L = 112$ . Only half of the lattice is shown. The dash line refers to the fitting using Equation 3.7. . . . .	43

3.10	The red line in (a) refers to the spin correlations and the yellow line in (a) refers to the dimer correlations. The results are obtained on a $L = 160$ lattice with $n = 0.5$ , $J = 0.6$ and $x$ is chosen to be $\frac{L}{4}$ in order to minimize the boundary effect. (b) is the same correlations with log scale in the y-axis showing the correlation decay over distance. . . . .	44
4.1	The schematic diagram of the gap in Haldane phase. . . . .	48
4.2	The illustrating plot of the XY model Hamiltonian after Chern-Simons fermionization. The dash lines indicate a unit cell. . . . .	50
4.3	The schematic phase diagram of the extended XY model for $0.1 < J_2 < 0.6$ and $0 < J_\chi < 0.3$ , based on the results from cylindrical circumference of 4 unit cells. The CSL is identified in the intermediate regime. . . . .	53
4.4	(a) shows the peak value at $\Gamma$ point in the spin structure $S(q)$ at $J_2 = 0.2$ for various $J_\chi$ . The inset of (a) is the spin structure of the XY-Neel order at $J_2 = 0.2$ , $J_\chi = 0.06$ , where there are clear peaks at the $\Gamma$ points in the second Brillouin zone. (b) is the $M$ point peak value at $J_2 = 0.4$ for various $J_\chi$ . The inset of (b) is the spin structure of the collinear order at $J_2 = 0.4$ , $J_\chi = 0.01$ , where the dominant peak is located at the $M$ points in the second Brillouin zone. (c) shows the antiferromagnetic order (blue line) and the scalar chiral order (red line) at $J_2 = 0.3$ for various $J_\chi$ . (d) refers to the spin correlations at $J_2 = 0.3$ for various $J_\chi$ . The phases at $J_\chi = 0.01, 0.04, 0.08$ , and $0.14(0.25)$ refer to Ising antiferromagnetic state, phase boundary, CSL, and chiral spin state respectively. The $x_0$ is chosen away from the open boundary, and $x$ refers to the horizontal distance between the two spins. The plots above are based on finite DMRG results with $L_y = 4 \times 2$ . . . . .	55
4.5	The staggered magnetization for various lengths in the x-direction (Figure 4.5(a)) and the y-direction (Figure 4.5(b)) in the intermediate regime. The phase transition from the Ising antiferromagnetic state to the CSL is determined by the sudden drop of $ \langle S_z \rangle $ . For the smallest size in (a) ( $L_x \times L_y = 20 \times 3 \times 2$ ) and (b) ( $L_x \times L_y = 6 \times 4 \times 2$ ) we found that $ \langle S_z \rangle  = 0$ at zero $J_\chi$ limit due to finite size effect. . . . .	56
4.6	The spin structure in the chiral spin state at $J_2 = 0.2$ , $J_\chi = 0.27$ using finite size cylinder of $L_x \times L_y = 20 \times 4 \times 2$ , which peaks at the $M$ points in the second Brillouin zone. . . . .	57
4.7	The creation of the edge by cutting the infinite long cylinder in half. . . . .	58
4.8	The matrix product state representations of the infinite long cylindrical system. . . . .	59

4.9	The ES for the spinon ground state (a) and the vacuum ground state (b) in the CSL phase at $J_2 = 0.26, J_\chi = 0.09$ , and the ES in the chiral spin state (c) at $J_2 = 0.26, J_\chi = 0.2$ with different spin sectors. The spectrum is calculated using infinite DMRG with $L_y = 6 \times 2$ . The $\lambda_i$ refers to the eigenvalues of the reduced density matrix, and the $k_y$ has an increasement of $\frac{2\pi}{L_y}$ . The quasi-degenerate eigenvalues are labeled by the number below each momentum. Each spin sector is separated with the help of total $S_z$ conservation implemented in the algorithm. . . . .	61
4.10	The entanglement spectrum in CSL at $J_\chi = 0.09$ (Figure 4.10(a)), boundary at $J_\chi = 0.13$ (Figure 4.10(b)), and the chiral spin state at $J_\chi = 0.2$ (Figure 4.10(c)). All three plots are obtained at $J_2 = 0.26$ . The dash red lines are guide to the eye. . . . .	62
4.11	(a) refers to the spin structure in the CSL phase at $J_2 = 0.2, J_\chi = 0.16$ where there is no peak as opposed to other magnetic phases. This result is based on the cluster of $20 \times 4 \times 2$ . (b) refers to the spin structure peaks with fixed $k_x = -\frac{2\pi}{\sqrt{3}}$ of various parameters. The blue and red lines are obtained in the chiral spin state with clusters of $20 \times 4 \times 2$ and $30 \times 6 \times 2$ , respectively. The magnitude of the peak increases as the cluster size increases. The black and grey lines are obtained in the CSL with the same two clusters, where there is no significant peak. (c) refers to the finite size scaling of the spin gap on the torus geometry with clusters of $3 \times 3 \times 2, 4 \times 3 \times 2, 4 \times 4 \times 2, 6 \times 4 \times 2$ , and $8 \times 5 \times 2$ . (d) refers to the entanglement entropy with various clusters on finite cylinders in the CSL phase. The $x$ here denotes the distance of the cut in the x direction. All of the results are obtained at $J_2 = 0.2$ . . . . .	64
5.1	The Fourier transform of the electron density at various fillings, with the dominant peaks remain at $k = \frac{2\pi}{6}$ . The results are obtained at $L = 144$ in the quasi-flat band regime. . . . .	69
5.2	(a) refers to the electron density in real space. The electron density has a robust oscillation pattern away from the boundary with the amplitude $\approx 0.03$ . Only half of the lattice is shown. (b) refers to the charge gap for various $U$ after the finite-size scaling. The charge gap becomes finite for $U > 0.2$ . (c) refers to the intra-chain spin correlations. The correlations are the same for either chain. Here $x = \frac{L}{4}$ is chosen to be away from the boundary to minimize the finite size effect. (d) refers to the inter-chain spin correlations with only half of the lattice shown. All of the results above are obtained at $n = \frac{1}{2J}$ . . . . .	71
5.3	The finite-size scaling of the charge gap for various $U$ in the quasi-flat band regime. We have used a least-square fit to the third order of polynomials in $1/L$ . Similar fittings are used in the extrapolation of the charge gap for various $\gamma_0$ . . . . .	72

5.4	(a) refers to the intra-chain spin correlations for various $\gamma_0$ where $x = \frac{L}{4}$ is chosen to be away from the boundary. The correlations are the same for either chain. The inset shows the correlations in the uncoupled limit. (b) refers to the spin structure for various $\gamma_0$ (c) refers to the inter-chain spin correlations for various $\gamma_0$ , obtained with the finite length of $L = 144$ . Only half of the lattice is shown. (d) refers to the charge gap for various $\gamma_0$ after the finite-size scaling. All of the results above are obtained at $U = 0.4$ and $n = \frac{1}{2J}$ . . . . .	74
5.5	The intra-chain spin correlations with next-nearest-neighbor Coulomb interactions, obtained by the system length of $L = 144$ . The correlation is calculate at $x = \frac{L}{4}$ in order to minimize the effect of the open boundary, and the correlation is the same for either chain. . . . .	76
6.1	(a) refers to the local spin value for various $J$ , (b) refers to the total electron spins versus $J$ . . . . .	79
6.2	The ground state energy of the singlet state and doublet state obtained by DMRG, which is represented by the purple and green line, respectively. . . .	81
6.3	The impurity magnetic moment square for various $J$ . . . . .	82
6.4	The correlations between the impurity spin and the electron spins in the singlet ground state (yellow line) and the doublet ground state (blue line) for various $J$ . . . . .	83
6.5	The superconducting order parameter without magnetic impurity spin for various onsite attractive interactions. . . . .	84
6.6	The superconducting order parameter with a magnetic impurity spin in the middle ( $i = 51$ ) for various onsite attractive interactions. . . . .	86

# Chapter 1

## Introduction

### 1.1 Condensed matter physics and strongly correlated systems

In condensed matter physics people study various states of matter. These states include insulating state, metallic state, superconducting state, quantum hall states and so on. Most matter involves large amount of atoms and particles. Although the behavior of every single particle is governed by the physical laws like quantum mechanics and statistical mechanics, together with the strong interactions between them they could form a new phase that is beyond single particle physics [1].

Starting from the microscopic view, every material contains nuclei that have positive charges, and electrons that have negative charges. The Hamiltonian of the whole system includes the electromagnetic potential energy and the kinetic energy. The most difficulty of solving the Hamiltonian is the "exponential wall": As the number of particles or variables increases, the complexity or the number of possible states increases exponentially. Even with the help of the most advanced computers in the world the system with more than

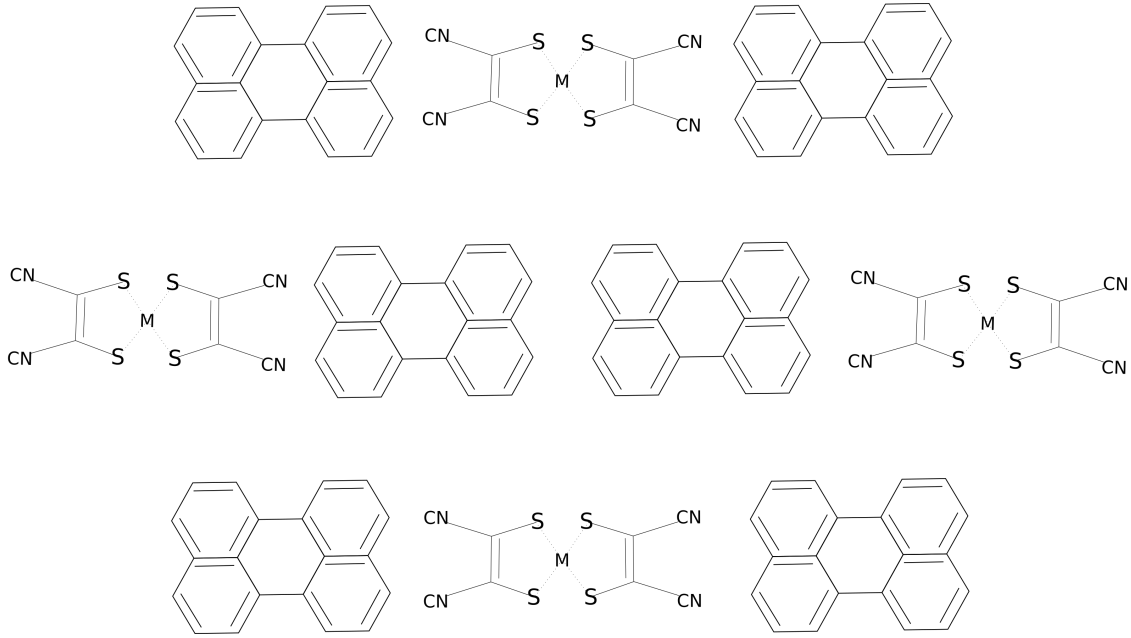


Figure 1.1: The crystal structure of  $Per_2[M(mnt)_2]$ . The conducting Per stack has a much larger resistivity within the plane than perpendicular to the plane, making it an effective one dimensional conducting chain.

thirty atoms can not be solved exactly, which is a very small number compared to the  $10^{23}$  atoms in real materials.

For most solid we could consider the atoms as a periodic lattice plus a small vibration about the lattice point. The electron's wave function in a periodic lattice could be described by the band theory. The band theory has predicted conductors, semiconductors, and insulators successfully. It also explains many electronic transport properties such as conductivity and magnetic susceptibility.

However, the band theory has neglected the Coulomb interactions between electrons, thus is not suitable for materials with strong interactions. With the Fermi liquid theory some interacting systems could be explained, but nowadays more and more states beyond the Fermi liquid theory have been found in nature. In one dimension, the interactions between electrons lead to a Tomonaga-Luttinger liquid [2], which is different from the Fermi liquid. Other exotic states include the Mott insulator, high temperature superconductor,

heavy Fermion materials, and so on. The common characteristic of those states is the strong correlations between the electrons, which is why the system is called strongly correlated systems.

The strongly correlated systems are studied using the lattice models which is based on a discrete space. The lattice in the solid is automatically given by the atoms because the atoms will stay in the equilibrium position in real space if we neglect the small vibrations. Even though almost all materials are three dimensional in nature, the interactions in some dimensions could be much weaker than other dimensions, thus resulting in an effective lower dimensional system. As an example given in Figure 1.1, This organic compound  $Per_2[M(mnt)_2]$  [3] is often treated as quasi-one dimensional material because the distance between the stack in the other two dimensions are much longer, thus the interactions are much weaker.

In one dimension the lattice is either an open chain or a closed loop, while in two dimensions there could be various types of lattices such as triangle lattice, honeycomb lattice, kagome lattice, and so on, as illustrated by Figure 1.2. The same Hamiltonian could have completely different physics on different geometries.

In three dimensions the lattice could become more complicated. Physicists seek to understand the physical properties of matter with minimal model by capturing the important role play of different interactions and lattice types. Most of the lattice models can not be solved exactly, and because of the strong interactions between electrons, we can not use perturbation theory to treat it as an effective one particle problem.

## 1.2 Numerical and analytical methods

In most cases, there are two basic routes to approximate the many-body wave functions of the complicated lattice model in general. The first one is by mean field theory, which

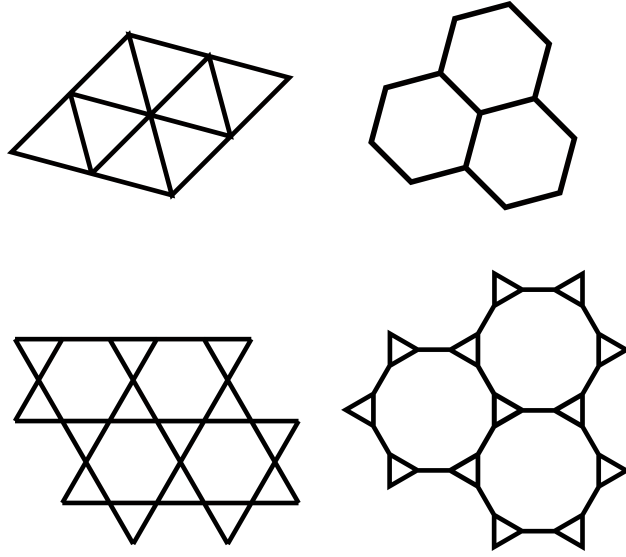


Figure 1.2: Some common lattice configurations in two dimensions.

represents the interactions by the mean field interactions and results in an analytical solution of the Hamiltonian. The advantage of the mean field theory is that we could have a better understanding of the physics with the analytical solution, but sometimes the solution is biased and not exact. Generally for a gapped system the quantum fluctuation corrections to the mean field solutions are finite, thus giving some confidence in the validity for the gapped cases. The second way is by numerical simulation. With more powerful computers and developed numerical algorithms the strongly correlated systems could be solved with higher precision.

In some situations, an exact analytical solution of the Hamiltonian can be achieved. The exact analytical solution provides a helpful way to examine the validity of the numerical calculations. In one dimension, the Bethe ansatz method is successful in solving the basic models such as antiferromagnetic Heisenberg model and Hubbard model. Under the bosonization and Luttinger theory [2], all electronic systems in one dimension belong to the universal class of Tomonaga-Luttinger liquid. In such case, all physical properties are controlled by a single Luttinger parameter.

$$\langle \rho(r)\rho(0) \rangle = \frac{2}{(2\pi\alpha)^2} \cos(2k_F x) \left(\frac{\alpha}{r}\right)^{2K} \quad (1.1)$$

$$\langle O_{CDW}^\dagger(r)O_{CDW}(0) \rangle = \frac{e^{2ik_F x}}{2(\pi\alpha)^2} \left(\frac{\alpha}{r}\right)^{K+1} \quad (1.2)$$

The examples of the density-density correlation functions and the charge density wave correlation functions are given by Equation 1.1 and Equation 1.2, assuming the Hamiltonian has spin SU(2) symmetry. Here  $K$  refers to the Luttinger parameter. These properties provide us an efficient way to numerically calculate the Luttinger parameter of a specific Hamiltonian in one dimension, and once the Luttinger parameter is known other physical properties could be derived from Luttinger theory. In addition, the theory can help us identify the phase transitions along with the numerical results.

For systems in two or more dimensions there is hardly an exact solution in general. Instead, people use mean field theory to acquire a physical picture that is helpful in explaining some of the phenomenon, such as the slave boson method [4], and the renormalized mean field theory [5]. However, those methods are usually limited to a certain type of problem.

As the development of high performance cluster computing, the numerical algorithm has improved a lot and become the most important way to approach the strongly correlated systems. Below is the introduction of four main standard numerical methods. To these days people are still searching for new algorithms based on these methods, but the validity and accuracy of the new methods remain to be tested.

1. The exact diagonalization [6, 7]. For a finite size lattice of a given Hamiltonian, the Hamiltonian is written in the form of one large matrix. The matrix is diagonalized using iterative eigenvalue solver like the Lanczos or Davidson, and the physical observables are obtained by the eigenvalues and eigenvectors. This algorithm is applicable for any type

of Hamiltonian, but it is limited by the lattice size of 64 sites for spin systems, and even fewer for electron systems. Thus, it is hard to extrapolate the numerical results into the thermodynamic limit.

2. The density matrix renormalization group [8, 9]. This algorithm is based on the finite quantum entanglement representation of the ground state. It is developed based on the numerical renormalization group method, which tends to restrict the dimension of the Hamiltonian matrix by truncating the high energy states and acquire the ground state of a larger size lattice, or even an infinite size. Although the algorithm can be used to calculate larger size, the lattice is often restricted to one dimension or quasi-two dimensions, because quantum entanglement of the ground state is proportional to the area between two partitions. This is known as the area law. Nowadays there are other numerical algorithms based on the density matrix renormalization group method that could calculate real two dimensional systems such as the projected entangled pair states. More details of the density matrix renormalization group method will be discussed in chapter 2.

3. The quantum Monte Carlo method [10]. This approach typically provides very accurate solution to the non-frustrated interacting bosonic systems. Its advantages of being able to deal with three dimensional lattices and finite temperature has made it popular for simulating various types of systems. However, the sign problem raised by the frustrations and the anti-commutation rule of Fermionic systems makes it less accurate for certain materials like the quantum spin liquids.

4. The dynamical mean field theory [11]. Instead of trying to calculate the ground state of a many-body lattice Hamiltonian, we can map the Hamiltonian into an impurity model, and the impurity model becomes easier to solve with various techniques. The mapping of the Hamiltonian is more accurate for higher dimensions, and becomes exact in the limit of infinite dimensions. Generally for a three dimensional system, the dynamical mean field theory can

provide good predictions for the electronic properties like a phase transition between a Mott insulating state and a metallic state, but for two and one dimensional systems, it becomes less valid. Another limitation of this method is the impurity problem. We can not map the impurity model because it doesn't have the lattice symmetry.

## 1.3 Fundamental lattice models

### 1.3.1 The Hubbard model

When we consider electrons moving in a lattice, the correlations between the electrons are very important. An electron can not hop to another state if that state is already occupied by another electron because of the Pauli exclusion principle. In addition, the electron will have less tendency of hopping to the nearby site if there are electrons there because of the Coulomb repulsion. The simplest model containing Coulomb repulsive interactions between electrons is the Hubbard model. The Hamiltonian of the Hubbard model [12] for single orbit is

$$H = \sum_{i,j} \sum_{\sigma} T_{ij} c_{i\sigma}^{\dagger} c_{j\sigma} + H.c. + U \sum_i n_{i\uparrow} n_{i\downarrow} \quad (1.3)$$

The first term in the Hamiltonian is the hopping term where  $c_{i,\sigma}^{\dagger}$  refers to the creation operator of an electron on site  $i$  with spin index  $\sigma$ , and the second term describes the onsite Coulomb interactions. If we consider only nearest neighbor hopping, the hopping term  $\sum_{i,j} T_{ij}$  could be reduced to  $t \sum_{\langle i,j \rangle}$ .

In one dimension, any finite positive  $U$  will result in a Mott insulator at half filling [13]. This Mott state is a spin density wave state with a uniform electron density and a non-uniform spin density. Apart from the half filling, the system will always be metallic regardless

of the magnitude of  $U$  [14]. If we include the nearest neighbor Coulomb repulsion term  $V \sum_{\langle i,j \rangle} \sum_{\sigma\sigma'} n_{i\sigma} n_{j\sigma'}$ , the state could become insulating again [13, 15, 16]. The model that includes not only the onsite Coulomb repulsion interactions is called the extended Hubbard model. Depending on the strength and interaction type, the Mott state could be spin density wave, charge density wave, or bond order wave [17]. In the charge density wave and bond order wave state the electron density forms a standing wave like pattern. The difference between them is that the peak of the standing wave is at the site for the charge density wave, but it is in between the sites (at the bond) for the bond order wave.

Besides the Mott state, other interesting phenomenon like high Tc superconductors and topological state can also emerge from the Hubbard model. When  $U \gg t$  and the system is at less than half filling, the Hubbard model can be approximated by the t-J model [18]. The Hamiltonian of t-J model is

$$H = t \sum_{\langle i,j \rangle} \sum_{\sigma} c_{i\sigma}^{\dagger} c_{j\sigma} + H.c. + J \sum_{\langle i,j \rangle} (\vec{S}_i \cdot \vec{S}_j - \frac{n_i n_j}{4}) \quad (1.4)$$

Here  $J = \frac{4t^2}{U}$  is the antiferromagnetic interactions between nearest neighbor spins. The t-J model has become the most important model to study the cuprate based high Tc superconductors [19]. The cuprate based high Tc superconductors have layered structure that is similar to a two dimensional material. In numerical calculations, the electronic system in real two dimensional lattice still remains a challenge. For instance, with the standard density matrix renormalization group method the calculations could be done on a cylindrical geometry, with open boundary conditions in one direction and periodic boundary conditions in another. However, the circumference of the cylinder is often restricted to several lattice spacing, making it hard to extrapolate to the thermodynamic limit.

Because of the effective antiferromagnetic interactions between nearest neighbor spins, the Hubbard model could induce frustrations with frustrated lattice such as the triangle

lattice. This could lead to a quantum spin liquid phase [20] with fractional quasi-particle excitations. In the mean time, the materials with quantum-spin-liquid-like behavior are being actively searched in experiments [21].

### 1.3.2 The Heisenberg model

In the Mott region where  $U \gg t$  at half filling, the electrons are localized at each lattice point. With exactly one electron per site, the whole system could be described as an effective spin- $\frac{1}{2}$  system. The simplest effective Hamiltonian is given as

$$H = J \sum_{\langle i,j \rangle} \vec{S}_i \cdot \vec{S}_j \quad (1.5)$$

Depending of the sign of  $J$ , the model is called ferromagnetic Heisenberg model, or antiferromagnetic Heisenberg model. This model is used to study the quantum magnetism in materials. As an example in one dimension, at high temperature the system is in non-magnetic thermal equilibrium state. As temperature decreases, the magnetic susceptibility generally follows the Curie's law which is inverse proportional to the temperature. However, at zero temperature the ground state is a paramagnetic state with finite susceptibility. Using numerical calculations we could obtain the magnetic susceptibility for various temperatures as illustrated in Figure 1.3. The peak of the magnetic susceptibility shows the Curie limit.

If we extend the interactions to further neighboring sites, the competition between the interactions will lead to other kinds of state. For example, a dimer phase can be found with large next nearest neighbor interactions [22]. In two dimensional lattice, there could be stripy phase [23], xy-plane Neel order [24], plaquette valence bond order [25], and so on.

Although the model looks simple, there is no analytical solution except for the one dimension version. In addition, the extension of this Hamiltonian could result in many exotic states that remains to be the hot topic in the field.

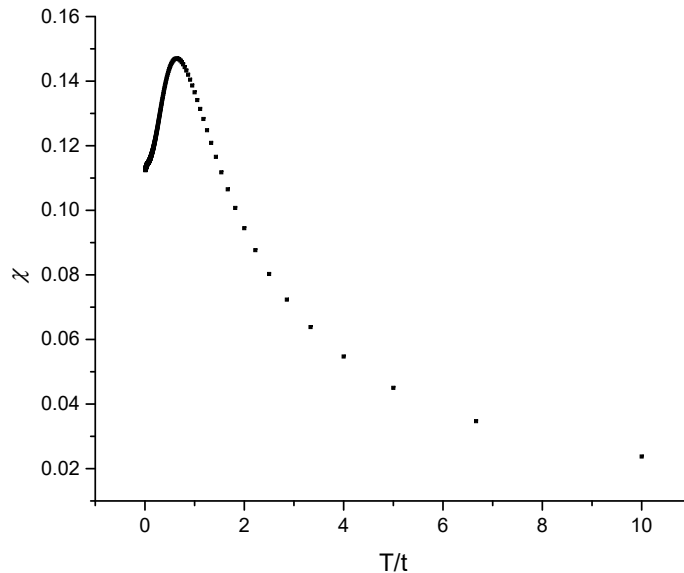


Figure 1.3: The magnetic susceptibility for various temperatures in one dimensional Heisenberg model. The numerical results is obtained by density matrix renormalization group method.

If we consider the spin to be spin-1 instead of spin- $\frac{1}{2}$ , a symmetry protected topological phase emerges which is known as the Haldane phase [26] for spin-1 chain. This topological phase can emerge for any integer number of spin, and is related to the quantum Hall effect.

For the extended Heisenberg model like including a next nearest neighbor spin interaction, if the magnitude of the interaction has opposite sign, the Hamiltonian will be frustrated. The frustration can also be achieved by putting the antiferromagnetic Heisenberg model in a frustrated lattice. Instead of the magnetic ordered state for the ground state, a quantum spin liquid state will emerge due to frustration [27]. The exotic properties [28, 29] of the quantum spin liquid are relevant to both unconventional superconductivity [30, 31, 32] and topological quantum computation [33].

Besides the Heisenberg interaction which consists of a two spin interaction, we can also get other types of spin interaction from the higher order perturbation of the Hubbard model.

In the presence of a staggered magnetic field, there could be an effective three spin chiral interaction [34] that is defined as

$$H_\chi = J_\chi \sum_{i,j,k \in \Delta} \vec{S}_i \cdot (\vec{S}_j \times \vec{S}_k) \quad (1.6)$$

The interaction could lead to a non-zero chirality that breaks the time reversal symmetry, which is essential for the topological states like chiral spin liquid. Furthermore, there could be a four spin ring exchange interaction [35] that competes with other interactions.

### 1.3.3 The Kondo model

In the study of inter-metallic elements, there are unpaired 4f or 5f electrons besides the itinerant electrons. These electrons are in the inner shell of the atoms, making them harder to contribute to the itinerant electrons. However, we could still consider them as magnetic impurities that interact with the electron spins. For the simplest case consider only one magnetic impurity that is represented by a localized spin- $\frac{1}{2}$ , the Hamiltonian is

$$\mathcal{H} = -t \sum_{\langle i,j \rangle} \sum_{\sigma} c_{i\sigma}^\dagger c_{j\sigma} + H.c. + J \vec{S}_0 \cdot \vec{s}_0 \quad (1.7)$$

The second term in the Hamiltonian describes the spin-spin interaction where  $\vec{S}_0$  denotes the localized spin- $\frac{1}{2}$  at location 0 and  $\vec{s}_0 = \frac{1}{2} \sum_{\alpha,\beta} c_{0,\alpha}^\dagger \vec{\sigma}_{\alpha,\beta} c_{0,\beta}$  (with Pauli matrices  $\vec{\sigma}$ ) the conduction electron spin.

The name of Kondo model originates from the experimental observation of an unexpected rise in resistivity of a metal at low temperature, which was explained by Kondo [36] with theoretical approaches, and later by Wilson [37] using numerical methods. More interesting phenomenon appears when we consider two or more impurities and include the interactions between them [38]. The interaction in the assumption of free electron bath can be derived

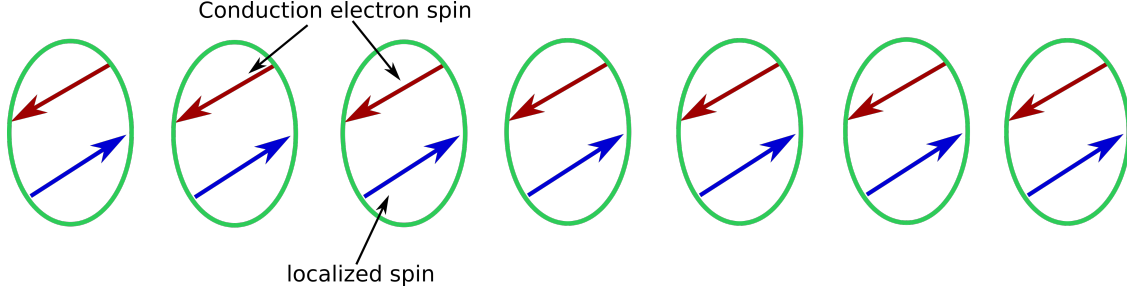


Figure 1.4: The demonstration of the Kondo insulator. The finite energy needed to break the singlet state and move an electron leads to an insulating ground state.

using perturbation theory, which is named as the RKKY interaction [39, 40, 41]. This effective interaction is long-ranged between the localized spins, with oscillations between ferromagnetic and antiferromagnetic coupling.

If the compound contains lots of rare earth elements that have magnetic impurities, the interactions will lead to significantly larger free electron mass, which is called the heavy Fermion materials. The corresponding lattice model is called the Kondo lattice model, with the Hamiltonian defined in one dimension as

$$\mathcal{H} = -t \sum_{i=1, \sigma}^{L-1} c_{i, \sigma}^\dagger c_{i+1, \sigma} + H.c. + J \sum_{i=1, \sigma}^L \vec{S}_i \cdot \vec{s}_i \quad (1.8)$$

Here the localized spins are periodically distributed on the lattice site. In the strong coupling limit  $J \gg t$  at half filling, the ground state is the Kondo insulator. Because there is one electron per site, every electron will form a spin singlet state with the localized spin as illustrated in Figure 1.4.

The Kondo model or Kondo lattice model is also studied in the context of other phases like the superconductivity. Experimentally the heavy Fermion superconductor has been found for certain materials [42], and the Weyl-semimetal could also be driven by the correlations with the magnetic impurities, which is identified as a new quantum material called the Weyl-Kondo semimetal [43]. The topological Kondo insulator with nontrivial topology has also

been proposed theoretically in three dimensions [44], where the spin-orbit coupling plays an important role in stabilizing those topological states.

If we allow the hopping between the f electrons and the itinerant electrons, the corresponding model is called the Anderson impurity model or periodic Anderson model [45]. The model is used to study the magnetic moment induced by the impurities in a non-magnetic metal. The heavy Fermion property can also be obtained from the periodic Anderson model because the Kondo lattice model is derived from the periodic Anderson model in the weak coupling limit. However, in the periodic Anderson model there is fluctuation in the conduction electron density, but there is no such fluctuation in the Kondo model. Thus the two models should be treated as different models.

# Chapter 2

## Density Matrix Renormalization Group Method

### 2.1 Introduction

The density matrix renormalization group (DMRG) is a numerical method for calculating the ground state of the many-body Hamiltonian [8, 9]. The ground state is an eigenstate with the lowest eigenvalue of the Hamiltonian, thus we can truncate the basis of the Hamiltonian by getting rid of the high energy states. Originally this idea was implemented as the numerical renormalization group (NRG) [37], which directly truncates the basis based on the energy. The NRG method is successful in predicting the physical properties of many strongly interacting systems such as the unexpected rise of resistivity in low temperature due to the magnetic impurity, which is known as the Kondo problem [37]. The numerical result gives resistivity from zero to high temperature in consistence with the experimental result. However, for a periodic lattice especially in finite size, the NRG method becomes less accurate.

The algorithm of both DMRG and NRG shares the same logic. Here we first introduce

the basic algorithm of the NRG method. The calculation starts with a small size system, with the dimensions of the Hilbert space small enough for the computer to diagonalize. Take the two spins Heisenberg model as an example, the Hilbert space is

$$H_2 = \vec{S}_1 \cdot \vec{S}_2 = \begin{pmatrix} \frac{1}{4} & 0 & 0 & 0 \\ 0 & -\frac{1}{4} & \frac{1}{2} & 0 \\ 0 & \frac{1}{2} & -\frac{1}{4} & 0 \\ 0 & 0 & 0 & \frac{1}{4} \end{pmatrix} \quad (2.1)$$

The ground state is the singlet state with eigenvalue of  $-\frac{3}{4}$ . The Hilbert space could be truncated without losing the information of the ground state by applying a unitary matrix transformation.

$$U = \begin{pmatrix} 0 & 0 \\ \frac{1}{\sqrt{2}} & \frac{1}{\sqrt{2}} \\ \frac{1}{\sqrt{2}} & -\frac{1}{\sqrt{2}} \\ 0 & 0 \end{pmatrix} \quad \tilde{H}_2 = U^\dagger H_2 U = \begin{pmatrix} \frac{1}{4} & 0 \\ 0 & -\frac{3}{4} \end{pmatrix} \quad (2.2)$$

As shown in Equation 2.2, the unitary matrix is chosen by the eigenvectors associated with the smallest two eigenvalues, and the dimensions of the Hilbert space are reduced. Then we add another spin to the system by taking the tensor product of the two subspaces.

$$H_n = \tilde{H}_{n-1} \otimes I + \vec{S}_{n-1} \otimes \vec{S}_n \quad (2.3)$$

Any operator in the original subspace is truncated with the same unitary transformation like  $\vec{S}^z$ . In this way the overall dimensions of the Hilbert space are fixed at a certain number and we can repeat the process until the energy per site converges. The general process is as follows assuming there are  $D$  degrees of freedom per site.

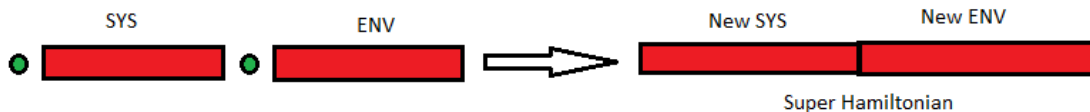


Figure 2.1: The whole system in DMRG is made of the system block and the environment block, and each time there is one site added to each block.

1. Build the Hamiltonian matrix for two sites, add one site to the system, and diagonalize the whole Hamiltonian.
2. Repeat until the dimension of the Hilbert space becomes larger than  $M$ .
3. Obtain the eigenvectors and the eigenvalues of the whole Hamiltonian and truncate it by the unitary transformation containing  $M$  lowest eigenvalues.
4. After the truncation, add one site to the block, and then dimension is just  $D \times M$  for each block.
5. Repeat the process of 3 and 4 until the energy per site converges.

Based on the NRG algorithm, the DMRG algorithm tries to include the environment and the coupling between the environment and the system. As a result, the Hamiltonian for the DMRG algorithm contains two blocks, the system block and the environment block. As shown in Figure 2.1, the tensor product of the two blocks is called the super Hamiltonian, and there is one site added to each block every time the system is enlarged.

The truncation of the super Hamiltonian is based on the reduced density matrix, which is defined as

$$\rho_s = Tr_e |\Phi\rangle \langle \Phi| \quad (2.4)$$

$$[\rho_s]_{i,i'} = \langle i | \rho_s | i' \rangle = \sum_j \langle ij | \Phi \rangle \langle \Phi | i'j \rangle \quad (2.5)$$

where  $|\Phi\rangle = \sum_{ij} \Phi_{ij} |i\rangle |j\rangle$  refers to the ground state of the super Hamiltonian,  $|i\rangle$  and  $|j\rangle$  refers to the indices of the system block and the environment block, respectively. In the Equation 2.4, the reduced density matrix of the system block is calculated by tracing over the environment block, and vice versa. After diagonalizing the reduced density matrix, the block is truncated using the largest  $M$  eigenvalues of the reduced density matrix.

The eigenvalues of the reduced density matrix have the properties given by Equation 2.6 because of the normalization of the ground state.

$$\sum_k \omega^k = 1, \omega^k > 0 \quad (2.6)$$

The  $\omega^k$  refers to the eigenvalue. In order to be able to continue the iteration the super Hamiltonian needs to be truncated. The truncation error is defined as

$$W = 1 - \sum_k^m \omega^k \quad (2.7)$$

Here we keep the largest  $M$  eigenvalues of the reduced density matrix. In general, the truncation error needs to be smaller than  $10^{-5}$  for the validity of the ground state properties, and  $10^{-7}$  for the correlation functions or the excitation properties.

Using the algorithm stated above, we could obtain the numerical results for infinite size system in one dimension, which is in the thermodynamic limit. For the finite size lattice, the site is not added to each block during the algorithm. As shown in Figure 2.2, after the desired lattice size is reached, we add one site to the environment block and remove one site from the system block at the same time. In this way, the total sites of the super Hamiltonian remain the same. When there is only one site in the system block, we start to add one site to the system block, and remove one site from the environment block. One circulation of this process is called a sweep.

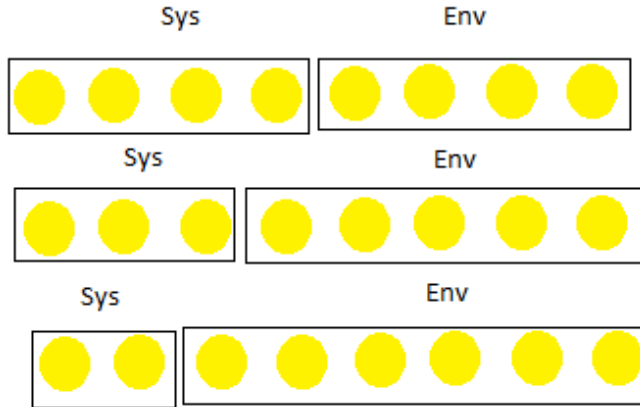


Figure 2.2: The schematic graph for the sweeping process in finite size DMRG algorithm, where 'Sys' refers to the system block and 'Env' refers to the environment block.

For finite size DMRG, we can calculate various physical properties such as the correlation function and the entanglement entropy besides the ground state energy during the sweep, and determine the convergence by these properties. This advantage does not occur in the infinite size DMRG algorithm because the lattice size always changes. As a result, the finite size DMRG is used more often in the numerical calculations because it is more accurate.

## 2.2 Finite temperature DMRG

The conventional DMRG method can only calculate the ground state which is at zero temperature, and very few low energy excited states. For thermodynamic properties such as the specific heat for finite temperature, we need to apply DMRG to the transfer matrix [46], which is related to the partition function.

$$Z = \text{Tr}(e^{-\beta H}) = \text{Tr}(T^N) = \sum_i \lambda_i^N \quad (2.8)$$

The transfer matrix  $T$  of the one dimensional lattice is given by Equation 2.8, assuming the periodic boundary condition.  $N$  refers to the number of sites, and  $\lambda_i$  refers to the eigenvalues of the transfer matrix. Because the  $N$  approaches infinity in the thermodynamic limit, the partition function only depends on the largest eigenvalue, thus we only need to calculate the largest eigenvalue in the algorithm.

The calculation of the transfer matrix is through the Suzuki-Trotter decomposition [47]. For nearest neighbor Hamiltonian we could separate the Hamiltonian into two terms, which are the Hamiltonian acting on the even sites and the odd sites. The interactions on the even sites commute with each other because the interactions are between nearest neighbor, but the interactions between the even sites and odd sites don't commute. The error introduced by separating the Hamiltonian could be controlled by the factor  $L$  as derived in below.

$$\begin{aligned}
Z_L &= \text{Tr}(e^{-\beta \frac{H_1}{L}} e^{-\beta \frac{H_2}{L}})^L \\
&= \text{Tr}(e^{-\beta \frac{H_1}{L}} e^{-\beta \frac{H_2}{L}} \dots e^{-\beta \frac{H_1}{L}} e^{-\beta \frac{H_2}{L}}) \\
&= \sum_{\alpha_1, \alpha_2 \dots \alpha_{2L}} \prod_{j=1}^L \langle \alpha_{2j-1} | e^{-\beta \frac{H_1}{L}} | \alpha_{2j} \rangle \langle \alpha_{2j} | e^{-\beta \frac{H_2}{L}} | \alpha_{2j+1} \rangle \\
&= \sum_{\{\alpha_1 \dots \alpha_{2L}\}} \prod_{i=1}^{\frac{N}{2}} \prod_{j=1}^L \langle s_{2i-1, 2j-1} s_{2i, 2j-1} | e^{-\beta \frac{h_{2i-1}}{L}} | s_{2i-1, 2j} s_{2i, 2j} \rangle \langle s_{2i, 2j} s_{2i+1, 2j} | e^{-\beta \frac{h_{2i}}{L}} | s_{2i, 2j+1} s_{2i+1, 2j+1} \rangle
\end{aligned} \tag{2.9}$$

The  $H_1$  and  $H_2$  in Equation 2.9 refers to the interaction terms on odd and even number of sites, respectively. The Trotter error is neglectable as long as  $L$  is much larger than  $\beta$ , and  $L$  is often regarded as the Trotter number to control the numerical error. The interaction after the Trotter decomposition can be viewed by the schematic graph in Figure 2.3. There

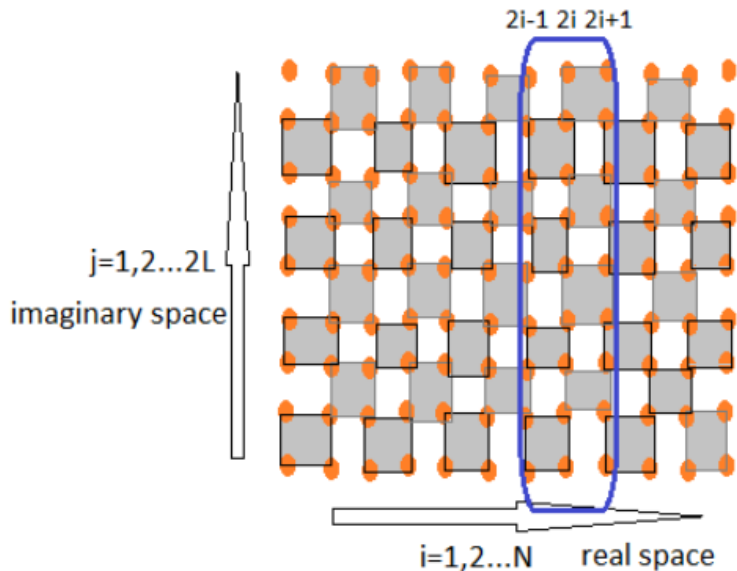


Figure 2.3: The schematic graph of the interactions in Trotter decomposition.

is an imaginary space with length of  $2L$  as well as the real space. Because the interactions are only among the four neighboring sites in the gray box, the decomposition is also called the checkerboard decomposition.

If we take the interactions within the blue circle as the transfer matrix, the partition function could be further reduced to Equation 2.10.

$$Z_L = \sum_{\{\alpha_1 \dots \alpha_{2L}\}} \prod_{i=1}^{\frac{N}{2}} T_1 T_2 = \text{Tr} (T_1 T_2)^{\frac{N}{2}} = \lambda_{\max}^{\frac{N}{2}} \quad (2.10)$$

After we calculate the largest eigenvalue of the transfer matrix, the physical properties such as the specific heat or the magnetic susceptibility per site can be obtained through the partition function.

## 2.3 DMRG in matrix product state

The accuracy of the DMRG method in calculating the ground state of the quantum systems depends on the quantum entanglement of the bipartite blocks, which is represented by the reduced density matrix. If we arrange the order of the eigenvalues of the reduced density matrix from large to small, the quantum systems with faster decaying eigenvalues will result in more accuracy in general as shown in Equation 2.7. This behavior in the eigenvalue spectrum of the reduced density matrix can be quantified by the entanglement entropy. The definition of the entanglement entropy is given as

$$S = - \sum_k \omega^k \ln \omega^k \quad (2.11)$$

In the numerical simulations, the entanglement entropy of the exact ground state can not be calculated because the exact ground state is unknown. However, the quantum entanglement is easier to control during the algorithm if we express the approximate ground state numerically using the matrix product state [48].

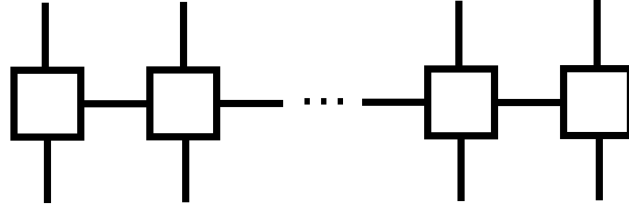
In general any quantum state could be expressed as the product of matrices with the help of single value decomposition (SVD). Assuming the open boundary condition of a finite size lattice, the state  $|\psi\rangle$  is derived in Equation 2.12.

$$|\psi\rangle = \sum_{\{\sigma_i\}} C_{\sigma_1, \dots, \sigma_L} |\sigma_1, \dots, \sigma_L\rangle = \sum_{\{\sigma_i\}} \sum_{\{a_i\}} A_{a_1}^{\sigma_1} A_{a_1, a_2}^{\sigma_2} \cdots A_{a_{L-2}, a_{L-1}}^{\sigma_{L-1}} A_{a_{L-1}}^{\sigma_L} |\sigma_1, \dots, \sigma_L\rangle \quad (2.12)$$

The index  $\sigma_i$  refers to the physical index that is determined by the local degrees of the freedom given by the Hamiltonian, while the index  $a_i$  refers to the bond whose dimensions could be controlled during the DMRG algorithm. The quantum entanglement of the state is proportional to the largest bond dimensions of  $a_i$ . Similarly any operator could be expressed



Matrix product state (MPS)



Matrix product operator (MPO)

Figure 2.4: The schematic representation of the matrix product state and matrix product operator.

in the same way.

$$\hat{O} = \sum_{\{\sigma_i\}, \{\sigma'_i\}} \sum_{\{a_i\}} A_{a_1}^{\sigma_1, \sigma'_1} A_{a_1, a_2}^{\sigma_2, \sigma'_2} \cdots A_{a_{L-2}, a_{L-1}}^{\sigma_{L-1}, \sigma'_{L-1}} A_{a_{L-1}}^{\sigma_L, \sigma'_L} |\sigma_1, \dots, \sigma_L\rangle \langle \sigma'_1, \dots, \sigma'_L| \quad (2.13)$$

The matrix elements of the matrix product operator are still operators, but those operators only act on the local sites. Thus the indices of every matrix is only summed by the nearby matrix, and we can represent this matrix product state in Figure 2.4 similar to the tensor network.

The algorithm is slightly different than the conventional DMRG. The initial state is guessed with fixed lattice sites instead of growing iteratively. Usually the initial guess is a Neel state or a randomized state. After that the sweeps from left to right and then right to left are taken the same way as the conventional DMRG. Every time all but one matrix are fixed, and we try to minimize the energy of the current state with the Lagrangian Multiplier.

This step is a generalized eigenvalue problem, which is equivalent to the conventional DMRG that adds one site to the block and remove one site from the other block.

During the sweeps the bond dimensions of the matrix product state are increased and eventually fixed until the ground state converges. The advantage of the matrix product state is that it automatically allows the long-ranged interacting terms in the Hamiltonian, which is essential for calculations in two dimensional systems. The two dimensional lattice is always treated as the one dimensional zigzag chain, where the nearest neighbor interactions in two dimension becomes long-ranged in the chain. Because the long-ranged interactions will lead to large quantum entanglement, usually the DMRG method is performed in the cylindrical geometry, with the circumference much smaller than the height. In addition, the ansatz is the same throughout the sweeps. The matrix product operator does not change because the dimension of the physical bond is only determined by the local degrees of freedom.

In general, the matrix product operator representation of the operator is not unique. The long-ranged interactions will lead to large dimensions of the matrix product operator, and the calculation becomes more difficult. However, for certain types of long-ranged interactions such as the exponentially decaying interactions, the corresponding matrix product operator is rather small. These types of Hamiltonian are specifically suitable for the DMRG method in matrix product state.

## 2.4 Other methods based on DMRG

The DMRG method based on the matrix product state is a variational method that is stable and suitable for different types of systems. Nowadays it has become one of the standard numerical method in computational physics. Based on DMRG, people have developed other algorithms that could deal with more complicated problems. The time evolving block decimation (TEBD) algorithm [49] implements the time evolution operator acting on the

matrix product state. It can be used in the non-equilibrium system or the quantum quenching. The minimally entangled typical thermal states (METTS) [50, 51] and the purification method [52, 49, 53] based on matrix product state can calculate two dimensional systems at both low and high temperatures. Although the sampling process in METTS is usually time-consuming and the purification method often requires larger computer memory, the simulations on simple models such as the Heisenberg model are still reliable. The infinite projected entangled pair state (iPEPS) [54] can be used for real two dimensional lattices with infinite length in both directions, but the convergence of the iPEPS is sometimes hard to control because there is no orthogonal center due to the tensor geometry.

The numerical accuracy of the algorithms based on matrix product state mainly depends on the number of states kept during the single value decomposition (SVD) process. As a result, different algorithms on the finite size lattice often have approximately the same accuracy with the same computer resources. However, as the theoretical understanding of the DMRG algorithm develops, the DMRG will play an important role in numerical simulations of different fields in the future. For example, the topological properties such as the edge state spectrum and topological quantum dimensions [55] could be obtained directly from the DMRG, making it popular in the study of interacting topological systems.

# Chapter 3

## The Kondo lattice model

### 3.1 Introduction

As a fundamental model for strongly correlated system describing heavy Fermion materials [56, 57, 58] and quantum magnetism [59], the Kondo lattice (KL) model [60, 61, 62] has been intensively studied over the last decades, especially in one dimension [63, 64].

The strong correlations in the weak coupling between electrons and localized spins makes it notoriously difficult for exact solutions. Thus numerical method becomes important in order to determine the phase diagram.

The Hamiltonian of the Kondo lattice model in one dimension is given as

$$\mathcal{H} = -t \sum_{i,\sigma} c_{i,\sigma}^\dagger c_{i+1,\sigma} + H.c. + J \sum_i \vec{S}_i \cdot \vec{s}_i \quad (3.1)$$

The first term in the Hamiltonian is the hopping term where  $c_{i,\sigma}^\dagger$  refers to the creation operator of an electron on site  $i$  with spin index  $\sigma$ , the second term describes the spin-spin interaction where  $\vec{S}_i$  denotes the localized spin- $\frac{1}{2}$  and  $\vec{s}_i = \frac{1}{2} \sum_{\alpha,\beta} c_{i,\alpha}^\dagger \vec{\sigma}_{\alpha,\beta} c_{i,\beta}$  (with Pauli matrices  $\vec{\sigma}$ ) the conduction electron spin.

To calculate the ground state we use the U(1) DMRG method with open boundary condition for lattice size up to  $L = 208$ . Calculations are performed using the ITensor library [65]. Smaller sizes are also used for finite size extrapolation. The largest bond dimension is 7,000 during the sweeps. 140 sweeps with increasing bond dimension were used in order to reach stable and convergent ground state. The cutoff error during the last few sweeps is  $10^{-7}$ . The hopping parameter  $t$  and the lattice spacing is set to unity to fix the energy scale.

## 3.2 One dimensional phase diagram

At half filling, the insulating phase is caused by the formation of the Kondo singlet. In the strong coupling limit, every electron forms a spin singlet state with the localized spin, and the charge gap is determined by the energy needed to break the singlet state. Numerical studies have shown that the finite charge gap exists for any finite  $J$  at half filling [66]. Similarly, in the strong coupling limit, the spin gap is the energy difference between the singlet state and the triplet state, which is  $J$ . As  $J$  decreases, the spin gap also decreases but it does not vanish for any finite  $J$ .

The finite spin gap will result in the zero magnetic susceptibility at the zero temperature, but when the temperature becomes comparable to the spin gap, the magnetic susceptibility becomes finite due to the thermal fluctuations. Using the finite temperature DMRG method we can study the temperature dependence of the uniform spin susceptibility.

The spin susceptibility is obtained by the change of the magnetization caused by a small magnetic field. During the calculations 25 states are kept to reach the truncation error of  $5 \times 10^{-4}$ , and the minimum temperature is 0.01 with the Trotter number = 2000. As shown in Figure 3.1(a), the spin susceptibility follows the Curie law at high temperature, and starts to deviate as the temperature decreases. At  $T < 0.02$  the spin susceptibility drops to nearly

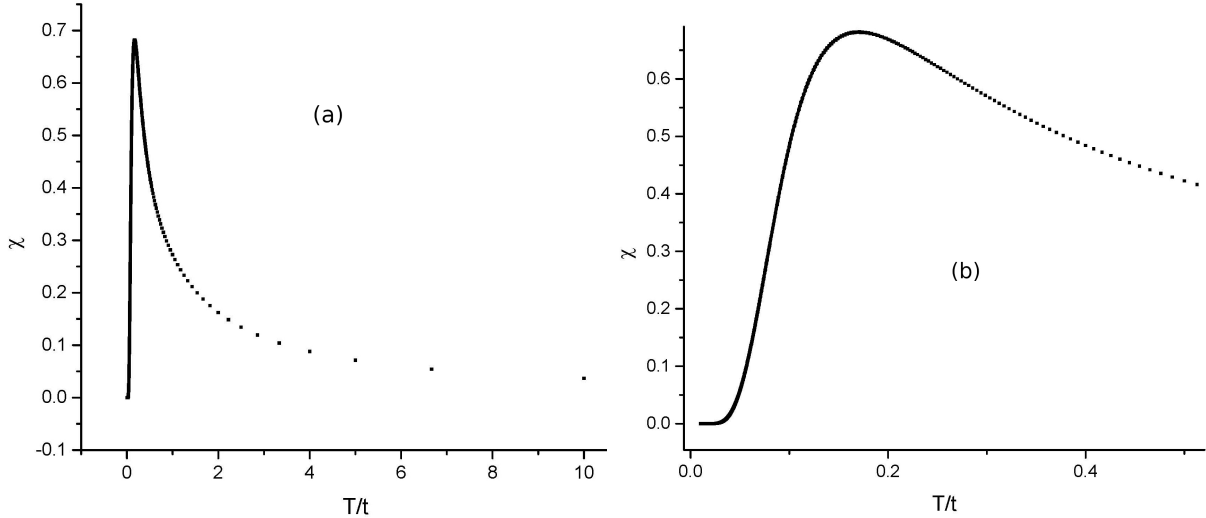


Figure 3.1: The uniform spin susceptibility of the one dimensional Kondo lattice model at half filling for various temperatures in Figure 3.1(a). Figure 3.1(b) shows the same susceptibility for the temperatures close to zero. The results are obtained at  $J = 1$ .

zero, which agrees with the finite spin gap in the ground state. The same susceptibility for temperature close to zero is plotted in Figure 3.1(b). The spin gap of the ground state is  $0.08t$ , which is generally consistent with the corresponding temperature where the spin susceptibility becomes finite.

Away from the half filling the ground state is metallic and the numerical simulations become harder because of the gapless excitations. Here we have only calculated the ground state properties in the doped regime.

In the extremely doped case where there is only one electron in the system, the localized spins tend to be anti-parallel to the electron spins. Because the same spin hopping of the electrons is energetically favorable, the localized spins align in one direction for the ground state. This ferromagnetic state is named Nagoaka state [67] with any finite Kondo coupling  $J$ . Additionally, in the atomic limit of the doped regime all electrons will form the Kondo singlet with the localized spins. However, there are more localized spins than electrons. The finite hopping term of the electrons results in an indirect ferromagnetic exchanges between

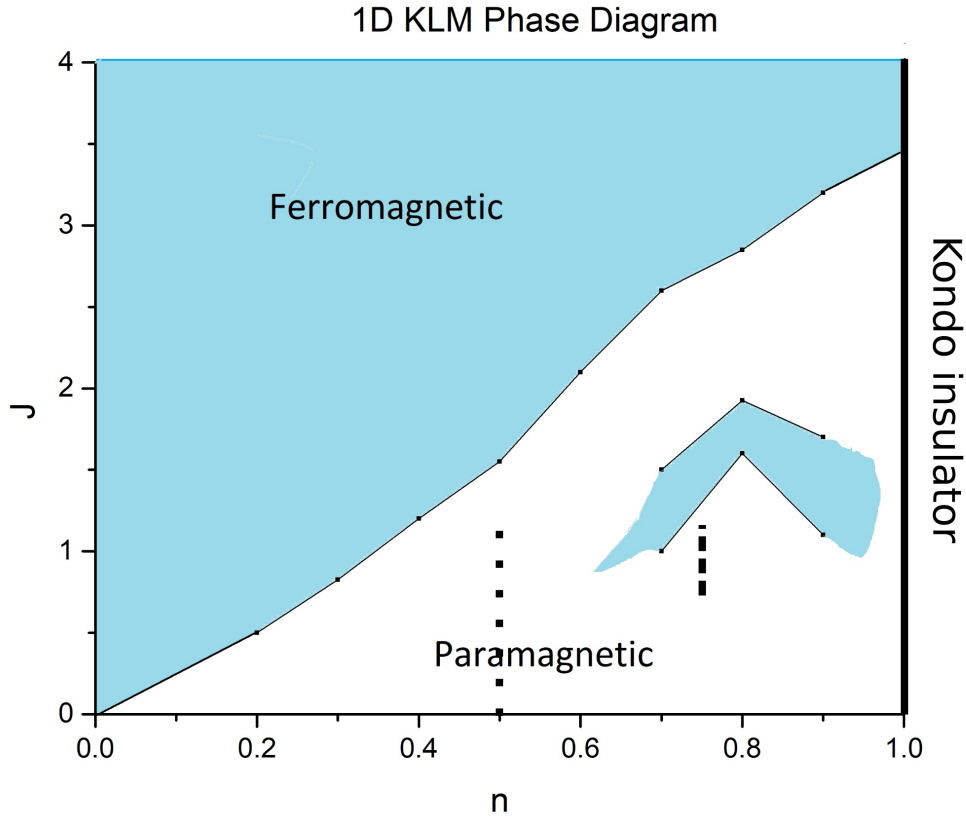


Figure 3.2: The ground state phase diagram of the one dimensional Kondo lattice model. The ferromagnetic (paramagnetic) state is represented by the blue (white) regime, and the solid line at  $n = 1$  is the Kondo insulator. The two dashed lines at  $n = 0.5$  and  $n = 0.75$  indicate the commensurate dimer phase and charge density wave phase, respectively.

the rest of the localized spins, and the ground state is also ferromagnetic.

The theoretical analysis is helpful to determine the ground state phase diagram. We can determine the phase boundary of the ferromagnetic state by calculating the ground state energy of different spin sectors because the total electron number and the total spin in the z-direction are conserved quantum number. In the ferromagnetic state the ground state energy is the same for different spin sectors, but for the paramagnetic state the ground state energy in the  $S_z^{tot} = 0$  sector has the lowest energy. Although in DMRG simulations the ground state in larger spin sectors generally has less entanglement that will result in a

quicker convergence and even lower ground state energy than the  $S_z^{tot} = 0$  sector, we can determine the phase boundary between the ferromagnetic state and the paramagnetic state in an unbiased way.

As shown in Figure 3.2, the ferromagnetic state dominates the strong coupling and doped regime. In the atomic limit where all electrons have formed spin singlet state with the localized spins, the average magnetization is determined by Equation 3.2 where  $n$  is the electron density. We found that this is true for the whole ferromagnetic regime.

$$\langle M \rangle = \frac{1}{2}(1 - n) \quad (3.2)$$

There is a phase transition into the paramagnetic regime as  $J$  decreases, where the Kondo singlet breaks down and the spins become strongly correlated because of the Ruderman-Kittel-Kasuya-Yosida (RKKY) [39, 40, 41] interaction. The paramagnetic phase could be described by the Tomonaga-Luttinger liquid (TLL) which is a universal class for interacting Fermions in one dimension. All the correlation functions could be determined by the Luttinger parameter. In the DMRG calculations, the open boundary of a finite size lattice could induce Friedel oscillations [68], and the Luttinger parameter is numerically calculated by fitting this charge oscillations. Other properties of the TLL could also be obtained numerically such as the spin charge separation. We have found that the period of the electron spin oscillations is always twice as the period of the charge oscillations.

Besides the ferromagnetic state in the strong coupling regime, there is a second ferromagnetic regime in the intermediate coupling. The average magnetization of this ferromagnetic state can still be determined by Equation 3.2, and the phase is also metallic. Although the ground states of this two ferromagnetic regime show similar properties, in the intermediate ferromagnetic regime a finite charge gap above the Fermi level is found for the electrons with opposite spin value to the magnetization of the system [69]. This suggests that the

mechanism driving the ferromagnetism for the two regimes might be different.

In the paramagnetic regime two insulating states are identified at the commensurate electron density of  $n = \frac{1}{2}$  and  $n = \frac{3}{4}$  in the weak coupling, which is discussed in the next two sections (the results at  $n = \frac{3}{4}$  have been published [70]).

### 3.3 Charge density wave

Previous studies have mainly focused on the competition between the Kondo effect and the RKKY interaction, while the effective Coulomb repulsion induced by the localized spins was neglected. In the 1D bosonization theory, if the interaction is strong enough, the system undergoes a phase transition from the TLL to an insulating phase. The TLL phase with a large Fermi surface has been found in the weak coupling [68, 71, 72] of 1D KL model at less than half filling. From DMRG studies, we find that the effective Coulomb repulsion is strong enough to induce the charge ordered insulating phase at commensurate fillings.

In the KL model the charge order has been investigated in higher dimensions. Using the dynamical mean field theory (DMFT) method and variational Monte Carlo method, a charge density wave (CDW) in the weak coupling has been found in both two dimensions [73, 74, 75] and infinite dimensions [76] at quarter fillings. The intriguing question remains whether the charge order exists in one dimension, as the DMFT method generally gets less accurate in low dimensions, especially in one dimension. Additionally, the charge order in higher dimensions is stabilized by the Kondo singlet formation, which is different from the 1D case.

The origin of the effective repulsive interaction in a KL model is proposed by a strong-coupling perturbation expansions [77]. However, for 1D the strong coupling region is dominated by the Kondo effect which results in ferromagnetism [78, 69] at less than half filling, as illustrated by Figure 3.2. And the CDW is identified at the commensurate filling of  $n = \frac{3}{4}$  in the weak coupling regime.

The electron density in the CDW phase shows modulation in real space under the open boundary condition as a result of spontaneous symmetry breaking. While the Mermin-Wagner theorem [79] forbids any spontaneous breaking of continuous symmetry in 1D, CDW only breaks the lattice translational symmetry which is discrete. In Figure 3.3(a) we show  $\langle N_i \rangle$  at  $J = 0.9, L = 160$ . There are strong oscillations around the average electron density with the amplitude  $\approx 0.03$ . The oscillation decays very slowly away from the boundary and remains finite in the middle of the chain. This allows us to define the order parameter as  $A = \lim_{L \rightarrow \infty} A(L/2)$  the amplitude of electron density oscillation in the middle.

The finite size extrapolation is needed to determine the order parameter in the large system limit. The extrapolated order parameter is plotted against  $J$  in Figure 3.3(c). When  $J$  is close to the critical point slightly above 1.0, the order parameter quickly rises from 0, and then decreases slowly to 0 as  $J$  decreases. Figure 3.3(d) shows the finite size extrapolation of the order parameter for various coupling. Inside the parameter range from  $J = 0.7$  to 1.0  $A(L/2)$  has a weak dependence of  $L$ , and remains a finite value as  $L$  goes to infinity.

The Fourier transform of the electron density in Figure 3.3(a) is plotted in Figure 3.3(b). We have used the smoothed Fourier transform in order to minimize the effect caused by the open boundary. The details of the window function that we use are discussed in Refs. [80, 81]. Here the CDW phase is dominant by a single peak at  $k = \frac{\pi}{2}$ , which corresponds to the oscillation period of 4 lattice spacing. There may be a superposition of other oscillation frequency such as  $k = \frac{\pi}{4}$ , but they all vanish in the thermodynamic limit as illustrated later. The inset of Figure 3.3(b) shows the intensity of the dominant peak divided by the lattice size. The intensity has a almost linear dependence of  $L$  and remains finite after the extrapolation.

The structure factor  $N(k)$  of the charge ordered phase always scales as the order parameter multiplied by the lattice length. In the infinite chain limit, The order parameter defined

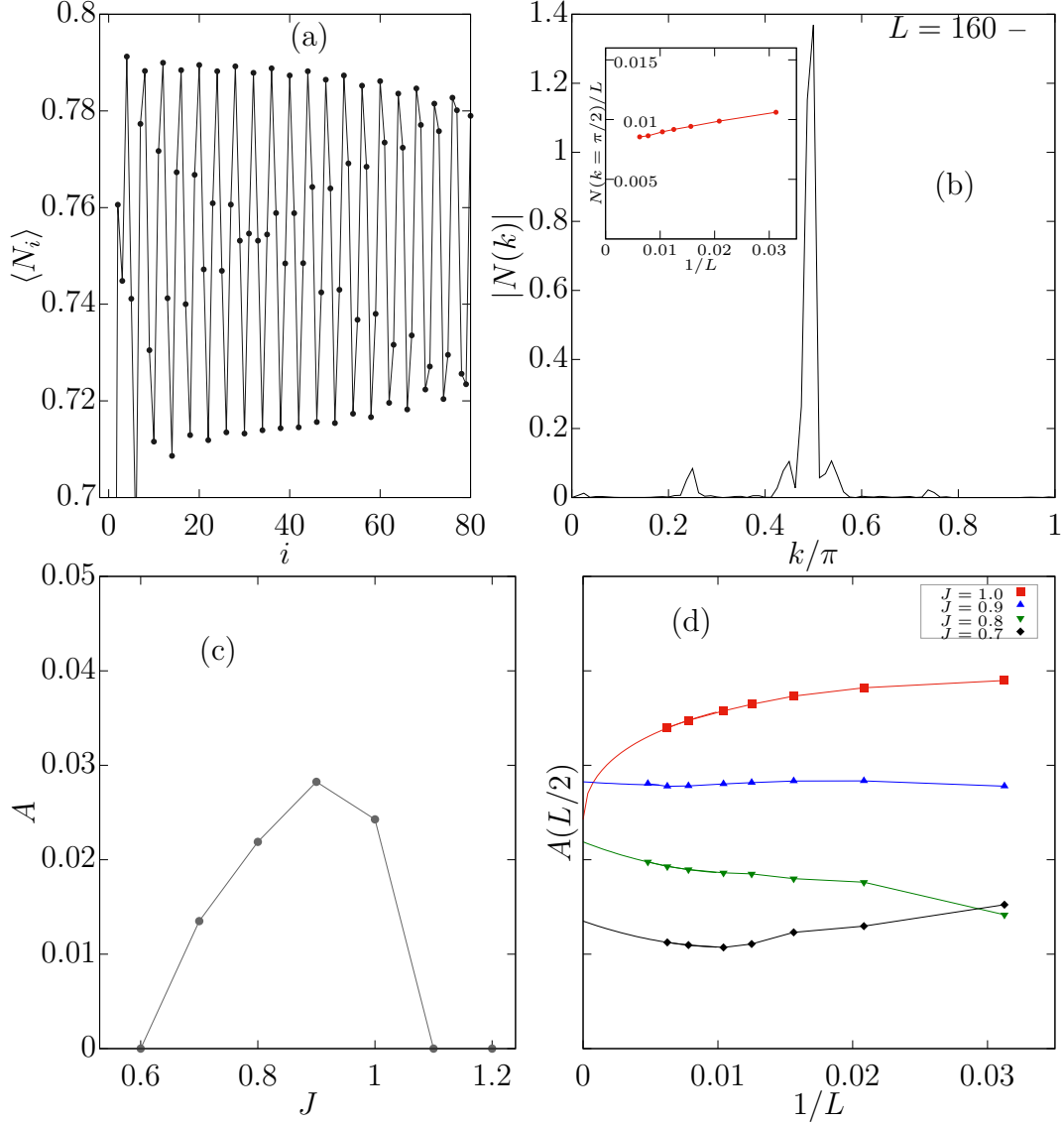


Figure 3.3: (a) is the electron density at  $J = 0.9, L = 160, n = \frac{3}{4}$ . Only half of the lattice is shown. (b) is Fourier transform of the density oscillation in (a). The dominant peak shows up at  $k = \frac{\pi}{2}$ . The inset of (b) shows the intensity of the  $k = \frac{\pi}{2}$  peak divided by the length. (c) is the  $J$  dependence of the oscillation amplitude in the middle after finite size extrapolation. The extrapolation in (d) is conducted in this way. If the fitting agrees well with the power decay of the Friedel oscillation in TLL then the order parameter is considered zero when  $L \rightarrow \infty$ , otherwise we use a least-square fit to the second order of polynomials in  $1/L$ . For  $J$  close to the transition we find it better to fit to  $1/\sqrt{L}$  as the similar scaling in TLL.

by the structure factor is essentially equivalent to the definition of the oscillation amplitude in the middle of the chain. As shown in Figure 3.3(d) and the inset of Figure 3.3(b), the order parameters both remain finite in the CDW phase.

The Luttinger parameter  $k_L$  in the TLL of the 1D KL model shows a monotonic decrease as  $J$  decreases at the fixed electron density [71, 72], indicating a strong repulsive interaction between electrons in the weak coupling region. This could explain the formation of a CDW under strong repulsion. However, in the limit of  $J \rightarrow 0$ , the system goes back to free 1D electrons with  $k_L = 1$ . Thus it is natural to see a critical point where the effective repulsive interaction isn't strong enough to stabilize CDW, and the system goes back to TLL. In the bosonization picture, the Umklapp type scattering term, which carries a fast oscillation phase factor, only appears in the low energy effective Hamiltonian at special fillings [82].

$$\Psi_{R,\uparrow}^\dagger \Psi_{R,\downarrow}^\dagger \Psi_{L,\uparrow} \Psi_{L,\downarrow} \propto e^{-i4K_F x} e^{i2\sqrt{2}\phi_\rho(x)} \quad (3.3)$$

If  $4K_F = 2\pi$ , corresponding to  $n = 1$ , the fast oscillation term becomes constant in Equation 3.3 and enters in the low energy effective Hamiltonian. If  $k_L < 1$  then this term is relevant in the renormalization procedure, and opens a gap in the charge sector. Higher order terms of Umklapp scattering could also occur at other commensurate fillings. In our case of  $n = \frac{3}{4}$ , the fourth power term of the Umklapp scattering can occur in the extremely small value of  $k_L < \frac{1}{16}$ . In fact, as we vary  $J$  at  $n = \frac{3}{4}$ ,  $k_L \rightarrow \frac{1}{16}$  when the system is close to the phase transition.

In order to determine the Luttinger parameter in the TLL phase, we compare the Friedel oscillation [68] amplitude at the center for different lattice sizes. The methods that we used to determine the Luttinger parameter are adopted from Ref. [81]. As shown in Figure 3.4(a), we fit the log-log plot of the oscillation amplitude and find that for  $J = 1.1$  the Luttinger parameter is 0.067, which is very close to the critical value of  $\frac{1}{16}$ . This agrees with the

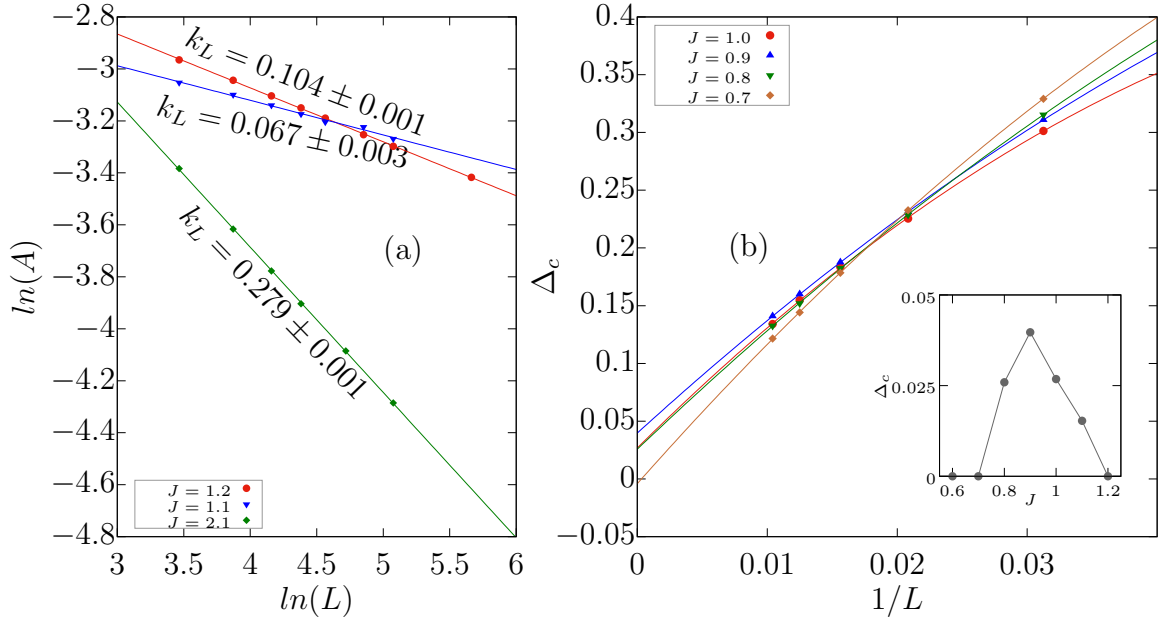


Figure 3.4: (a) is the log-log plot of the Friedel oscillation amplitude in the middle of various lengths. The Luttinger parameter  $k_L$  is determined by the  $\text{slope} = -2k_L$ . The error of  $k_L$  is given by the standard deviation of the least square fit. The Luttinger parameter decreases as we lower  $J$  into the weak coupling region, which agrees with previous studies. For  $J = 1$  it cannot be linearly fit, indicating the onset of CDW. (b) is the finite size extrapolation of the charge gap at  $n = \frac{3}{4}$ . Four examples of  $J$  are given for the least-square fit. The inset of (b) shows the extrapolated charge gap for various  $J$ .

assumption that the CDW is driven by the strong effective Coulomb repulsion. Near the critical  $J$ , the oscillation decay rate is so slow that we cannot be sure whether or not the oscillation will vanish in the limit of infinite long chain [81]. Although it is hard to determine the exact critical value of  $J$ , the Luttinger parameter close to the transition point provides another evidence of the emergence of the CDW.

Then we investigate the charge gap in the CDW. Figure 3.4(b) shows the  $J$  dependence of the Charge gap at  $n = \frac{3}{4}$ , which is defined as

$$\Delta_c = \lim_{L \rightarrow \infty} [E_0(N_e = N + 2) + E_0(N_e = N - 2) - 2E_0(N_e = N)] \quad (3.4)$$

where the  $E_0(N_e)$  refers to the ground state energy of a given electron number. Here we set  $N = \frac{3}{4}L$  to fix the electron density. We choose  $J$  carefully to avoid the ferromagnetic region so that the ground state is always in the  $S_z^{total} = 0$  subspace. The charge gaps here only depend on the ground state energy calculated by the DMRG method, thus are very reliable. In Figure 3.4(b), the charge gap is extrapolated by a least-square fit to the second order of polynomials in  $1/L$ . A non-zero value of the gap can be distinguished in the thermodynamic limit. The inset of Figure 3.4(b) shows the extrapolated result of the charge gap at different values of  $J$ . The gap reaches a maximum value at around  $J = 0.9$ , and has a monotonic decreasing to 0 apart from the peak. Generally in a gapped phase the correlation function either has an exponential decay or decays to a constant at large separations. The electron density oscillation agrees with the latter case here. The emergence of a non-zero charge gap is consistent with the CDW, and together with the CDW order parameter, we can establish the TLL-CDW phase boundary at  $J \approx 1.1$  and  $0.7$ .

The measurement of the Zeeman field needed to close the charge gap could be used as a scale of finite transition temperature  $T_c \sim \frac{\mu_B h_c}{k}$ . We found  $h_c = 0.03$  at  $J = 0.9$ , where the CDW is also destroyed.

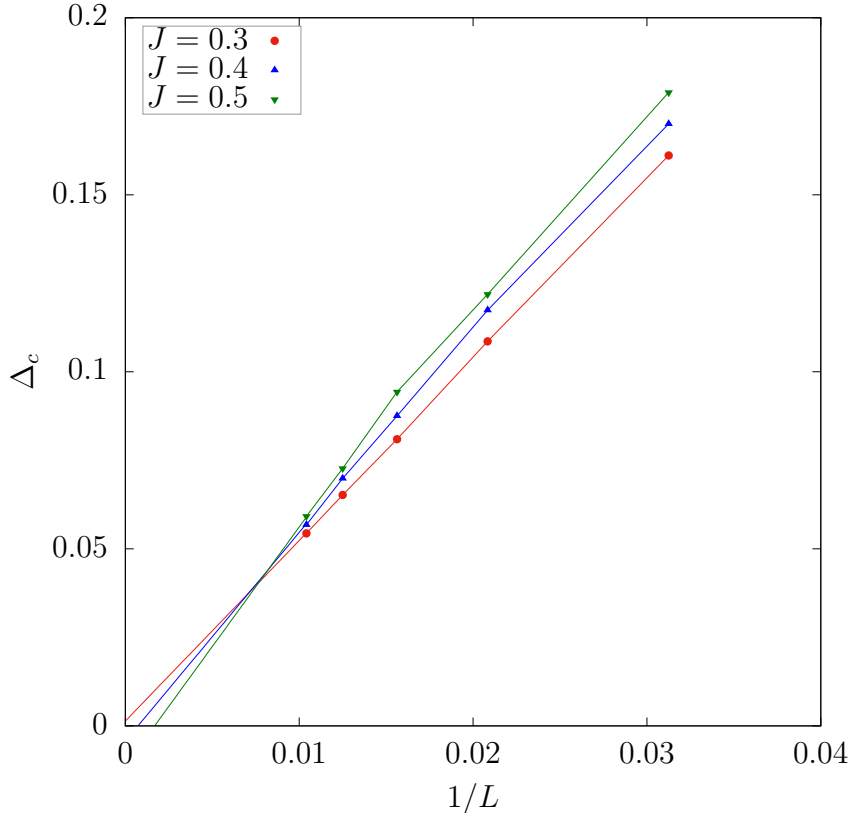


Figure 3.5: The finite size extrapolation of the charge gap at  $n = \frac{1}{4}$ .

The spin gap is defined in a similar way  $\Delta_s = E_0(S_z^{tot} = 1) - E_0(S_z^{tot} = 0)$  except that  $E_0(S_z^{tot} = -1)$  is not needed due to the spin symmetry. We have calculated the spin gaps for several  $J$  with different lattice sizes and the gap is always zero with an error bar in the order of the truncation error. Although numerically we can never rule out a very tiny spin gap in larger sizes, additional evidence to support the vanishing spin gap is found considering the density oscillation period. The effective spin in one unit cell remains a half-integer number, which resembles the spin-half Heisenberg model with gapless spin excitation.

The possible CDW phase at the commensurate filling of  $n = \frac{1}{4}$  is also investigated using DMRG. Figure 3.5 shows the finite size extrapolation of the charge gap in the paramagnetic region at  $n = \frac{1}{4}$ . The charge gap is defined the same as the one in the main text. We have found no evidence of a charge gap for  $0.5 > J > 0.3$ . We haven't calculated the charge gap

for  $J > 0.6$  because the region is dominant by the ferromagnetic phase, while at  $n = \frac{3}{4}$  there is no ferromagnetic phase for  $J < 1.2$ . In addition, we have fit the electron density oscillation similar to the main text and found  $k_L = 0.23$  for  $J = 0.3$ . The Luttinger parameter is still way above the critical value of  $\frac{1}{16}$ . We have found no charge order at  $n = \frac{1}{4}$  based on our numerical results. For very small  $J < 0.2$  it is hard for the algorithm to reach convergence, and we do not rule out the possibility of different phase there.

We then turn to the correlation of the localized spins in the CDW. Unlike the charge part, the total spin of the ground state preserves the  $SU(2)$  symmetry. The RKKY interaction between the localized spins could lead to possible valence bond solid as it has been reported in the 1D KL at quarter filling [83].

We first study the nearest neighbor correlation of the localized spins, i.e.  $\langle S_i \cdot S_{i+1} \rangle$ . Figure 3.6(a) shows that the correlation has  $k = \frac{\pi}{2}$  oscillations with a superposition of incommensurate oscillations with  $k = \frac{\pi}{L}$  which is size dependent. Generally in a valence bond solid, the dimer order described by the short-ranged spin correlation should be  $L$  independent away from the boundary, as the example of the KL on the zigzag ladder at half filling [84]. Quantum fluctuations will destroy any incommensurate order in 1D, so the leading order at the weak coupling of  $n = \frac{3}{4}$  is just the charge order. The average correlation of the nearest neighbor spins is antiferromagnetic, which is consistent with the RKKY interaction close to half filling. Here the correlation of the localized spins cannot be explained by the low energy effective Heisenberg model with RKKY couplings because of the existence of charge fluctuations. We believe the  $k = \frac{\pi}{2}$  oscillation of the localized spin correlation is mainly induced by the  $k = \frac{\pi}{2}$  CDW because of the antiferromagnetic coupling between the electron spins and the localized spins.

For further illustration we study the dimer-dimer correlations which is defined as the two point correlation functions of the localized spins  $\langle O_x \cdot O_{x+i} \rangle$ , where  $O_x = S_x \cdot S_{x+1}$  refers to

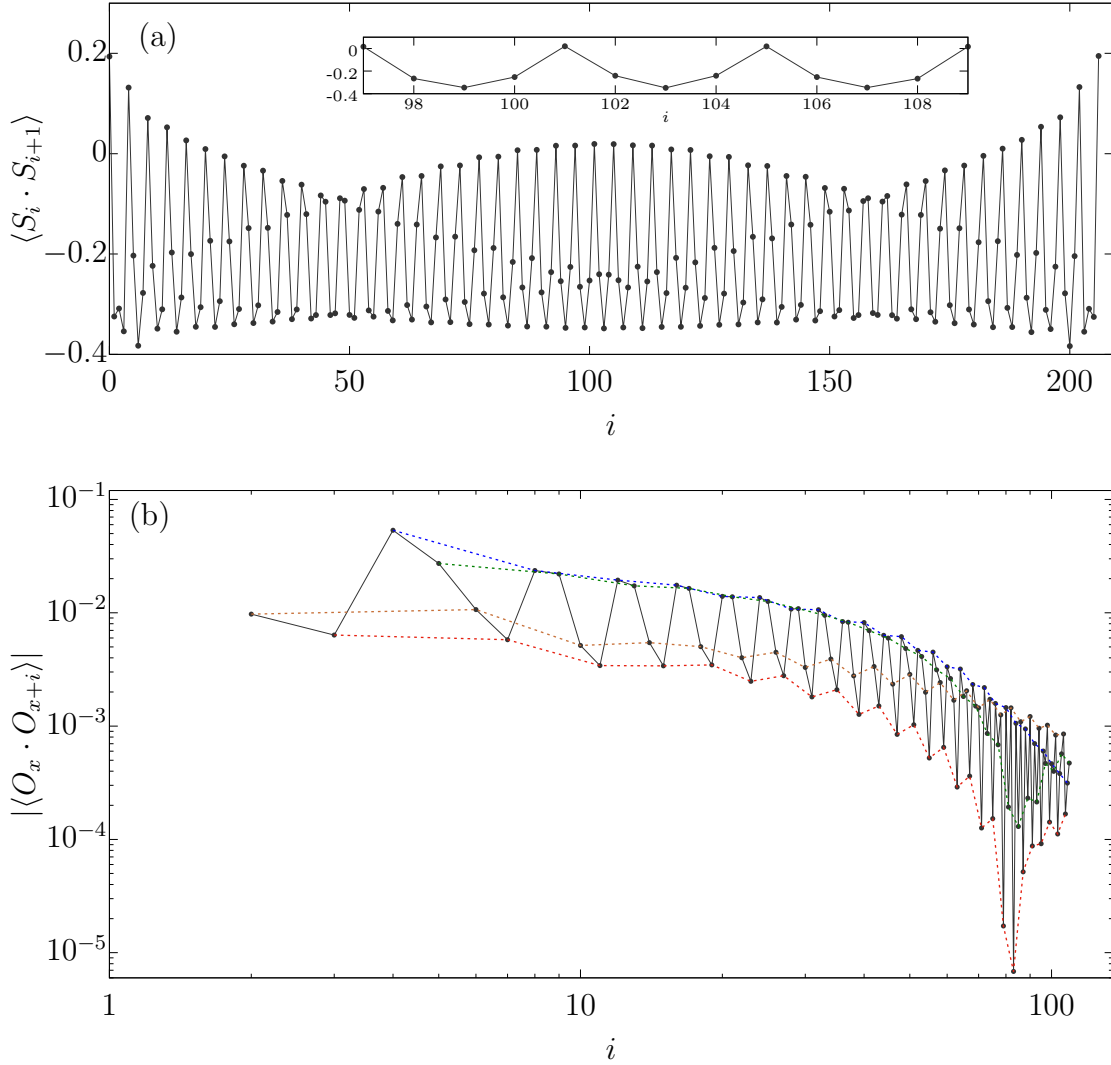


Figure 3.6: The nearest-neighbor (Figure 3.6(a)) and long range dimer-dimer (Figure 3.6(b)) correlation of the localized spins at  $J = 0.9, L = 208, n = \frac{3}{4}$ . In (a) the average correlation is around -2.0, which is  $L$  independent. The incommensurate oscillation refers to the upper bound in the middle with  $k = \frac{\pi}{L}$ . The amplitude of the incommensurate oscillations has almost no dependence of the lattice length. The inset of (a) shows the dominant oscillation of the correlation with a period of 4, which is the same period as the CDW. In (b) we calculate the correlation at  $x = 29$  to minimize the boundary effect. The plot uses logarithmic scale on both axis in order to identify the decay mode. The dimer-dimer correlation also has an oscillation period of 4. The 4 color dashed lines are nothing but the correlation of every four points connected, because they each has a different pattern. The correlation functions of the TLL are not shown here as they have monotonic power law decays which agrees with the bosonization theory.

the nearest neighbor spin correlation. The  $\langle O_x \cdot O_{x+i} \rangle$  plotted in Figure 3.6(b) shows a decay over distance, although in an oscillation fashion. The correlation is dominant by the blue line, indicating a slow exponential decay. This is different from the TLL where correlation functions generally has power law decays. It seems that the correlation saturates toward a finite value for the green and red line at around  $i = 80$ , but after analyzing the dimer-dimer correlation at different points, we find that it always 'saturates' near the middle of the lattice. The similar 'saturation' is also found in the TLL phase at  $J = 2.1, n = \frac{3}{4}$ . We argue that this is just an artificial effect due to finite size of system, as the correlation will have a monotonic decay in the limit of an infinite chain. This is consistent with our conclusion that the phase at  $n = \frac{3}{4}$  for weak  $J$  is dominant by the charge order.

To summarize this section, we have used the DMRG method to provide compelling evidence for CDW at  $n = \frac{3}{4}$ , similar CDW is not found at the other commensurate filling of  $n = \frac{1}{4}$ . The numerical results is consistent with the bosonization prediction near the phase transition, suggesting that the CDW is driven by the effective Coulomb repulsion, which is qualitatively different from the CDW in higher dimensions [73, 76], and at extremely small  $J$  in 1D predicted recently [85]. We also find that CDW is insulating, while the phase at incommensurate filling or generally in TLL is metallic. Under the existence of CDW, the localized spin has formed a similar oscillation pattern, while preserving the total spin SU(2) symmetry. Other magnetic orders like the antiferromagnetic order has not been found in the CDW phase. Our results provide a simple mechanism of the charge order in 1D organic compounds. The emergence of the CDW may have implications for the novel phase diagram of the KL model in higher dimensions.

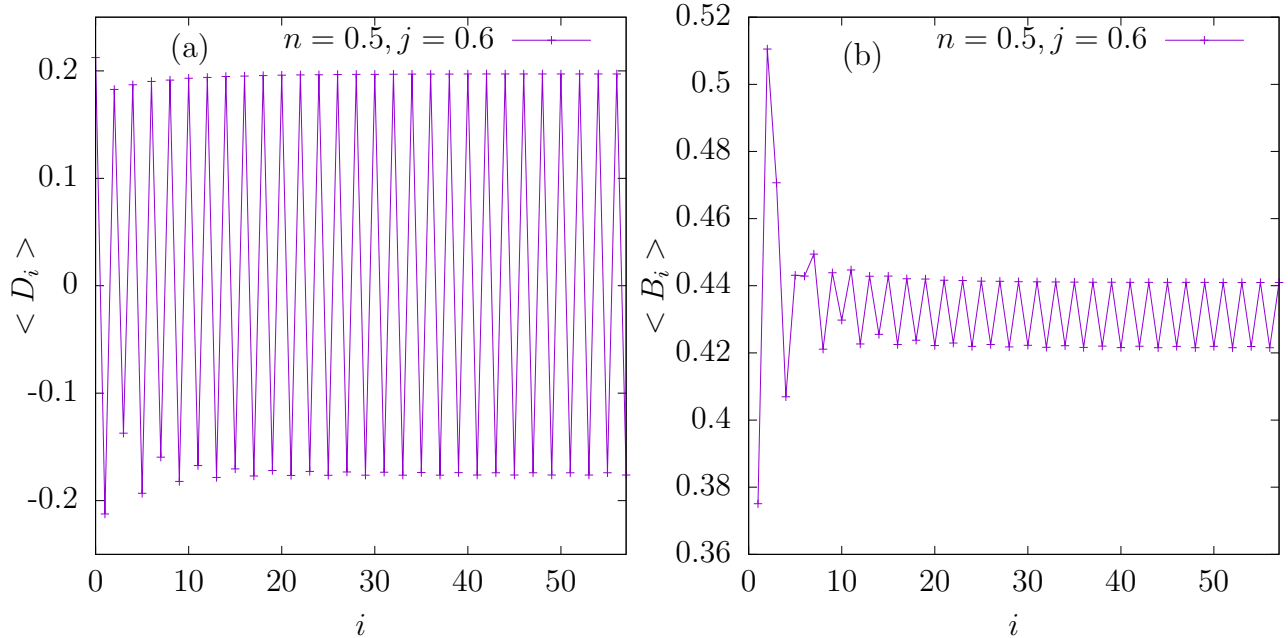


Figure 3.7: The dimer order (a) and bond order wave (b) at  $n = 0.5, J = 0.6$  obtained by the finite size lattice of  $L = 112$ . Only half of the lattice is shown.

### 3.4 Dimer order and bond order wave

The 1D KL model at quarter filling ( $n = \frac{1}{2}$ ) has been investigated [83, 86] to realize a dimerization of the localized spins induced by RKKY interaction, although there are some controversy about the existence of true dimer order [87, 88]. Motivated by the experiments of quasi-one dimensional organic compound  $(Per)_2[Pt(mnt)_2]$  [89, 3], we explore the nature of this dimer order and provide detailed numerical evidence of the dimer order for the localized spins. We also find a coexisting bond order wave (BOW) in this regime with simultaneously phase transition along with the dimer state.

The simplest dimer state appears in the one dimensional Heisenberg model with nearest and next nearest neighbor coupling. If the next nearest neighbor coupling is large enough every neighboring pair of spins forms an independent singlet state [22]. The order parameter of the dimer states  $\langle D \rangle$  is defined by the difference of neighboring spin bonds as given in

Equation 3.5, where  $S_i$  refers to the localized spin at site  $i$ .

$$\begin{aligned} \langle D \rangle &= \lim_{L \rightarrow \infty} \langle D(L) \rangle \\ \langle D(L) \rangle &= \sum_i^L (-1)^i D_i = \sum_i^L (-1)^i \langle S_i \cdot S_{i+1} \rangle \end{aligned} \quad (3.5)$$

Using finite size DMRG, we show a robust dimer pattern in real space without any pinning field in the intermediate coupling regime at  $n = 0.5$  for the localized spins. As an example given in Figure 3.7(a), the dimer order becomes almost uniform away from the boundary. Besides the dimer order, the BOW is identified at the same regime with the order parameter defined similarly as the dimer order.

$$\begin{aligned} \langle B \rangle &= \lim_{L \rightarrow \infty} \langle B(L) \rangle \\ \langle B(L) \rangle &= \sum_i^L (-1)^i B_i = \sum_{i\sigma}^L (-1)^i \langle C_{i\sigma}^\dagger \cdot C_{i+1\sigma} + H.c. \rangle \end{aligned} \quad (3.6)$$

As shown in Figure 3.7(b) the order parameter of BOW also becomes uniform away from the boundary, suggesting that there are different orders for the electrons and the localized spins.

The dimer orders are extrapolated into the thermodynamic limit using various lattice sizes. As shown in Figure 3.8(a), in the dimer phase the dimer order has a slight decrease over lattice sizes, and remains finite after the extrapolation. When  $J$  is above 1.2, the dimer order becomes zero after the extrapolation. The extrapolated dimer order is given in Figure 3.8(b), where the dimer order increases monotonically from 0 as  $J$  decreases from 1.2, which indicates a quantum phase transition. The charge gap (defined in Equation 3.4) and the BOW order parameter (defined in Equation 3.6) are extrapolated into the thermodynamic limit in a

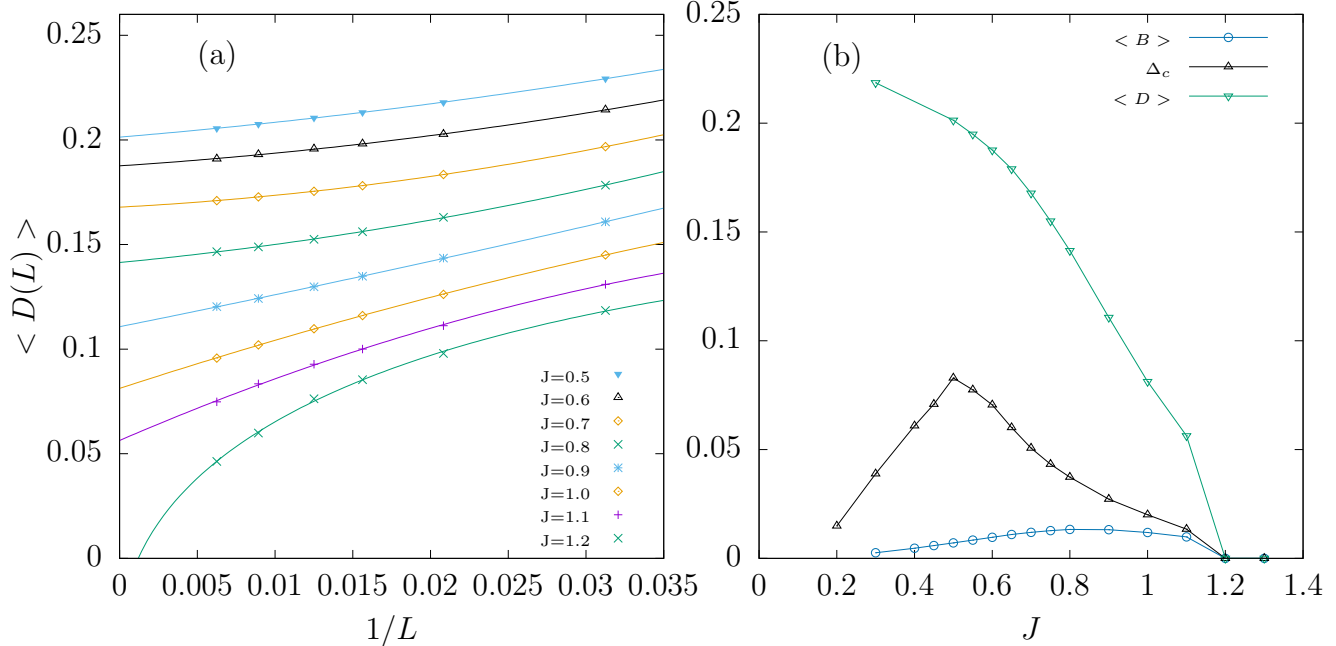


Figure 3.8: (a) refers to the finite size scaling of the dimer order for various  $J$ . We use a least-square fit to the second order of polynomials in  $1/L$ . The order parameter of the dimer phase and bond order wave phase is plotted along with the charge gap in (b). These quantities are obtained after finite size scaling similar to (a).

similar way. The charge gap becomes finite below  $J = 1.2$ , and reaches maximum at  $J = 0.5$ . The BOW order also becomes finite below  $J = 1.2$ , and reaches maximum at  $J = 0.8$ . For extremely small  $J$  the numerical results are hard to converge and we can not be sure whether the charge gap and the order parameters goes to zero at the finite  $J$ . However, based on the results we show a simultaneous quantum phase transition of localized spin dimer state and electron BOW around  $J = 1.2$ .

The spin gap in this insulating phase is calculated for several  $J$  with different lattice sizes and the gap is always zero with an error bar in the order of the truncation error. The localized spins have form a dimer state, but similar to the case of  $n = 0.75$  here the effective electron spin in one unit cell is one half which is reasonable for the gapless spin excitation.

The entanglement entropy for the open boundary system can be studied in the framework

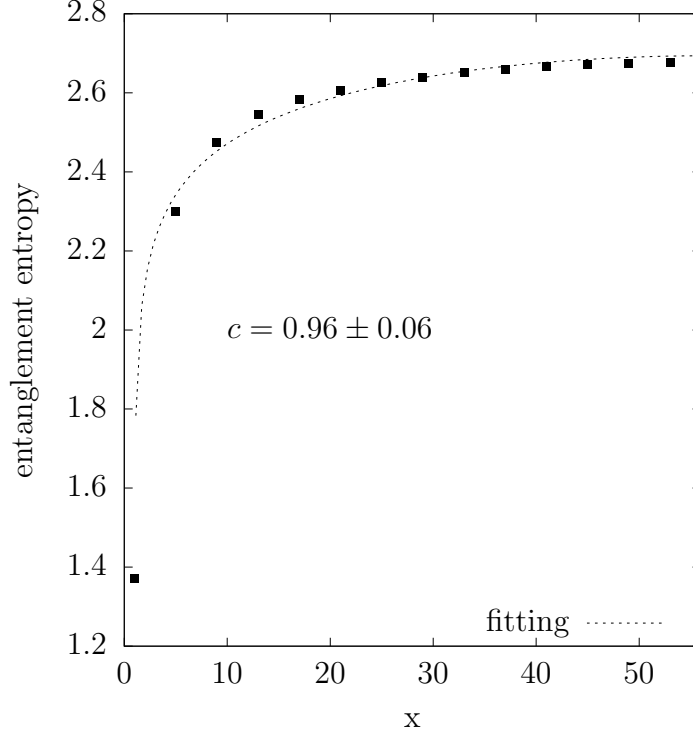


Figure 3.9: The entanglement entropy at  $n = 0.5$ ,  $J = 0.6$  obtained by the finite size lattice of  $L = 112$ . Only half of the lattice is shown. The dash line refers to the fitting using Equation 3.7.

of the conformal field theory [90]. As shown in Figure 3.9, we plot the entanglement entropy versus subsystem size in the insulating state at  $n = 0.5$ ,  $J = 0.6$  on a finite size lattice of  $L = 112$ . The entanglement entropy shows a logarithmic dependence and follows the general equation below.

$$S(x) = \frac{c}{6} \ln \left[ \frac{L}{\pi} \sin \left( \frac{x\pi}{L} \right) \right] + g \quad (3.7)$$

Here  $S(x)$  is the entanglement entropy of the subsystem by cutting at site  $x$ .  $L$  is the whole lattice size,  $c$  is the central charge, and  $g$  is a non-universal constant. The fitting gives the central charge  $c \approx 1$ , which is consistent with the gapless spin excitations.

The dimer order for the localized spins is a result of the RKKY interactions, which is a

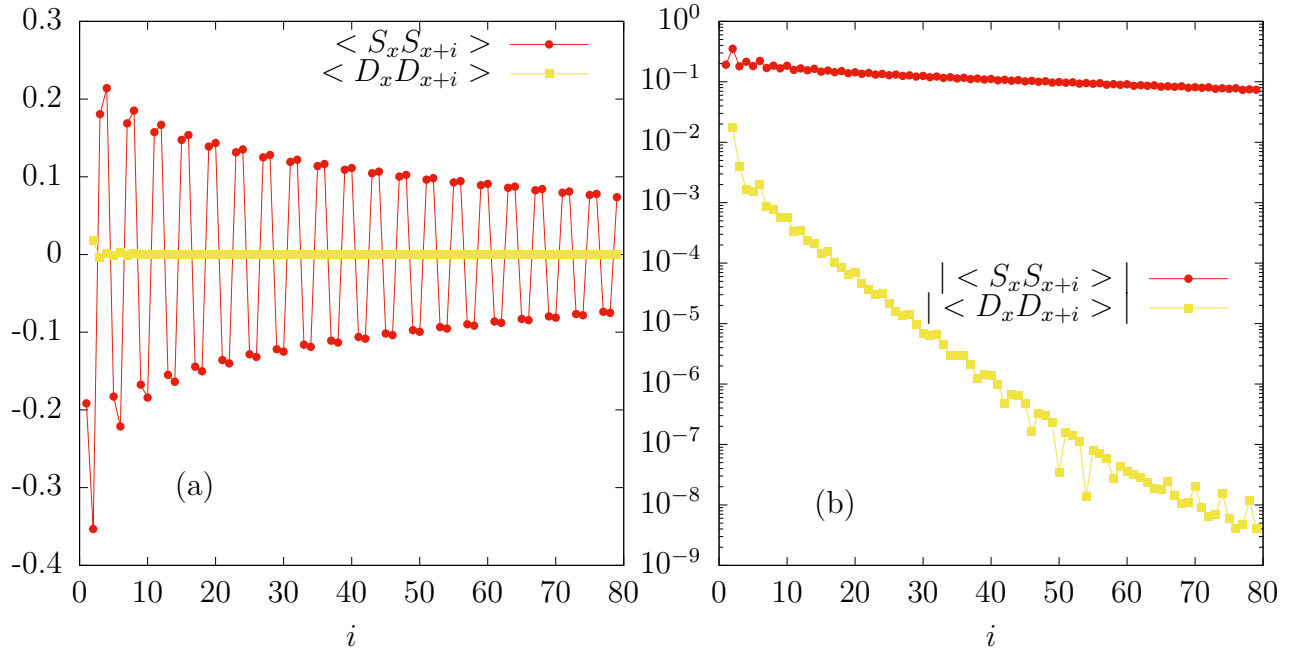


Figure 3.10: The red line in (a) refers to the spin correlations and the yellow line in (a) refers to the dimer correlations. The results are obtained on a  $L = 160$  lattice with  $n = 0.5$ ,  $J = 0.6$  and  $x$  is chosen to be  $\frac{L}{4}$  in order to minimize the boundary effect. (b) is the same correlations with log scale in the y-axis showing the correlation decay over distance.

long-ranged effective interaction with staggered signs. Thus we expect this dimer phase to be different than the dimer phase that exists in the extended Heisenberg model. The spin correlation functions of the localized spins is given by the red line in Figure 3.10(a), where there exists strong spin correlations with slow power-law decay. The spin correlations have a period of 4 which is doubled the period of the local dimer order. This is because the dimer phase is caused by the quasi-long ranged correlations between localized spins instead of the formation of singlet state between neighboring spins. The collective behavior of the localized spins can be regarded as two spin spiral states with the same period but a phase shift of  $\frac{\pi}{2}$ .

We further confirm the nature of this exotic dimer state by obtaining the dimer correlations. As shown in Figure 3.10(b), the dimer correlation has an exponential decay over distance, and it is much smaller than the spin correlation. This result is obtained under

the open boundary condition on a finite size lattice. A more complete study of the dimer correlation would be under the periodic boundary condition, but we have found that it is hard to reach numerical convergence even for a small lattice of  $L = 32$  under the periodic boundary condition. However, the robust dimer order in the absence of pinning field and the periodic pattern in spin correlation functions are consistent with the emergence of the exotic dimer phase in this regime.

The organic compound  $(Per)_2[Pt(mnt)_2]$  is shown to be the experimental realization of the one dimensional Kondo lattice [3], and could be best explained by our numerical results. In particular, the perylene chain in the compound is metallic with quarter filled electrons and the  $Pt(mnt)_2$  chain is insulating with half filled electrons that could be considered as localized spins. The weak interactions between the electrons in these two different chains make it an effective one dimensional weakly coupled Kondo lattice at  $n = 0.5$ . At low temperature this compound shows a combination of spin-Peierls transition for the insulating stack, and the CDW order for the metallic stack [91, 92, 93, 94, 89]. The experimental measurement of different properties of the compound shows that the spin-Peierls and CDW phase transition occurs at almost the same temperature [95, 96]. Our numerical results also show a simultaneous phase transition at intermediate  $J$ . The only difference between the BOW and the CDW is the position of the peak of the wave. For CDW the peak is at the site, while for BOW the peak is at the bond. Thus they are hard to distinguish in experiments. In addition, the spin-Peierls transition into the dimer phase agrees with the finite dimer order identified in the intermediate regime.

We have identified a coexisting localized spin dimer order and electron BOW in the intermediate  $J$  at  $n = 0.5$ . The localized spins are mediated by the RKKY long-ranged interactions that results in a strongly correlated dimer state. This exotic dimer state is qualitatively different from the dimer phase in the extended Heisenberg model where every

neighboring spins form a singlet state. Our results show that the Kondo interactions between electrons and localized spins can induced a simultaneous phase transition for both sides, which agrees with the experimental findings on the organic compound  $(Per)_2[Pt(mnt)_2]$ . Although the results are restricted in one dimension, it provides a new mechanism of the interaction driven phase transition and a hindsight to the Kondo physics.

# Chapter 4

## The spin- $\frac{1}{2}$ XY honeycomb model

### 4.1 Topological phase of matter

As a concept in geometry, topology studies the invariance of continuous deformation of space. In condensed matter physics, there are similar topological invariance defined in the Brillouin zone of the reciprocal lattice, and it can be related to the physical properties measured in experiments. Such examples include the Berry phase in the Aharonov-Bohm effect [97], and the quantum Hall states with gapless edge excitations [98, 99].

The topological phase often has no conventional order parameter as opposed to the charge density wave, superconducting state, magnetic ordering state, and so on. The famous example is given by the Haldane phase in the one dimensional spin-1 Heisenberg model [26]. The Hamiltonian is given as

$$H = J \sum_i (\vec{S}_i \cdot \vec{S}_{i+1} + D(S_i^z)^2) \quad (4.1)$$

As shown in Figure 4.1, the spin gap closes as we vary the parameter  $D$  (assuming  $J = 1$ ), suggesting a quantum phase transition. However, there is no spontaneously symmetry

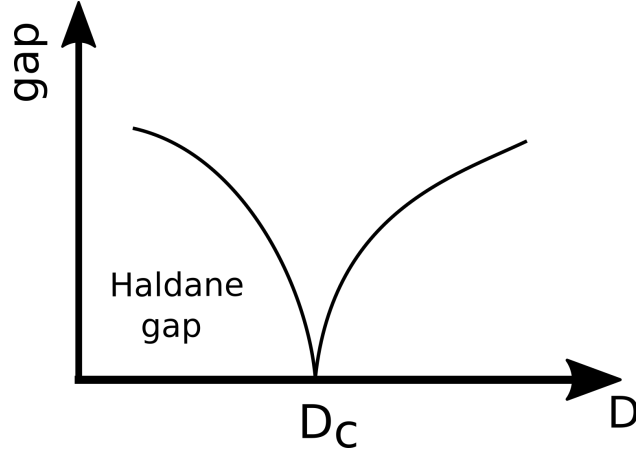


Figure 4.1: The schematic diagram of the gap in Haldane phase.

breaking and no magnetic order. The unique properties of the Haldane phase is that there is a free effective spin- $\frac{1}{2}$  on each edge for a finite size lattice under the open boundary. This kind of transition into a topologically non-trivial state is called the topological phase transition. There is one type of topological states with non-abelian anyonic excitations, which is a potential candidate for topological quantum computer [33].

Most topological states involve a gapped bulk and gapless edge excitations. For electronic system this means that it is an insulator in the bulk and metallic on the edge. Similar properties can be achieved in the spin systems with the help of frustration and competing orders. This is regarded as the topological spin liquids [27].

The spin liquids feature a highly frustrated phase with long range ground state entanglement [100, 101] and fractionalized quasi-particle excitations [102, 103, 104] in the absence of conventional order. Among various kinds of spin liquids, the chiral spin liquids (CSL), which have gapped bulk and gapless chiral edge excitations, is proposed by Kalmeyer and Laughlin [105]. It has a nontrivial topological order, and belongs to the same topological class as the fractional quantum Hall states.

In recent years, there have been extensive studies to identify the CSL in realistic spin models on different geometries such as Kagome [106, 107, 108, 109, 110], triangle [111, 23,

112, 113], square [114, 115], and honeycomb lattices [116]. The CSL state has fractional chiral edge excitations that could be determined by the Chern number through spin pump over flux insertion in numerical calculations. It also has a non-trivial topological order associated with the Chern number. In addition, the CSL has a non-zero chiral order that breaks the time reversal symmetry, similar to the fractional quantum Hall states. The non-zero chiral order is often used as the first clue that indicates a CSL.

## 4.2 Analytical prediction of the chiral spin liquid

Interestingly, for the spin- $\frac{1}{2}$  XY model on honeycomb lattice theoretical studies have suggested the existence of a CSL in the highly frustrated regime that is generated by the staggered Chern-Simons flux with nontrivial topology [117, 118]. Here we will map the Hamiltonian of the spin XY model into the honeycomb Haldane model using Chern-Simons fermionization following Ref. [117]. The Hamiltonian of the XY model is

$$H = J_1 \sum_{\langle i,j \rangle} (S_i^+ S_j^- + h.c.) + J_2 \sum_{\langle\langle i,j \rangle\rangle} (S_i^+ S_j^- + h.c.) \quad (4.2)$$

where  $J_1$  refers to the nearest neighbor coupling and  $J_2$  refers to the next nearest neighbor coupling. The positive  $J_1$  and  $J_2$  will result in frustration in the ground state, and the intermediate regime of  $J_2$  has the most frustration. The spin couplings are only in the xy-plane.

The Chern-Simons fermionization which maps the spin operators by the spinless Fermion operators attached to a string operator, is defined as

$$S_r^{(\pm)} = c_r^{(\pm)} e^{\pm i \sum_{r' \neq r} \arg[r-r'] \hat{n}_{r'}} \quad (4.3)$$

where  $\arg[r]$  is the angle of the vector  $r$  defined in two dimensions and  $\hat{n}_r$  is the number

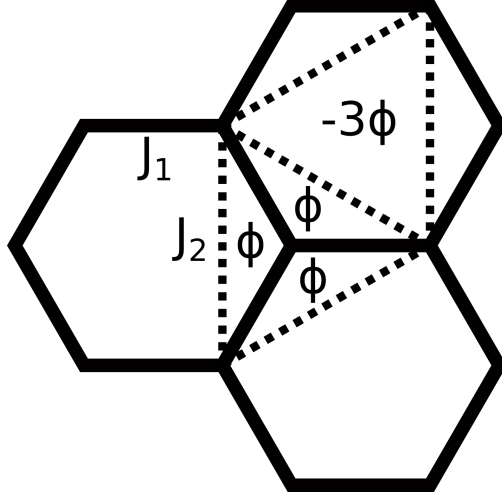


Figure 4.2: The illustrating plot of the XY model Hamiltonian after Chern-Simons fermionization. The dash lines indicate a unit cell.

operator of the spinless fermion. The hard-core condition is automatically satisfied because only one fermion is allowed per site. The spin up state corresponds to the one fermion state and the spin down state corresponds to zero fermion state. Using Equation 4.3 we can derive the Hamiltonian in terms of fermions hopping in the existence of a magnetic flux.

$$H = J_1 \sum_{\langle r,r' \rangle} c_r^\dagger c_{r'} e^{iA_{r,r'}} + J_2 \sum_{\langle\langle r,r' \rangle\rangle} c_r^\dagger c_{r'} e^{iA_{r,r'}} + h.c. \quad (4.4)$$

Here we have  $A_{r,r'} = \sum_{r''} (\arg[r - r''] - \arg[r' - r'']) \hat{n}_{r''}$ . The unique properties of  $A_{r,r'}$  allow us to define the Chern-Simons magnetic field on site  $r$  as

$$B_r = A_{r+e_1, r+e_2} + A_{r+e_2, r+e_3} + A_{r+e_3, r+e_1} = 2\pi \hat{n}_r \quad (4.5)$$

Looking for the mean-field solutions motivated by the numerical results of antiferromagnetic ground state, we can gauge out the uniform component of the magnetic flux at half filling, which corresponds to total  $S_z = 0$  in terms of the spins. The resulting Hamiltonian

has a staggered flux with net zero in the unit cell, as shown in Figure 4.2. In the intermediate regime of  $J_2$  this Hamiltonian could be mapped into the Haldane Hamiltonian with nontrivial topological bands. This suggests that the ground state of the intermediate regime of  $J_2$  is a non-uniform chiral spin liquid with antiferromagnetic ordering in the  $z$  direction on the mean-field level.

### 4.3 Global phase diagram

Although the CSL is predicted analytically in the intermediate  $J_2$  regime, so far there is no direct numerical evidence supporting this claim [119, 120, 24, 121, 122, 123, 124, 125], leaving the possible existence of a CSL in the honeycomb XY model as an open question.

Aside from the possible CSL, the XY model itself is expected to have a rich phase diagram because of the frustration induced by the next-nearest-neighbor coupling  $J_2$ . As the reminiscent of the debated intermediate phase in numerical studies, density matrix renormalization group (DMRG) [24, 123] and coupled cluster method [125] studies suggest an Ising antiferromagnetic state. However, exact diagonalization (ED) [119, 126] and quantum Monte Carlo method studies [120, 127] suggest a Bose-metal phase with spinon Fermi surface [128]. A very recent numerical study using ED reveals an emergent chiral order but the phase remains a topologically trivial chiral spin state [129]. Up to now, the theoretical understanding of the phase diagram for honeycomb XY model is far from clear.

Using large scale DMRG [8, 9] method, we identify the global quantum phase diagram in the presence of the nearest, next-nearest XY spin couplings and three-spins chiral interactions  $\vec{S}_i \cdot (\vec{S}_j \times \vec{S}_k)$ . We also provide strong numerical evidence of the long-sought CSL in the extended spin- $\frac{1}{2}$  XY model on the honeycomb lattice and clarify the conditions for such a phase to emerge (the results have been published [130]). While there are only magnetic ordered phases in the absence of the chiral couplings, the CSL emerges with finite chiral

interactions, where the minimum  $J_\chi$  required for the emergence of the CSL appears in the intermediate  $J_2$  regime. This suggests a possible multi-critical point in the phase diagram, neighboring between Ising antiferromagnetic order, collinear/dimer order, and the CSL.

The CSL is identified in the extended regime above the XY-Neel state and the Ising antiferromagnetic state induced by chiral interactions. We also obtain a chiral spin state at large  $J_\chi$  with finite chiral order. The chiral spin state shows peaks in the spin structure factor that increase with system sizes, indicating a magnetic ordered state. The phases we find without the chiral term agree with previous numerical studies using DMRG [24]. Our results demonstrate the importance of the interplay between the frustration and chiral interactions, which leads to a rich phase diagram.

We investigate the extended spin- $\frac{1}{2}$  XY model with a uniform scalar chiral term using both infinite and finite size DMRG methods [65, 131] in the language of matrix product states [48]. We use the cylindrical geometry with circumference up to 6 (8) unit cells in the finite (infinite) size systems except for the calculations of spin gap, which is based on smaller size tori.

The Hamiltonian of the XY model with chiral interactions is given as

$$\begin{aligned}
 H = J_1 \sum_{\langle i,j \rangle} (S_i^+ S_j^- + h.c.) + J_2 \sum_{\langle\langle i,j \rangle\rangle} (S_i^+ S_j^- + h.c.) \\
 + J_\chi \sum_{i,j,k \in \Delta} \vec{S}_i \cdot (\vec{S}_j \times \vec{S}_k)
 \end{aligned}
 \tag{4.6}$$

here  $\langle i, j \rangle$  refers to the nearest-neighbor sites and  $\langle\langle i, j \rangle\rangle$  refers to the next-nearest-neighbor sites.  $\{i, j, k\}$  in the summation  $\sum_\Delta$  refers to the three neighboring sites of the smallest triangle taken clockwise as shown in Figure 4.3. The chiral term could be derived as an effective Hamiltonian of the extended Hubbard model with an additional  $\Phi$  flux through each elementary honeycomb [107, 116, 132, 34]. We set  $J_1 = 1$  as the unit for the energy

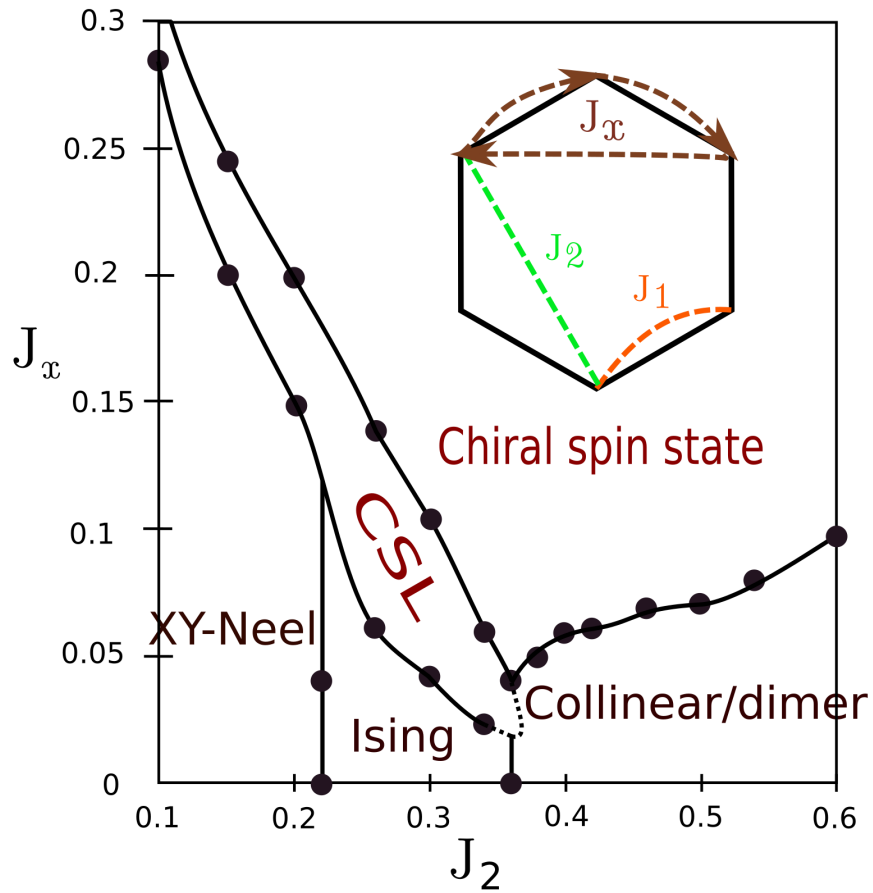


Figure 4.3: The schematic phase diagram of the extended XY model for  $0.1 < J_2 < 0.6$  and  $0 < J_x < 0.3$ , based on the results from cylindrical circumference of 4 unit cells. The CSL is identified in the intermediate regime.

scale, and use the spin U(1) symmetry for better convergence.

The ground state phase diagram is illustrated in Figure 4.3. We use spin structure factors to identify magnetic ordered phases, and entanglement spectrum to identify the topological ordered CSL. For larger  $J_\chi$ , a magnetic ordered chiral spin state with nonzero scalar chiral order is also identified.

The static spin structure in the Brillouin zone is defined as

$$S(\vec{q}) = \frac{1}{N} \sum_{i,j} \langle \vec{S}_i \cdot \vec{S}_j \rangle e^{i\vec{q} \cdot (\vec{r}_i - \vec{r}_j)} \quad (4.7)$$

In the XY-Neel phase there are peaks at the Brillouin zone  $\Gamma$  points in the static spin structure as shown in the inset of Figure 4.4(a). The magnitude of the peak is plotted as a function of  $J_\chi$  in Figure 4.4(a). It decreases rapidly as  $J_\chi$  increases, and disappears as the system transits into the CSL at  $J_\chi \approx 0.15$ . Similarly, the peak for the collinear order at various  $J_\chi$  is given in Figure 4.4(b). The inset of Figure 4.4(b) shows the spin structure at  $J_\chi = 0.01$  where the phase is dominant by the collinear order. The phase boundary could be identified by the sudden drop and the disappearance of the peak at  $J_\chi \approx 0.06$ . In the intermediate regime at  $J_2 = 0.3$  and small  $J_\chi$ , the staggered on-site magnetization serves as the order parameter as shown in Figure 4.4(c), where the three corresponding phases from left to right are Ising antiferromagnetic state, CSL, and chiral spin state. This quantity shows a sudden drop from the Ising antiferromagnetic state to the CSL at  $J_\chi \approx 0.04$ , which determines the phase boundary as illustrated by the left dash line. The right dash line is determined by the vanish of quasi-degenerate pattern in the entanglement spectrum.

In order to test the finite size effect we study larger systems in both x and y-directions. While the CSL is robust in various sizes, the critical  $J_\chi$  of the phase boundary between the Ising antiferromagnetic state and the CSL in the intermediate regime may vary slightly. Here we show one example at  $J_2 = 0.3$  in Figure 4.5. The critical  $J_\chi$  increases by 0.01 as  $L_x$

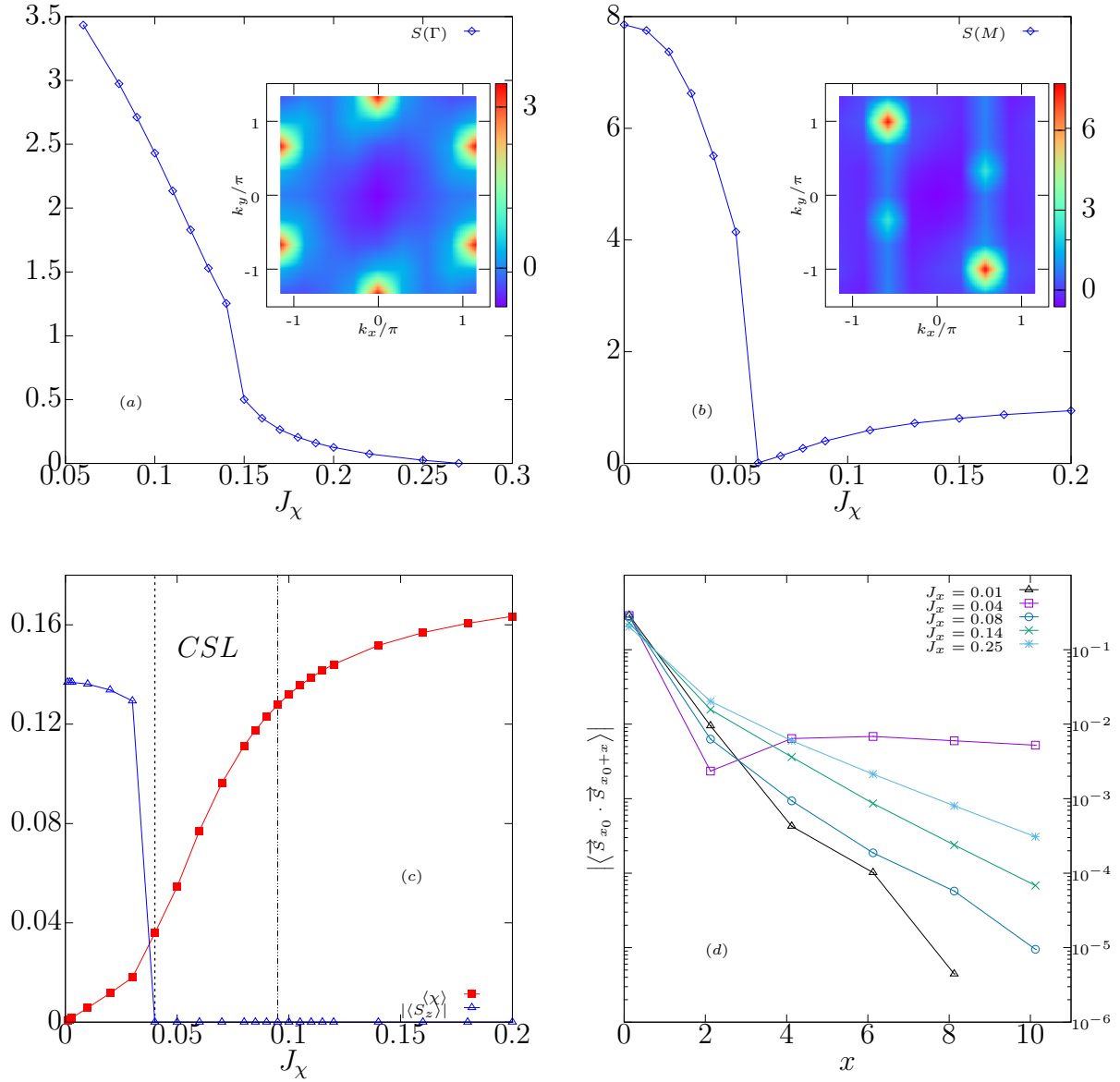


Figure 4.4: (a) shows the peak value at  $\Gamma$  point in the spin structure  $S(q)$  at  $J_2 = 0.2$  for various  $J_\chi$ . The inset of (a) is the spin structure of the XY-Neel order at  $J_2 = 0.2$ ,  $J_\chi = 0.06$ , where there are clear peaks at the  $\Gamma$  points in the second Brillouin zone. (b) is the  $M$  point peak value at  $J_2 = 0.4$  for various  $J_\chi$ . The inset of (b) is the spin structure of the collinear order at  $J_2 = 0.4$ ,  $J_\chi = 0.01$ , where the dominant peak is located at the  $M$  points in the second Brillouin zone. (c) shows the antiferromagnetic order (blue line) and the scalar chiral order (red line) at  $J_2 = 0.3$  for various  $J_\chi$ . (d) refers to the spin correlations at  $J_2 = 0.3$  for various  $J_\chi$ . The phases at  $J_\chi = 0.01, 0.04, 0.08$ , and  $0.14(0.25)$  refer to Ising antiferromagnetic state, phase boundary, CSL, and chiral spin state respectively. The  $x_0$  is chosen away from the open boundary, and  $x$  refers to the horizontal distance between the two spins. The plots above are based on finite DMRG results with  $L_y = 4 \times 2$ .

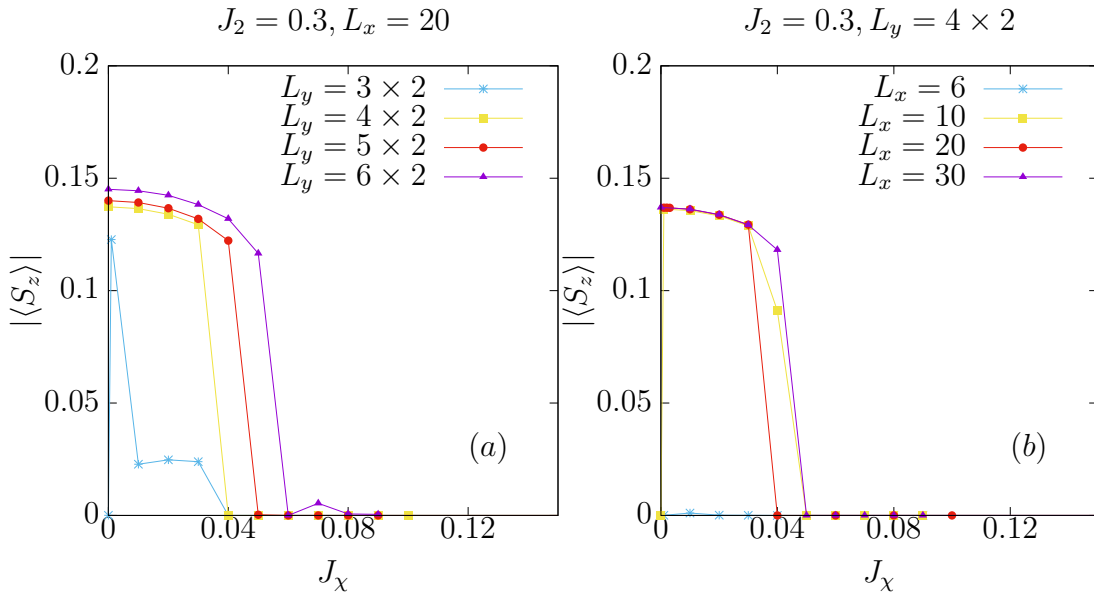


Figure 4.5: The staggered magnetization for various lengths in the x-direction (Figure 4.5(a)) and the y-direction (Figure 4.5(b)) in the intermediate regime. The phase transition from the Ising antiferromagnetic state to the CSL is determined by the sudden drop of  $|\langle S_z \rangle|$ . For the smallest size in (a) ( $L_x \times L_y = 20 \times 3 \times 2$ ) and (b) ( $L_x \times L_y = 6 \times 4 \times 2$ ) we found that  $|\langle S_z \rangle| = 0$  at zero  $J_\chi$  limit due to finite size effect.

increases from 20 to 30 while keeping  $L_y$  fixed, and it increases by 0.02 when  $L_y$  increases from  $4 \times 2$  to  $6 \times 2$  with fixed  $L_x$ . The finite size scaling indicates that the phase transition into CSL happens at  $J_\chi > 0.06$  in the thermodynamic limit.

Besides the magnetic order parameters, other properties such as the spin correlation, the entanglement entropy and spectrum are also used to identify the phase boundary. We have found consistence in those different measurements. As shown in Figure 4.4(d), the spin correlations are strongly enhanced at  $J_\chi \approx 0.04$  near the phase boundary between the Ising antiferromagnetic phase and the CSL, while both phases have exponentially decaying spin correlations. The phase boundary determined by the spin correlation is the same as the one by the staggered magnetization.

Both CSL and the chiral spin state in the larger  $J_\chi$  regime have a finite scalar chiral

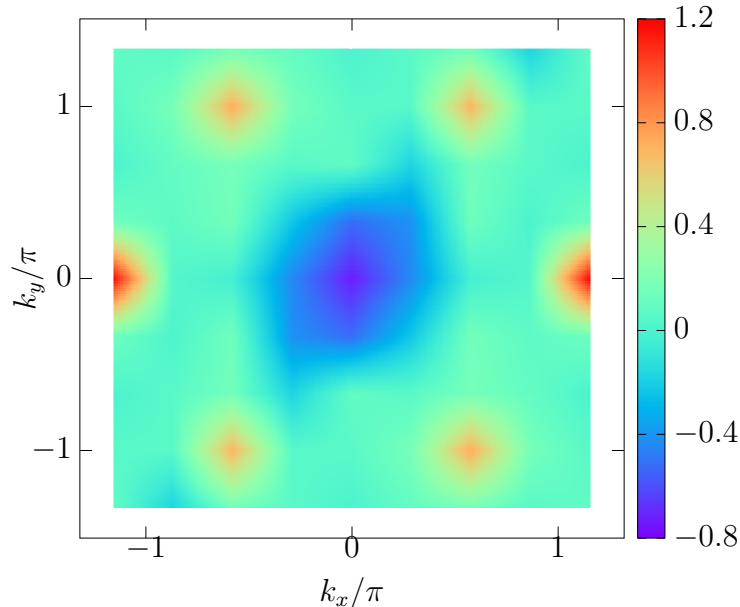


Figure 4.6: The spin structure in the chiral spin state at  $J_2 = 0.2$ ,  $J_\chi = 0.27$  using finite size cylinder of  $L_x \times L_y = 20 \times 4 \times 2$ , which peaks at the  $M$  points in the second Brillouin zone.

order that is defined as

$$\langle \chi \rangle = \frac{1}{3N} \sum_{i,j,k \in \Delta} \vec{S}_i \cdot (\vec{S}_j \times \vec{S}_k) \quad (4.8)$$

As shown by the red curve in Figure 4.4(c), the chiral order increases monotonically with the increase of  $J_\chi$  in the CSL and chiral spin state, and saturates around  $\langle \chi \rangle \approx 0.177$ . The spin correlations in these two states are given in Figure 4.4(d) as examples at  $J_\chi = 0.08$ , and 0.14(0.25) respectively, where they remain exponentially decay. However, the spin correlation increases generally as  $J_\chi$  increases. As shown in Figure 4.11(b), for the parameters we labeled as chiral spin state, the spin structure factors show sharp peaks, with the magnitudes of the peak values increasing with system sizes, suggesting a magnetic ordered state in the larger  $J_\chi$  regime. We also notice that the spin structure in this chiral spin state shares the same

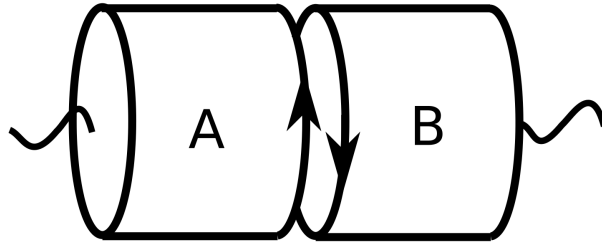


Figure 4.7: The creation of the edge by cutting the infinite long cylinder in half.

peaks as the tetrahedral phase [116, 133] as shown in Figure 4.6, and we do not rule out the possibility of tetrahedral magnetic order in this regime.

The extended regime of  $J_2 > 0.6$  and  $J_2 < 0.1$  are not our main focus because we are interested in the intermediate  $J_2$  regime with strong frustration, but we do find that the CSL extends to a relatively large  $J_\chi \approx 0.5$  at  $J_2 = 0$ . This implies that the CSL could survive even without the frustration induced by second nearest neighbor interactions in the XY model, which may be interesting for future study. In the regime labeled as collinear/dimer, we also find a non-magnetic dimer ground state in close competition with the collinear state at  $J_\chi > 0.55$ . As pointed out in Ref. [24], the actual ground state depends on the system size and XC/YC geometry.

The phase near the critical point of  $J_2 \approx 0.36$ ,  $J_\chi \approx 0.02$  is hard to define numerically because different spin orders are mixed together in the low energy spectrum, thus the spin correlation is generally large. Here the phase boundary is measured by the unique properties of the CSL through the entanglement spectrum as discussed below, and it will be marked by the dash line as a guide to the eye in Figure 4.3.

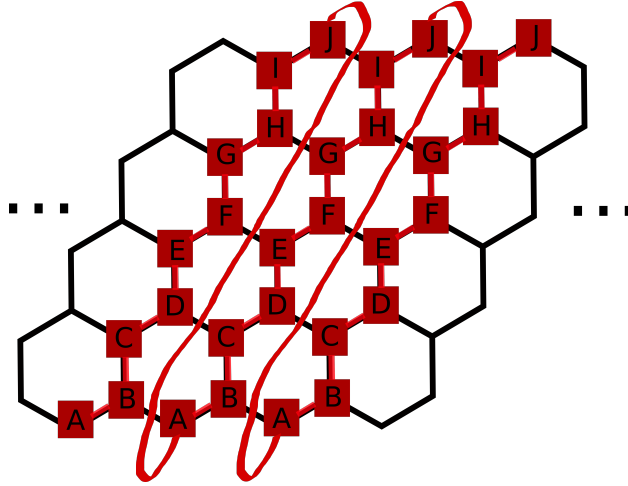


Figure 4.8: The matrix product state representations of the infinite long cylindrical system.

## 4.4 Numerical evidence of the chiral spin liquid

The CSL can be characterized by the twofold topological degenerate ground states, which are called ground state in vacuum and spinon sectors [106, 134], respectively. The spinon sector refers to a spin- $\frac{1}{2}$  excitation on the edge of the system, and the vacuum sector has no such excitation. The excitation is gapless which is why the two states are degenerate. Using infinite size DMRG with finite size in one direction under periodic boundary conditions and infinite size in the other direction, we can obtain the ground state of the CSL with no edge. The edge can be created by cutting the system in half, as shown in Figure 4.7. This is done by cutting the bond which connects the neighboring matrix product state as illustrated in Figure 4.8, and we can calculate the entanglement spectrum (ES) of the subsystem.

The ES of the system corresponds to the physical edge spectrum [135, 136, 137]. We can express the low energy edge Hamiltonian of the configuration in Figure 4.7 as

$$H_{edge}(\lambda) = H_L + H_R + H_{int}(\lambda) \quad (4.9)$$

where  $\lambda$  is the interaction strength between the two subsystems, and the quantum entanglement between the two subsystems as

$$\rho_L = \text{Tr}_R |G\rangle\langle G| = e^{-H_E} \quad (4.10)$$

where the ES are the eigenvalues of  $\rho_L$ , and  $|G\rangle$  is the ground state of the edge Hamiltonian. The one dimensional free edge state could be described by the (1+1) conformal field theory. The conformal invariant boundary states are in certain forms (Ishibashi states [138]) that allows us to make a connection between the edge Hamiltonian and the entanglement Hamiltonian ( $H_E$ ) as [135]

$$\rho_{La} \simeq Z_a^{-1} \widehat{P}_a e^{-4\tau_0 H_L} \widehat{P}_a \quad (4.11)$$

where  $a$  refers to any topological sector in general. Following the chiral  $SU(2)_1$  conformal field theory [139], the leading ES of a gapped CSL has the degeneracy pattern of 1,1,2,3,5,7... [140].

As shown in Figure 4.9(a) and (b), the ES in the CSL phase has such quasi-degenerate pattern with decreasing momentum in the y-direction for each spin sector. The ES of the spinon ground state has a symmetry about  $S_z = \frac{1}{2}$  which corresponds to a spinon at the edge of the cylinder, while the one of the vacuum ground state has a symmetry about  $S_z = 0$ . The ES is robust in the bulk part of the CSL phase for various parameters and system sizes. However, as we approach the phase boundary, additional eigenstates may also mix in the spectrum. As shown in Figure 4.10(a), the counting of the quasi-degenerate states in the CSL is very clear in every spin sector. In Figure 4.10(b) we can still identify the counting for  $S = 0$  sector near the phase boundary, but additional low-lying eigenstates have already mixed in the the  $S = -1$  and 1 sector. As soon as the system enters the chiral spin state

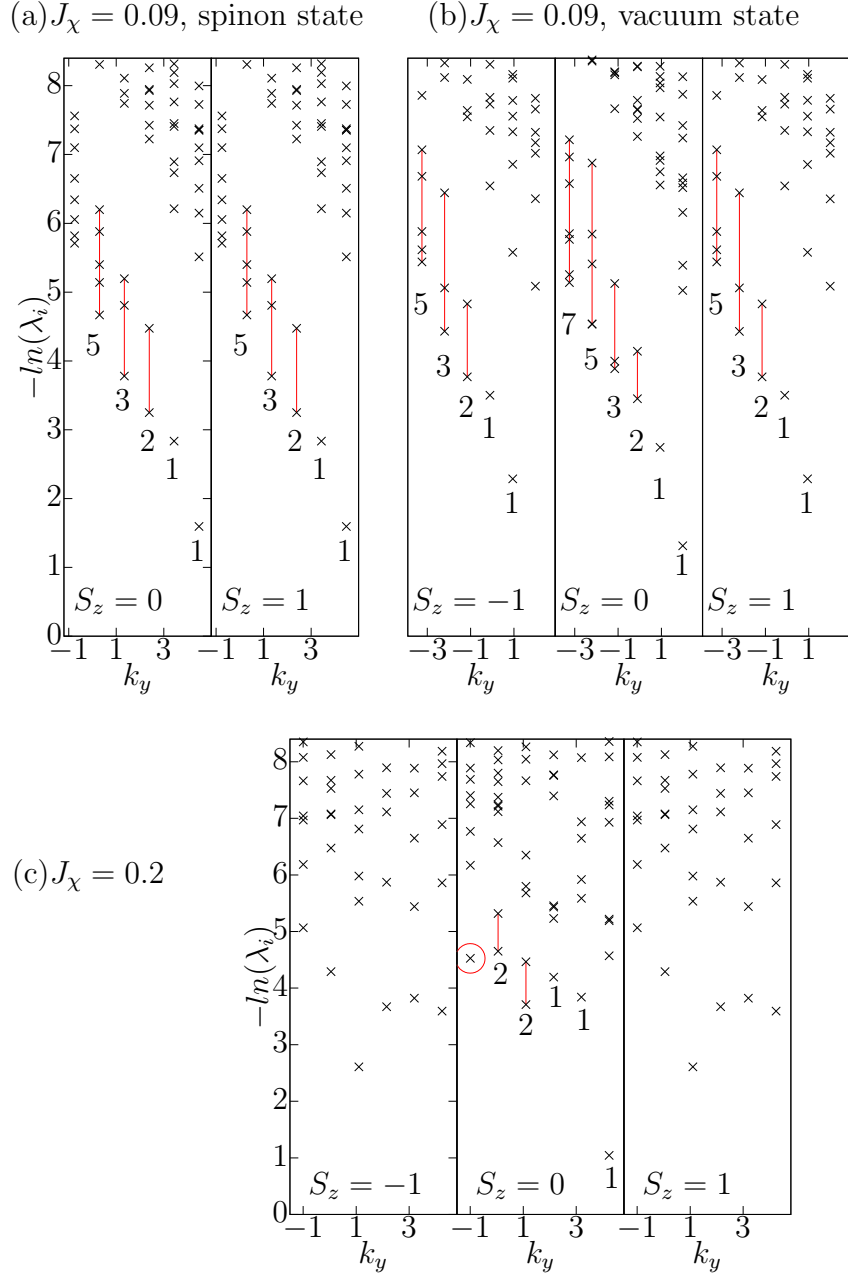


Figure 4.9: The ES for the spinon ground state (a) and the vacuum ground state (b) in the CSL phase at  $J_2 = 0.26$ ,  $J_\chi = 0.09$ , and the ES in the chiral spin state (c) at  $J_2 = 0.26$ ,  $J_\chi = 0.2$  with different spin sectors. The spectrum is calculated using infinite DMRG with  $L_y = 6 \times 2$ . The  $\lambda_i$  refers to the eigenvalues of the reduced density matrix, and the  $k_y$  has an increase of  $\frac{2\pi}{L_y}$ . The quasi-degenerate eigenvalues are labeled by the number below each momentum. Each spin sector is separated with the help of total  $S_z$  conservation implemented in the algorithm.

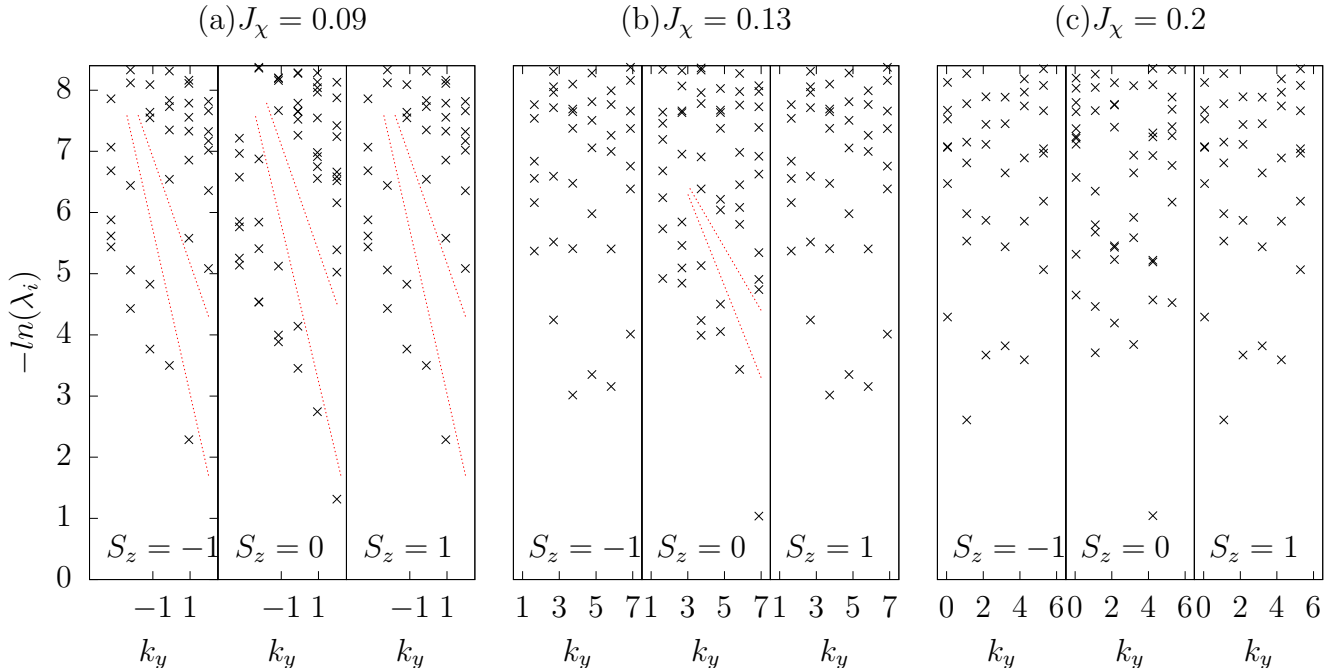


Figure 4.10: The entanglement spectrum in CSL at  $J_\chi = 0.09$  (Figure 4.10(a)), boundary at  $J_\chi = 0.13$  (Figure 4.10(b)), and the chiral spin state at  $J_\chi = 0.2$  (Figure 4.10(c)). All three plots are obtained at  $J_2 = 0.26$ . The dash red lines are guide to the eye.

the counting disappears, as shown in Figure 4.10(c).

The main difference between the CSL and the chiral spin state is the topological edge state that can be identified through the ES. An example of the ES in the chiral spin state is also given in Figure 4.9(c), where the quasi-degenerate pattern disappears and additional low-lying states emerge, as opposed to the ES in the CSL shown in Figure 4.9(a) and (b). The phase boundary between these two states are determined mainly by the ES.

Besides the quasi-degenerate pattern of the ES there are other numerical methods to identify the CSL, which are listed here for future study. These methods have been proven to be unbiased and accurate ways to identify the CSL [137].

1. Insert a flux through the finite cylinder adiabatically and calculate the net spin transfer from one edge to the other. The quantized net spin pump corresponds to the quantized Chern number.

2. Compute the quantum dimensions by entanglement entropy, and compare it with the semion model based on conformal field theory.

3. Obtain the modular S and U matrix by applying a modular transformation on the torus ground state, and compare it with the exact one of a chiral semion model.

The finite chiral order represents the time reversal symmetry breaking chiral current in each small triangle, which is shown in Figure 4.4(c). The chiral order is significantly enhanced as the system undergoes a phase transition from the Ising antiferromagnetic state to the CSL. However, the spin correlation remains following exponential decay, as shown by the line of  $J_\chi = 0.08$  in Figure 4.4(d). We further confirm the vanish of any conventional spin order in the CSL by obtaining the spin structure in Figure 4.11(a), and comparing it with the one in the chiral spin state in Figure 4.11(b). There is no significant peak in the CSL phase as opposed to other magnetic phases.

In order to identify the excitation properties of the CSL, we obtain the spin-1 excitation gap by the energy difference between the lowest state in  $S = 0$  and 1 sector. To measure the bulk excitation gap, we use the torus geometry to reduce the boundary effect. The finite size scaling of the spin gap using rectangle like clusters is shown in Figure 4.11(c). The spin gap decays slowly as the cluster grows, and remains finite after the extrapolation, suggesting a gapped phase in the thermodynamic limit. In addition, we study the entanglement entropy of the subsystems by cutting at different bonds. As shown in Figure 4.11(d), the entropy becomes flat away from the boundary, which corresponds to a zero central charge in the conformal field theory interpretation [90]. This supports a gapped CSL phase that is consistent with the finite spin gap.

To summarize this section, we identify the long-sought CSL with the perturbation of three-spins chiral interactions in the spin- $\frac{1}{2}$  XY model on the honeycomb lattice. The CSL extends to the intermediate regime with a small  $J_\chi$ , providing evidence of the important

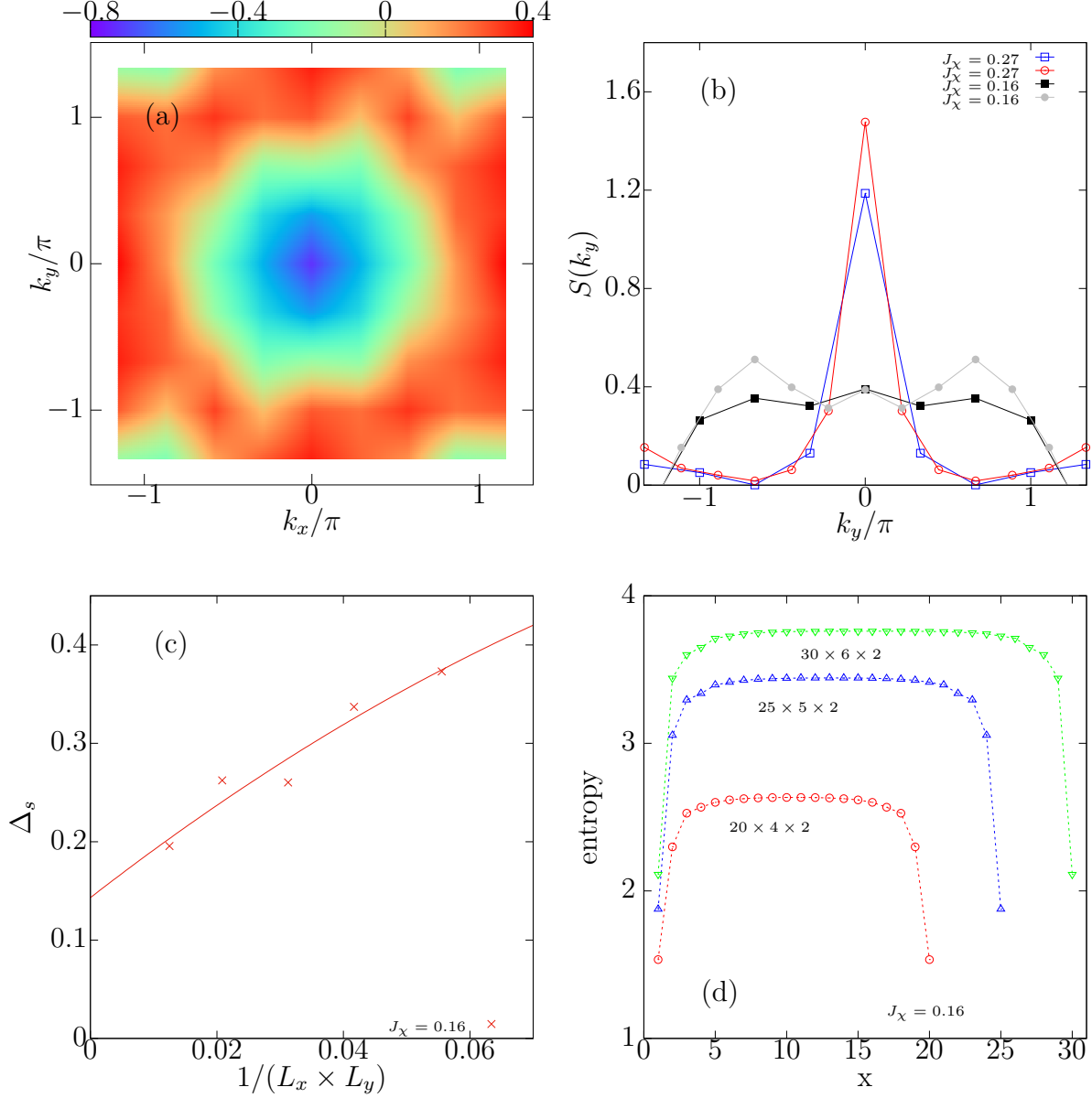


Figure 4.11: (a) refers to the spin structure in the CSL phase at  $J_2 = 0.2$ ,  $J_\chi = 0.16$  where there is no peak as opposed to other magnetic phases. This result is based on the cluster of  $20 \times 4 \times 2$ . (b) refers to the spin structure peaks with fixed  $k_x = -\frac{2\pi}{\sqrt{3}}$  of various parameters. The blue and red lines are obtained in the chiral spin state with clusters of  $20 \times 4 \times 2$  and  $30 \times 6 \times 2$ , respectively. The magnitude of the peak increases as the cluster size increases. The black and grey lines are obtained in the CSL with the same two clusters, where there is no significant peak. (c) refers to the finite size scaling of the spin gap on the torus geometry with clusters of  $3 \times 3 \times 2$ ,  $4 \times 3 \times 2$ ,  $4 \times 4 \times 2$ ,  $6 \times 4 \times 2$ , and  $8 \times 5 \times 2$ . (d) refers to the entanglement entropy with various clusters on finite cylinders in the CSL phase. The  $x$  here denotes the distance of the cut in the  $x$  direction. All of the results are obtained at  $J_2 = 0.2$ .

interplay between frustration and chiral interactions driving the CSL. Here, we demonstrate that the chiral interactions are essential for the emergence of the CSL, because the minimum critical  $J_\chi$  of the phase transition is around 0.02, which is stable against the increasing of system sizes.

A chiral spin state is also obtained at larger  $J_\chi$ , which extends to the wider regime of  $J_2$ . The chiral spin state has a peak value for spin structure factor growing with system sizes. Further studies include finding the exact nature of this chiral spin state, and the nature of the phase transition into the CSL.

Experimentally, of all the honeycomb materials that show a quantum-spin-liquid-like behavior [141, 142, 143], the Co-based compounds are mostly studied in the context of XY model such as  $BaCo_2(PO_4)_2$  [144, 145] and  $BaCo_2(AsO_4)_2$  [146], thus it would be extremely interesting to search for the quantum spin liquid in such model. On the other hand, the results of CSL may be tested in cold atoms experiments [147, 148] because the spin XY model could be mapped by the bosonic Kane-Mele model in the Mott regime [129, 149].

# Chapter 5

## The magic angle physics in twisted bilayer graphene

### 5.1 Constructing an effective two-leg ladder

The twisted bilayer graphene (TBG) refers to two graphene layers which rotates by a small angle away from its superposition. At the angle of  $\sim 1^\circ$ , there are some unexpected physical properties and it is called the magic angle [150, 151, 152]. As a result, the low energy band becomes quasi-flat, and the kinetic energy is reduced. Under the doping of electrons the system becomes a superconductor at low temperature [153, 154, 155, 156, 157].

The effects of the correlations between the electrons becomes important in the TBG because the kinetic energy is reduced, and it can be studied using the DMRG method. However, even the single particle physic is not well understood [158]. The large scale moiré pattern is formed under the magic angle and the unit cell becomes too large for the ab-initio calculations [151]. In addition, the Wannier functions describing the TBG turn out to be not so localized [159, 158], thus it is necessary to come up with alternative approaches that can be used to understand the physics of magic angle in TBG.

Here we define an auxiliary model that mimics the TBG model on both single particle level and many particles level (the results have been published [160]). We show that the two leg ladder with a periodic flux can lead to a quasi-flat low energy band, similar to the magic angle TBG. With Coulomb repulsions inducing the correlations between the electrons at half filling, the system becomes ferromagnetic for spins on each leg as well as between two legs. In addition, this model provides hindsight to the study of 1D magnetism due to electron correlations.

The low energy effective model of a TBG [152, 161] can be described by ( $\hbar = 1$ )

$$h_{1,2} = -iv_0 \begin{pmatrix} 0 & \partial_x - i\partial_y \\ \partial_x + i\partial_y & 0 \end{pmatrix} \quad (5.1)$$

$$h_{\perp} = \frac{\gamma_0}{3} \sum_{n=0}^2 e^{i\delta\mathbf{K}_n \cdot \mathbf{r}} \begin{pmatrix} 1 & e^{-i\frac{2\pi n}{3}} \\ e^{i\frac{2\pi n}{3}} & 1 \end{pmatrix} \quad (5.2)$$

where  $h_{1,2}$  are Dirac Hamiltonians describing the individual layers and  $h_{\perp}$  couples them. Here  $v_0$  is the Dirac velocity of the individual layers,  $\gamma_0$  is the interlayer coupling strength,  $\delta\mathbf{K} = \mathbf{K}^{\theta} - \mathbf{K}$  is the vector that connects the Dirac points of the rotated and the unrotated layers in momentum space, and  $\delta\mathbf{K}_n$  is  $\delta\mathbf{K}$  rotated by an angle of  $2\pi n/3$ . The vector  $\delta\mathbf{K}$  sets the length scale of the Moiré pattern which has a periodicity of  $\frac{4\pi}{3\delta K}$ . The bandwidth of the low-energy bands changes as a function of the parameter  $\alpha = \frac{\gamma_0}{v_0\delta K}$ , and it decreases to almost zero when  $\alpha \sim 1$ .

There are many features in the model of the TBG including a Dirac dispersion, a valley degree of freedom, and the fact that it is a two dimensional system. Here we hope to capture the essence of the TBG model by constructing an auxiliary Hamiltonian by replacing Equation 5.1 and Equation 5.2 with

$$h_{1,2} = -\frac{\partial_x^2}{2m} \quad (5.3)$$

$$h_{\perp} = \gamma(x)e^{i\phi(x)} \quad (5.4)$$

The auxiliary Hamiltonian is unrelated to the original TBG Hamiltonian but the inspiration is obvious. We have replaced the individual graphene layers with one dimensional free electrons while keeping the coupling term complex similar to that in the original TBG Hamiltonian where each element of  $h_{\perp}$  is complex. We impose the condition  $\gamma(x) = \gamma(x+X)$  and  $\phi(x) = \phi(x+X)$  so that  $h_{\perp}$  is periodic as in TBG where  $X$  is the period. To simplify, we assume a constant flux per plaquette  $\phi(x) = 2\pi x/X$ . Also, we assume that  $\gamma(x)$  is a slowly varying function so that we can approximate it as  $\gamma(x) = \gamma_0[1 + g \cos(2\pi x/X)]$ . We can show that the resulting low-energy band structure also has a quasi-flat feature for certain value of  $\gamma_0$  similar to the  $\alpha$  in the TBG model.

## 5.2 Ferromagnetic Mott state

To study the effect of electron-electron interactions on the auxiliary Hamiltonian, we write the corresponding lattice version of the Hamiltonian as

$$\begin{aligned}
 H = & -t \sum_{j,\sigma,\lambda} c_{j+1\sigma\lambda}^{\dagger} c_{j\sigma\lambda} + \sum_{j,\sigma} \gamma_j c_{j\sigma 2}^{\dagger} c_{j\sigma 1} + h.c. \\
 & + U \sum_{j,\lambda} n_{j\uparrow\lambda} n_{j\downarrow\lambda}
 \end{aligned} \quad (5.5)$$

The operator  $c_{j\sigma\lambda}$  annihilates an electron on site  $j$ , on the leg with index  $\lambda = 1, 2$  and spin  $\sigma = \downarrow, \uparrow$ . The hopping parameter between neighboring sites in each leg is  $t$  and between

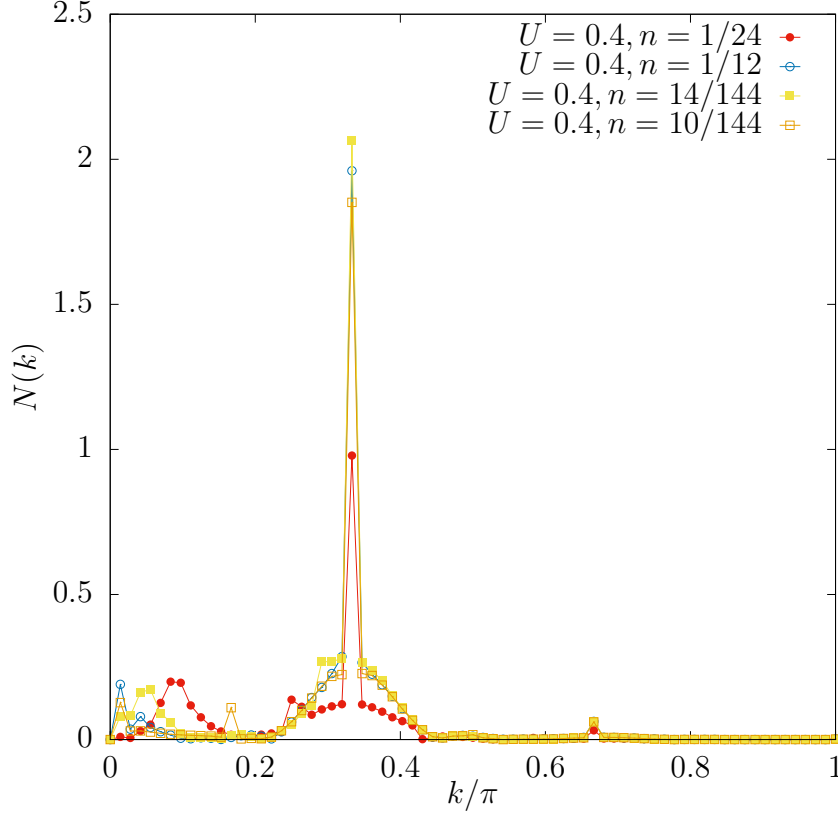


Figure 5.1: The Fourier transform of the electron density at various fillings, with the dominant peaks remain at  $k = \frac{2\pi}{6}$ . The results are obtained at  $L = 144$  in the quasi-flat band regime.

the two legs by  $\gamma_j = \gamma_0 \left(1 + g \cos \frac{2\pi j}{J}\right) e^{i\frac{2\pi j}{J}}$ , where  $\gamma_0$  and  $g$  are constants. In our calculation, we choose  $J$  to be 6 (which is  $X$  in the last section) without any loss of generality, and set  $t = 1$  to fix the energy scale. Interaction is added via an onsite Hubbard interaction of strength  $U$  in the second line, where  $n_{j\sigma\lambda}$  is the electron number operator. We are interested in understanding the effect of interactions when the quasi-flat band is half-filled, so we fix the electron density at  $n = \frac{1}{2J}$ .

Finite size DMRG method with open boundary conditions is used to calculate the ground state properties. The calculations are performed using the ITensor library [65]. To minimize

the finite-size effect we study systems of various lengths up to  $N = 240 \times 2$  with cutoff error less than  $10^{-9}$ . The energy difference between two sweeps is less than  $10^{-7}$  during final sweeps. The total electron number and  $S_z$  conservation are implemented for better convergence.

In order to stay in the quasi-flat band regime we fix  $\gamma_0 = 0.49$  and  $g = 0.1$  so that  $\delta_{BW} \approx 7.5 \times 10^{-3}$  and  $\Delta_{BG} \approx 4.89 \times 10^{-2}$ . For the onsite Hubbard term, we impose the condition  $\delta_{BW} \lesssim \langle U \rangle < \Delta_{BG}$ , where  $\langle U \rangle = U \sum_{j,\lambda} \langle n_{j\uparrow\lambda} n_{j\downarrow\lambda} \rangle$  is measured in the non-interacting limit: We choose  $U = 0.4$  which gives  $\langle U \rangle / \Delta_{BG} \approx 0.18$  and  $\langle U \rangle / \delta_{BW} \approx 1.17$ . As shown in Figure 5.2(a), as a result of interaction a commensurate charge density wave emerges with the period of  $J$ .

Away from the boundary there exist strong oscillations around the average electron density, which is induced by the open boundary. Further analysis at different fillings with the same interactions in Figure 5.1 shows that it is a commensurate charge density wave, because the oscillation period is independent of the Fermi momentum, which is determined by the electron density. Meanwhile the local spin value  $\langle S_i^z \rangle$  remains zero with an error bar in the order of the truncation error for any finite  $U$ .

We calculate the charge gap defined as  $\Delta_c = \lim_{L \rightarrow \infty} [E_0(N_e = N + 2) + E_0(N_e = N - 2) - 2E_0(N_e = N)]$ , where  $E_0(N_e)$  refers to the ground state energy of a given electron number. We find  $\Delta_c = 0.0214$ , obtained after accounting for the finite-size scaling as shown in Figure 5.3. The calculations of the charge gap only depend on the ground state energy thus are very reliable. The charge gap remains finite after the scaling for  $U > 0.2$ , which indicates a gapped phase.

The extrapolated charge gap increases monotonically as  $U$  increases, and saturates at  $\Delta_c = 0.0474$  when  $U > 1$ , as shown in Figure 5.2(b). Also, it is seen that  $\Delta_c$  goes to zero at  $U \approx 0.1$ , signaling a metal-insulator transition. The spin gap is defined similarly as

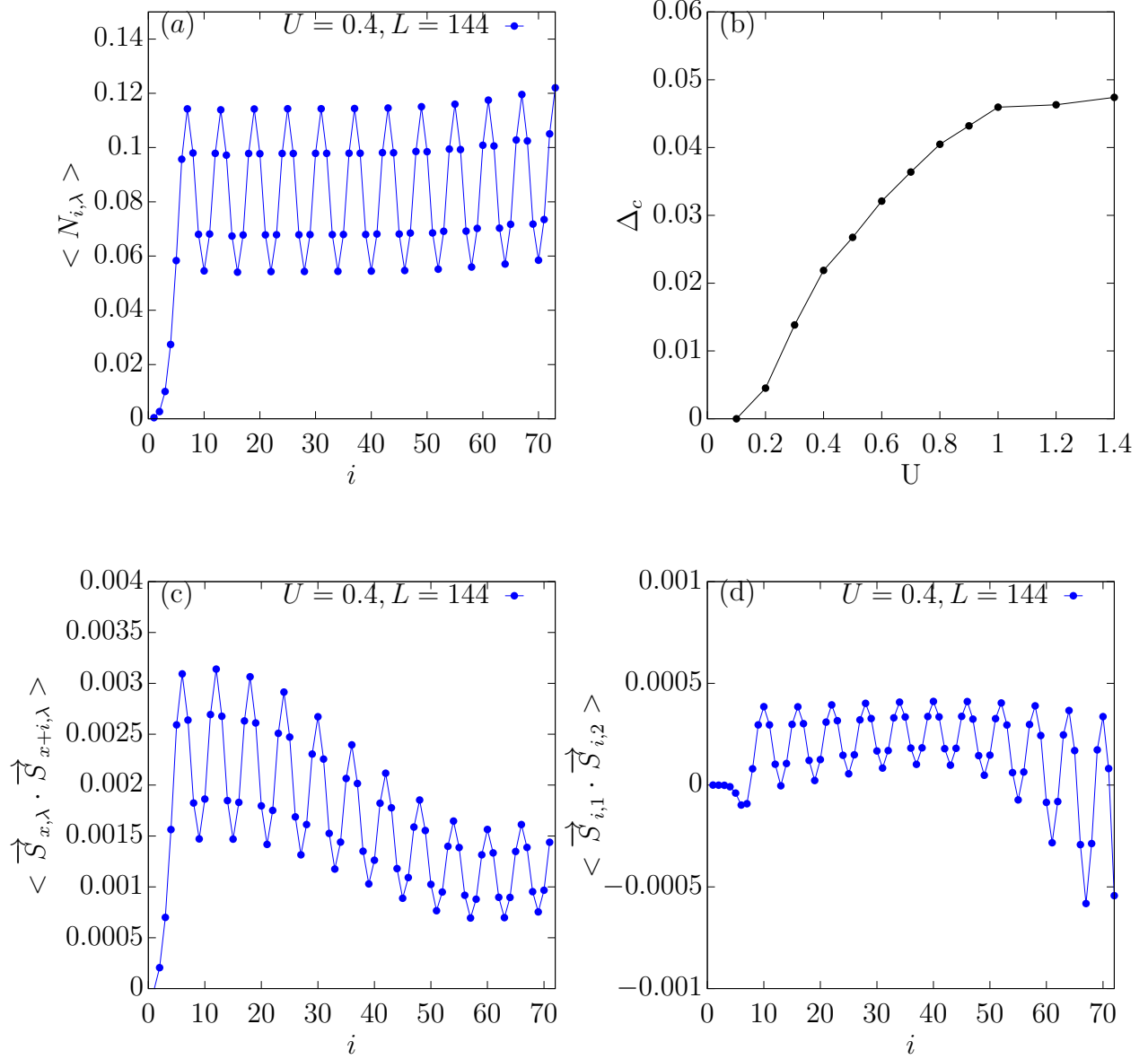


Figure 5.2: (a) refers to the electron density in real space. The electron density has a robust oscillation pattern away from the boundary with the amplitude  $\approx 0.03$ . Only half of the lattice is shown. (b) refers to the charge gap for various  $U$  after the finite-size scaling. The charge gap becomes finite for  $U > 0.2$ . (c) refers to the intra-chain spin correlations. The correlations are the same for either chain. Here  $x = \frac{L}{4}$  is chosen to be away from the boundary to minimize the finite size effect. (d) refers to the inter-chain spin correlations with only half of the lattice shown. All of the results above are obtained at  $n = \frac{1}{2J}$ .

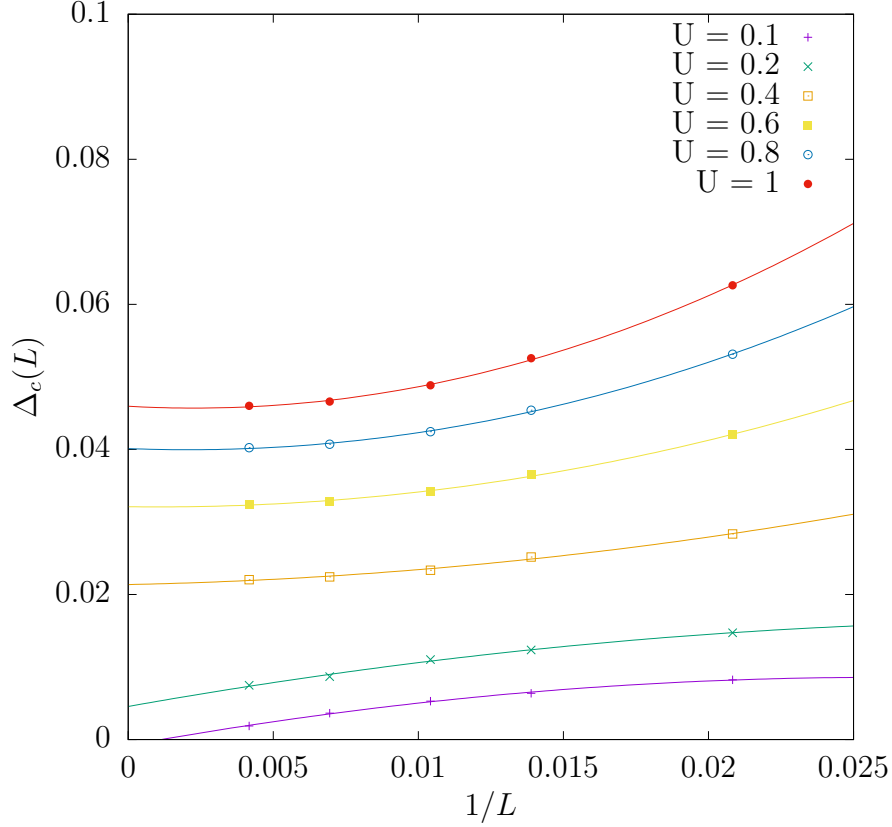


Figure 5.3: The finite-size scaling of the charge gap for various  $U$  in the quasi-flat band regime. We have used a least-square fit to the third order of polynomials in  $1/L$ . Similar fittings are used in the extrapolation of the charge gap for various  $\gamma_0$ .

$\Delta_s = E_0(S_z^{tot} = 1) - E_0(S_z^{tot} = 0)$  except for the missing  $E_0(S_z^{tot} = -1)$  term because of the spin  $U(1)$  symmetry. We find that  $\Delta_s = 0$  (less than  $10^{-6}$ ). The non-zero charge gap and a zero spin gap at finite  $U$  is consistent with the Mott state at half-filling.

We next investigate the spin-spin correlations in this Mott state. The spin correlations within each leg are defined as  $\langle \vec{S}_{i\lambda} \cdot \vec{S}_{j\lambda} \rangle$  where  $\vec{S}_{i\lambda}$  is the total spin of the electrons on site  $i$  of the  $\lambda$ th chain. As shown in Figure 5.2(c), the spin-spin correlations oscillate with the same period as the electron density, and are independent of the Fermi momentum as well. However, the spin-spin correlation values are all positive between any two site, indicating a

ferromagnetic ordering. A similar behavior is observed for the spin-spin correlation between the two legs, although it is found to be weaker than the intra-leg correlation. This is shown in Figure 5.2(d). This suggests that in the quasi-flat regime, the system is an unusual ferromagnetic Mott insulator.

When the interaction is much smaller than the bandwidth, the system could be considered as an effective one dimensional Hubbard chain and the state may become antiferromagnetic. In order to study the phase transition we change the bandwidth while keeping the interaction strength the same. The bandwidth is controlled by the parameters  $\gamma_0$  and  $g$  in our model. To change it, we keep  $g$  fixed to the value used before ( $g = 0.1$ ) and change  $\gamma_0$ . Thus,  $\gamma_0$  is a proxy for the bandwidth which can be read off from Figure 5.4(c). As shown in Figure 5.4(a), as  $\gamma_0$  is decreased (bandwidth is increased), the ferromagnetic ordering becomes antiferromagnetic. In the inset, we show the expected spin-spin correlation in the limit when the two legs are completely uncoupled. It is clear, once the transition has occurred, the spin-spin correlation quickly assumes the form expected for a single chain. Thus, the emergence of the ferromagnetic phase only appears on a small bandwidth. A better representation of the ferromagnetic-antiferromagnetic transition can be achieved by the structure factor  $S(k) = \frac{1}{N} \sum_{i,j} \langle \vec{S}_i \cdot \vec{S}_j \rangle e^{ik(x_i - x_j)}$ . We plot in Figure 5.4(b)  $S(k)$  vs.  $k$  for different values of  $\gamma_0$ . Presence of ferromagnetic ordering at larger values of  $\gamma_0$  (smaller bandwidth) is marked by a peak at  $k = 2\pi/6$  representing the dominant frequency of oscillations in the spin correlation. At smaller values of  $\gamma_0$  (larger bandwidth), another peak emerges at  $k = 2\pi/12$  signalling the presence of antiferromagnetic ordering. Around  $\gamma_0 \approx 0.43$ , where the transition happens, we find both peaks present. The ferromagnetic to antiferromagnetic transition is also observed in spin-spin correlation between the two legs as shown in Figure 5.2(c). In the charge sector, we find charge density waves with the same periodicity as in the quasi-flat band regime. The charge gap decreases with decrease in  $\gamma_0$

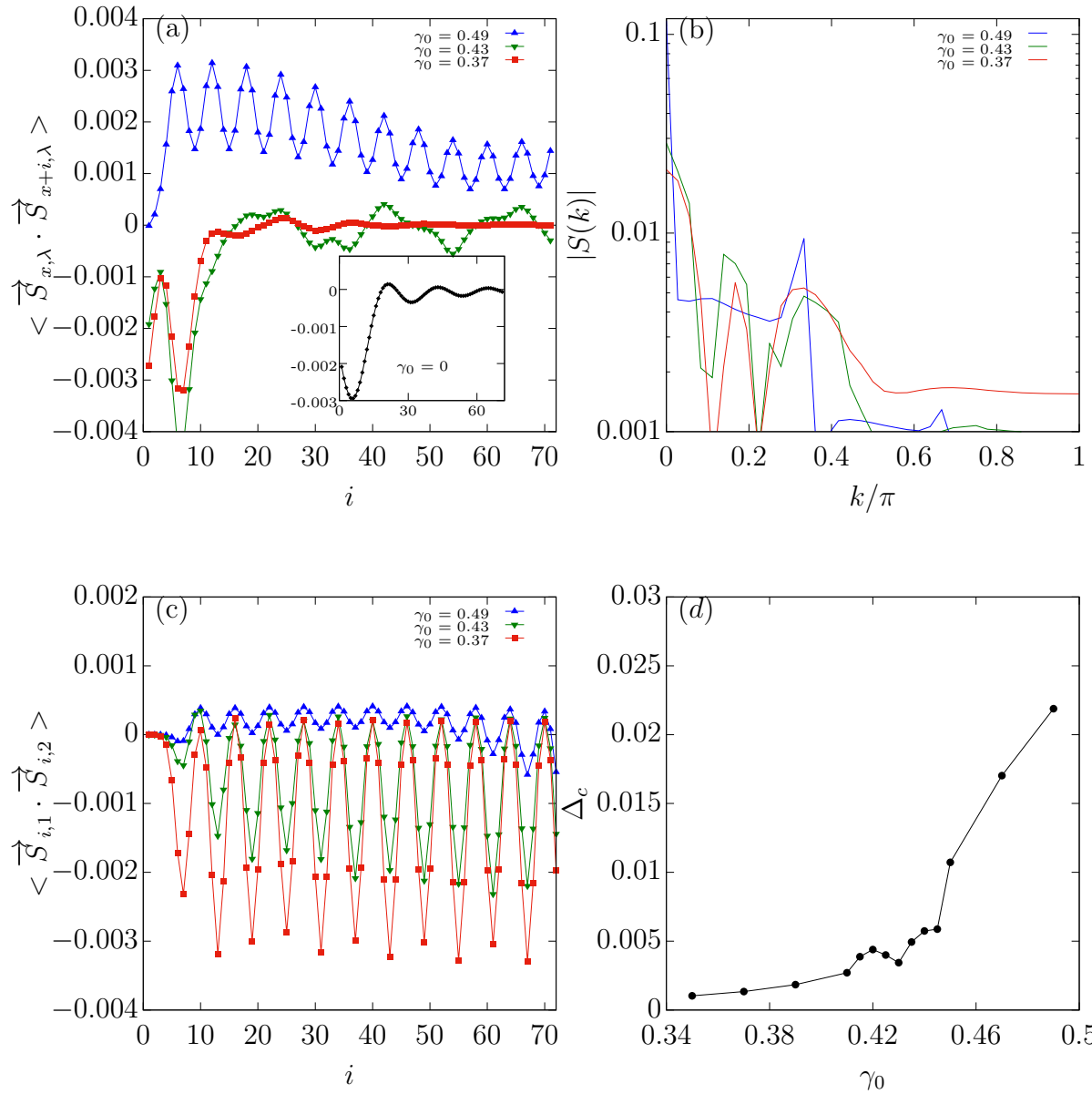


Figure 5.4: (a) refers to the intra-chain spin correlations for various  $\gamma_0$  where  $x = \frac{L}{4}$  is chosen to be away from the boundary. The correlations are the same for either chain. The inset shows the correlations in the uncoupled limit. (b) refers to the spin structure for various  $\gamma_0$  (c) refers to the inter-chain spin correlations for various  $\gamma_0$ , obtained with the finite length of  $L = 144$ . Only half of the lattice is shown. (d) refers to the charge gap for various  $\gamma_0$  after the finite-size scaling. All of the results above are obtained at  $U = 0.4$  and  $n = \frac{1}{2J}$ .

(increase in bandwidth), as shown in Figure 5.4(d), except near  $\gamma_0 = 0.43$  where it shows certain features. This is the same value at which the ferromagnetic to antiferromagnetic transition appears in the spin sector.

Besides the onsite Coulomb interactions in Equation 5.5, we have tested other interactions such as the next-nearest-neighbor Coulomb interactions, which is defined as

$$V \sum_{j,\sigma,\sigma',\lambda} n_{j\sigma\lambda} n_{j+1\sigma'\lambda} \quad (5.6)$$

As shown in Figure 5.5 the spin correlations become ferromagnetic for finite  $V$ , which is similar to the one with only onsite Coulomb interactions, suggesting that the ferromagnetic Mott state is robust against various types of Coulomb interactions.

In summary, we have shown that a two-leg ladder with a flux and a periodic coupling term between the legs produces a low energy quasi-flat band similar to that in magic angle TBG. In the presence of interaction, the ground state is a ferromagnetic Mott insulator. As the band becomes more dispersive, the ground state changes into an antiferromagnetic Mott insulator. In addition to providing clues to the physics of magic angle TBG, the model could be relevant in the larger context of 1D correlations and magnetism.

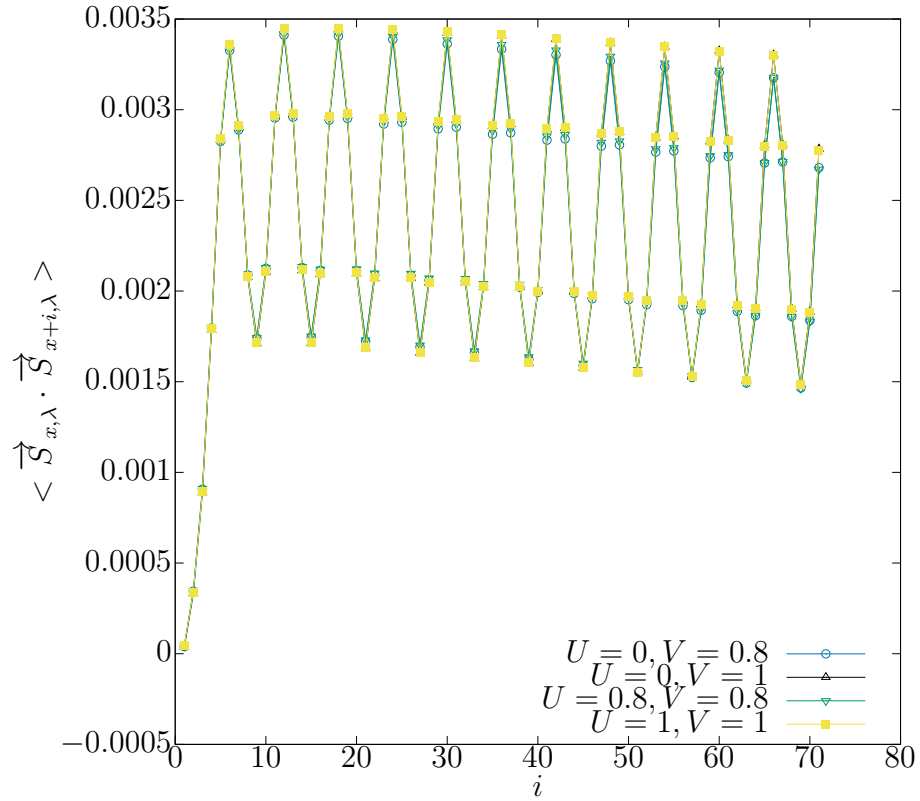


Figure 5.5: The intra-chain spin correlations with next-nearest-neighbor Coulomb interactions, obtained by the system length of  $L = 144$ . The correlation is calculate at  $x = \frac{L}{4}$  in order to minimize the effect of the open boundary, and the correlation is the same for either chain.

# Chapter 6

## The Kondo impurity in a superconductor

### 6.1 Kondo screening in a superconductor

The Kondo screening refers to a magnetic impurity surrounded by electrons with opposite spins. In normal metal where there are enough free electrons, the magnetic impurity behaves as a non-magnetic impurity after the screening. However, in a superconductor, especially in s-wave superconductor, there are only cooper pairs instead of free electrons at zero temperature. For s-wave superconductor the cooper pairs has singlet pairing, therefore can not contribute to the screening of the magnetic impurity [162].

Alternatively, if the interactions between the magnetic impurity and the electrons are strongly enough, one cooper pair will break and the magnetic impurity will form a spin singlet state with one of the electrons. This quasi-particle state is known as the Yu-Shiba-Rusinov (YSR) states [163, 164, 165, 166, 167]. The quasi-particle gap of the YSR states lies in the superconducting gap, with two peaks located symmetrically about the center of the superconducting gap due to particle-hole symmetry.

We consider the single Kondo impurity [168] of spin- $\frac{1}{2}$  in an  $s$ -wave superconductor where the Hamiltonian has two terms, the  $H_{BCS}$  is the BCS Hamiltonian of the  $s$ -wave superconductor and  $H_{imp}$  is the interactions between the electrons and the impurity spin.

$$\begin{aligned}
H &= H_{BCS} + H_{imp} \\
H_{BCS} &= \sum_{k\sigma} \epsilon_k c_{k\sigma}^\dagger c_{k\sigma} - \Delta \sum_k (c_{k\uparrow}^\dagger c_{-k\downarrow}^\dagger + H.c.) \\
H_{imp} &= J \vec{S} \cdot \left( \frac{1}{2N_s} \sum_{kk'\sigma\sigma'} c_{k\sigma}^\dagger \vec{\tau}_{\sigma\sigma'} c_{k'\sigma'} \right)
\end{aligned} \tag{6.1}$$

$c_{k\sigma}$  is the electron annihilation operator at momentum  $k$  and spin  $\sigma$ ,  $\epsilon_k$  is the single particle energy band dispersion,  $\Delta$  is the BCS gap parameter,  $J$  is the antiferromagnetic exchange interaction between the Kondo impurity and the conduction electrons,  $S$  is the impurity spin with  $S = \frac{1}{2}$ ,  $N_s$  is the number of lattice sites, and  $\tau$  is the Pauli matrix.

The Hamiltonian defined in the continuous three dimensional space is hard to diagonalize numerically. Thus, we need to apply the spherical wave representation, then discretize the states in a logarithmic way with respect to the momentum in radial direction [169, 170]. The resulting Hamiltonian will be in one dimension, and only finite numbers of discrete states are needed as we neglect the high energy states. This transformation was originally done by Wilson for the Numerical Renormalization Group calculations of the Kondo problem [37]. The resulting Hamiltonian becomes

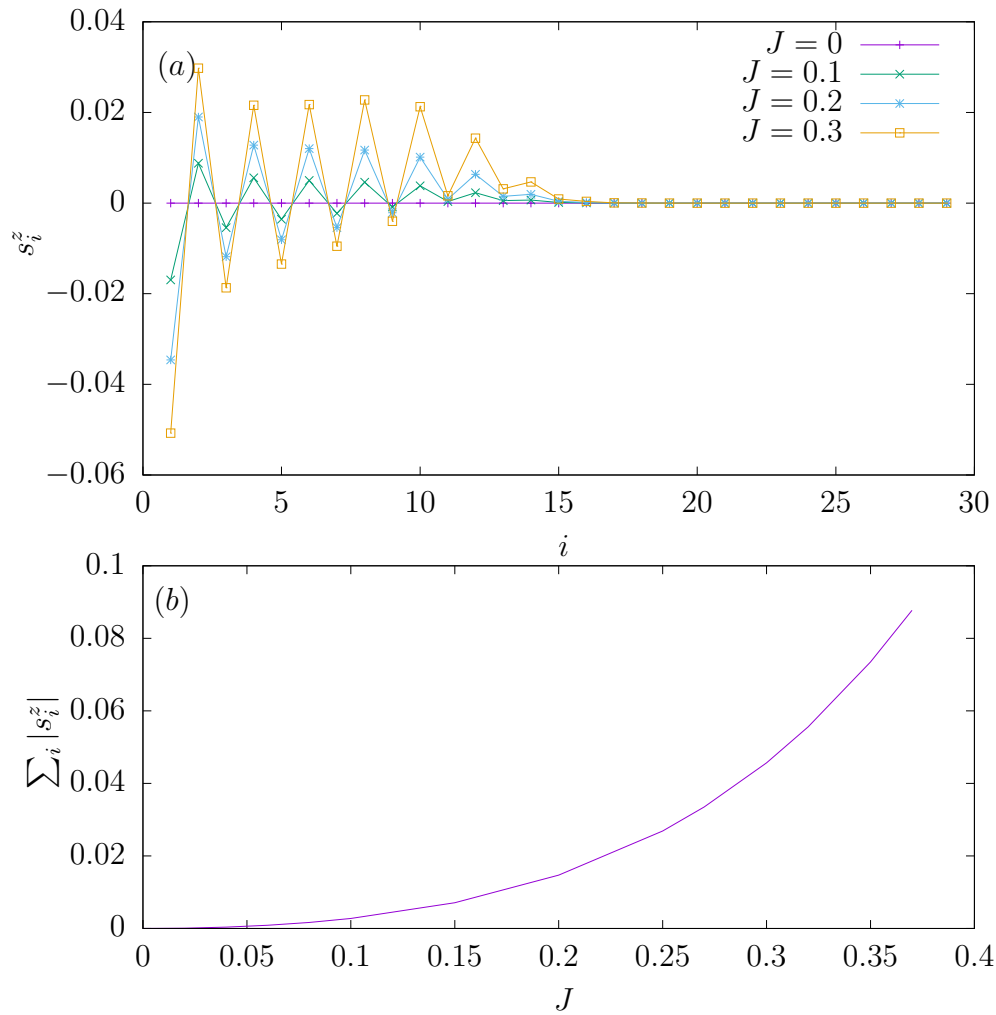


Figure 6.1: (a) refers to the local spin value for various  $J$ , (b) refers to the total electron spins versus  $J$ .

$$\begin{aligned}
H &= H_k + H_\Delta + H_{imp} \\
H_k &= \frac{1 + \Lambda^{-1}}{2} \sum_{\sigma} \sum_{n=0}^{\infty} \Lambda^{-n/2} \epsilon_n (f_{n\sigma}^\dagger f_{n+1\sigma} + H.c.) \\
H_\Delta &= -\Delta \sum_{n=0}^{\infty} (f_{n\uparrow}^\dagger f_{n\downarrow}^\dagger + H.c.) \\
H_{imp} &= \frac{J}{2} \vec{S} \cdot \sum_{\sigma\sigma'} f_{0\sigma}^\dagger \vec{\tau}_{\sigma\sigma'} f_{0\sigma'}
\end{aligned} \tag{6.2}$$

where  $H_k$  is the hopping term,  $H_\Delta$  is the pairing potential, and  $H_{imp}$  is the interactions that comes from the  $H_{imp}$  in Equation 6.1. The  $f_n^\dagger$  is the electron creation operator at level  $n$ . Here  $n$  is not the lattice site number but the radial distance after the logarithmic discretization, so we choose a different symbol for the electron operator. The density of states of conduction electrons is renormalized by  $D = 1$ , and  $\Lambda$  is the logarithmic discretization parameter. The  $\epsilon_n$  is defined as

$$\epsilon_n = (1 - \Lambda^{-(n+1)}) (1 - \Lambda^{-(2n+1)})^{-1/2} (1 - \Lambda^{-(2n+3)})^{-1/2}$$

The Hamiltonian acts on a half infinite chain with the impurity interaction term  $H_{imp}$  acting on the first site. In addition, the parameters in the hopping term  $H_k$  has an exponential decay, making it possible to approximate the results using a finite length. For the  $\Lambda = 2$  that we choose,  $N_s = 68$  sites is enough in the DMRG calculations. The total electron number is not conserved because of the superconducting term, but we still have the electron parity conservation as well as the total  $S_z$  conservation. During the final sweeping in the DMRG process, 300 states are kept in order to achieve the truncation error less than  $10^{-11}$ .

In the limit of  $J \rightarrow 0$  the Kondo impurity becomes a free spin, and there should be no screening from the electrons at all. As  $J$  increases, the screening will start to enhance. As

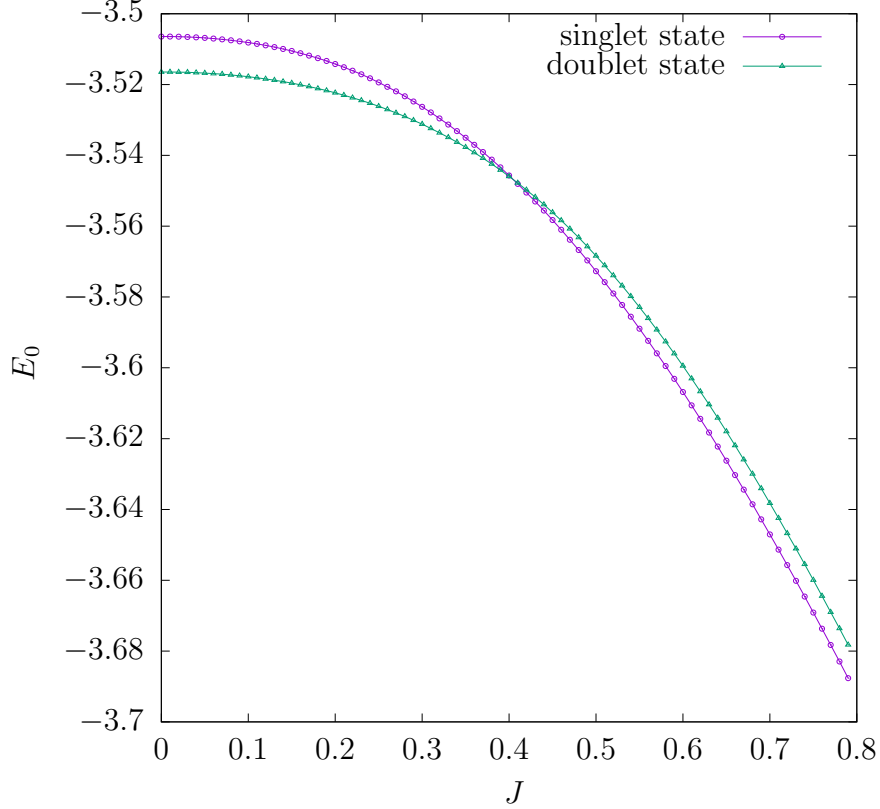


Figure 6.2: The ground state energy of the singlet state and doublet state obtained by DMRG, which is represented by the purple and green line, respectively.

shown in Figure 6.1(a), the electron spins becomes finite with finite  $J$ . The site  $i$  here does not represent the physical distance away from the impurity, it is the radial distance after the logarithmic correction. In Figure 6.1(b) we find that the total electron spins increase monotonically as  $J$ , indicating that the screening is enhanced.

## 6.2 Kondo singlet state and doublet state

In the strong coupling limit as opposed to the free spin limit, at zero temperature the impurity spin will capture one electron and form the spin singlet state, and we refer it as the Kondo singlet ground state. The state with the impurity spin in the spin doublet state

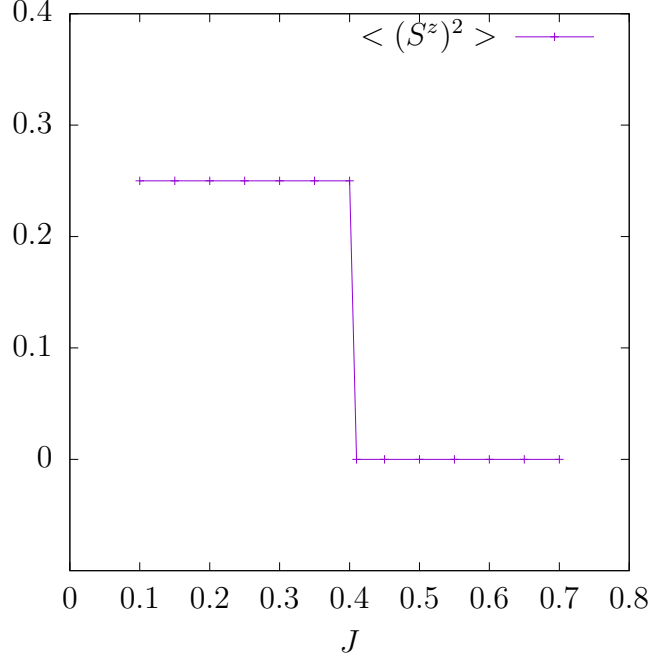


Figure 6.3: The impurity magnetic moment square for various  $J$ .

is the Kondo double state. The Kondo singlet state has odd numbers of electrons because all the other electrons have formed Cooper pairs, while the Kondo doublet state has even number of electrons. Using the electron parity conservation, we can calculate the ground state energy evolution of the two sub-space by varying the Kondo coupling  $J$ . As shown in Figure 6.2, in the weak coupling case as  $J < J_c \approx 0.405$ , the impurity spin could not pair with any conduction electron, and thus the ground state has doublet degeneracy. For  $J > J_c$ , it appears that the impurity spin can capture an electron from a Cooper pair and form a singlet ground state.

The transition from Kondo doublet ground state to singlet ground state can be further confirmed by the impurity spin square. If there is no conduction electrons,  $\langle (S_{imp}^z)^2 \rangle$  is just 0.25. Similarly, it is 0 if there exists no impurity. Thus, this quantity describes the impurity contribution to the square of the total magnetic moment. As shown in Figure 6.3, the quantity drops from 0.25 to 0 at the critical coupling strength of  $J_c \approx 0.405$ .

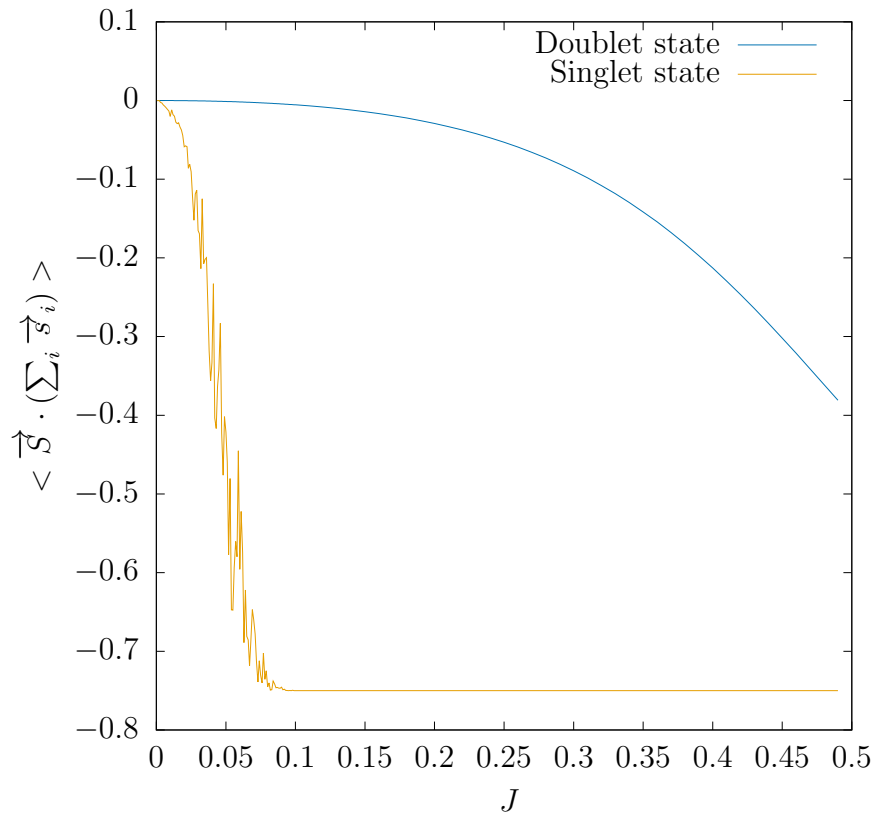


Figure 6.4: The correlations between the impurity spin and the electron spins in the singlet ground state (yellow line) and the doublet ground state (blue line) for various  $J$ .

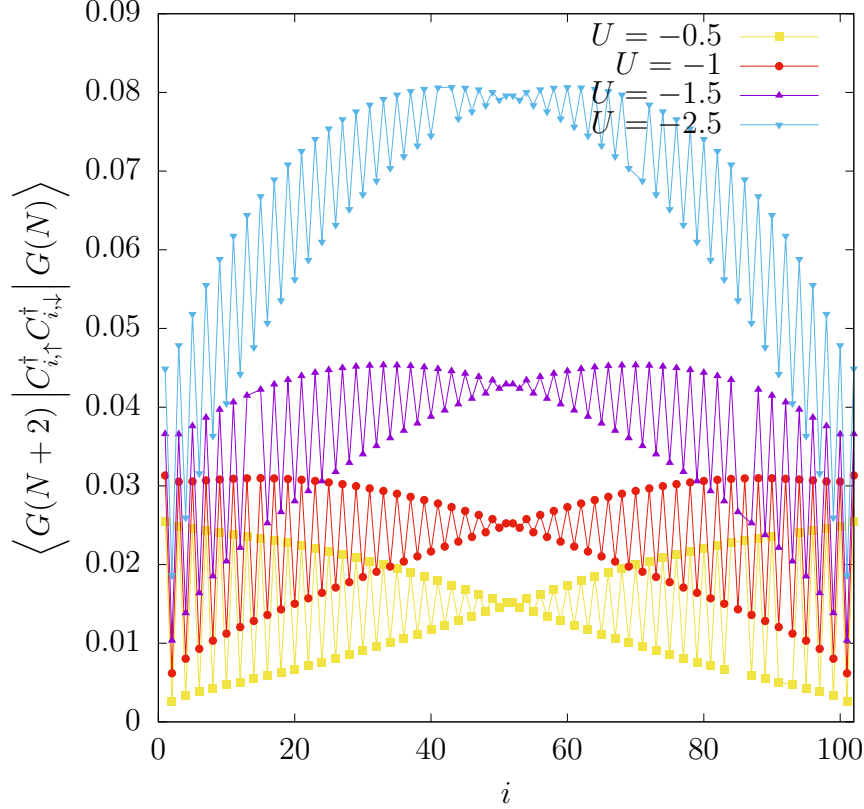


Figure 6.5: The superconducting order parameter without magnetic impurity spin for various onsite attractive interactions.

However, even if the impurity spin can not capture an electron the antiferromagnetic coupling may result in partial screening. This can be seen from the spin correlations between the impurity spin and the electron spins in Figure 6.4. For the Kondo singlet state because there is one free electron that can not be paired, the correlation quickly drop to  $-0.75$ , indicating the formation of a spin singlet state. In the Kondo doublet state the correlation has a very slow decrease as  $J$  increases, which suggests a partial screening of the impurity spin near the  $J_c$ .

Other studies of the Kondo impurity in the s-wave superconductor has found no partial screening [162]. One of the reason for this is that the pairing potential may not be uniform in real materials. To illustrate this idea, we consider the Hamiltonian with attractive onsite

Coulomb interactions in a one dimensional chain. The Hamiltonian is

$$H = -t \sum_{i\sigma} c_{i\sigma}^\dagger c_{i+1\sigma} + h.c. + U \sum_i n_{i\downarrow} n_{i\uparrow} \quad (6.3)$$

The hopping parameter  $t$  is set to 1, and  $U$  is negative. The Hamiltonian has total electron number conservation which is different than Equation 6.2, thus the ground state of this Hamiltonian for a finite system will always be in a certain electron number sector, which leads to a zero superconducting order in the ground state. Here we calculate two ground states of the same parameters with total electron number differed by two, and then calculate the superconducting order parameter by taking the overlap of the two after applying the s-wave superconducting operator. One of the example is given here in Figure 6.5 with  $\Delta \sim \langle G(N+2) | C_{i,\uparrow}^\dagger C_{i,\downarrow}^\dagger | G(N) \rangle$ . The superconducting order has staggered pattern in real space with inversion symmetry, and it increases as  $U$  decreases.

We find similar behavior of the superconducting order in the presence of a magnetic impurity. The magnetic impurity is placed in the middle of the lattice with  $H_{imp} = J \vec{S} \cdot \sum_{\sigma\sigma'} c_{N/2,\sigma}^\dagger \vec{\tau}_{\sigma\sigma'} f_{N/2,\sigma'}$  included in the Hamiltonian. As shown in Figure 6.6, the superconducting order has the similar staggered pattern as Figure 6.5, and it also increases as  $U$  decreases. There are some negative values of the superconducting order at certain sites due to the truncation error, but we show that in general the pairing potential may not be uniform with realistic electron-electron interactions involved. Recently the Hubbard model [171] and the t-J model in two dimensions have been found to host a superconducting ground state in the doped regime, and the Kondo screening in a superconductor can be studied with those models as future directions.

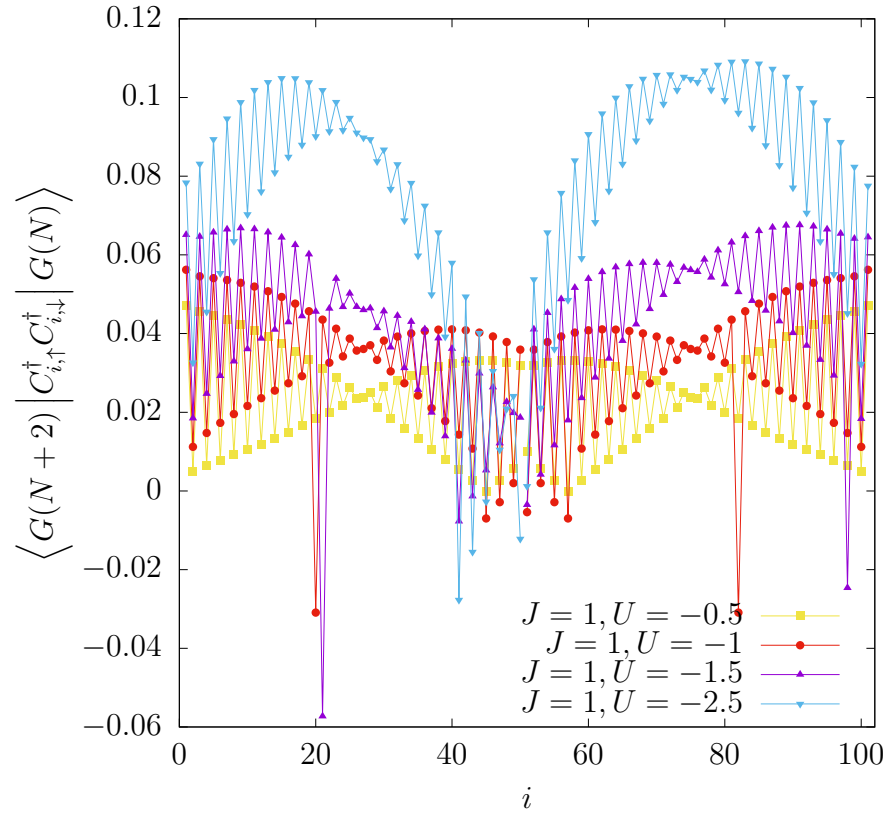


Figure 6.6: The superconducting order parameter with a magnetic impurity spin in the middle ( $i = 51$ ) for various onsite attractive interactions.

# Chapter 7

## Summary

The DMRG method has become a standard unbiased numerical method to study strongly correlated systems in low dimensions. We have studied both electron and spin systems, either in low dimensional lattices or by reducing the models in higher dimensions into the low dimensional effective models. These models are related to the fundamental quantum models that are of general interests to the condensed matter field, and can provide possible explanations to the experimental results. The DMRG has been developed from the iterative ground state solver for one dimensional lattice to a powerful numerical technique that can cope with finite temperatures states, entanglement and topological properties, non-equilibrium properties, and even real two dimensional systems with infinite lengths in both directions. With increasing number of researchers engaging in the development of algorithms based on DMRG, we believe it will become more useful in the studies of unresolved physical problems.

The analytical methods also plays an important role in understanding the underlining physics in the strongly correlated systems. Although the many-body Hamiltonian usually can not be solved exactly, the classification of different quantum states provides additional methods to numerically determine the phase diagram. As two examples studied here, the Kondo lattice model in one dimension is studied based on the Tomonaga-Luttinger liquid

theory that predicts power-law decay correlation functions. The chiral spin liquid phase in the honeycomb XY model is identified with the spectrum of the chiral edge state, which is based on conformal field theory. With the help of these analytical methods, we can rely less on the single particle picture of the model.

The main results for the studies in various models are summarized in the order of the paper. In chapter 3, we study the ground state of the standard 1D Kondo lattice model and identify two insulating phases in the doped region at weak coupling, the charge density wave (CDW) and dimer/bond order wave phase. The CDW phase without bare repulsive interaction between electrons serves as an important example of strong effective Coulomb repulsion induced by the magnetic impurities, and the dimer/bond order wave phase shows a simultaneous phase transition due to the interaction between the electrons and the localized spins. It is the first time that a charge order is found in the standard 1D Kondo lattice model.

The CDW phase of the Kondo lattice model has been found in two dimensions and infinite dimensions, which is stabilized by the Kondo effect between electrons and localized spins. However, it is qualitatively different from the CDW here in one dimension which is driven by the effective repulsive interactions between electrons. There is also coexistence of magnetic orders in the CDW for two and infinite dimensions but not one dimension. Here we discover a new type of CDW phase in 1D Kondo lattice model, which means that though it does not include bare repulsive interactions, the CDW is still driven by the effective repulsive interactions. The dimer/bond order wave phase provides a possible mechanism of the simultaneous Peierls and spin-Peierls transition found in the 1D organic compounds (e.g. D2X where D is fluoranthene or perylene derivatives, and X is AsF<sub>6</sub> or PF<sub>6</sub>), which is considered as an experimental realization of the 1D Kondo lattice model.

These charge orders also exist in other fundamental 1D models like the Hubbard model

and t-J model. The comparison of the charge orders in different models and the potential novel phase of the mixed models (e.g. Kondo lattice model with Hubbard interaction) are interesting starting points for future study. The emergence of these charge orders enriches the phase diagram and may have implication for the effective repulsive interaction caused by the magnetic impurities in higher dimensions.

In recent years, the chiral spin liquids (CSL) have been theoretically investigated and are actively searched for in experiments. For the extended spin- $\frac{1}{2}$  XY model on honeycomb lattice, theoretical studies have suggested the possible existence of CSL in the highly frustrated regime generated by the staggered Chern-Simons flux with nontrivial topology, and since then there have been extensive studies trying to identify the CSL numerically. However, so far there are no direct numerical evidence supporting this claim.

In chapter 4, we provide strong numerical evidence of the long-sought CSL in the extended spin- $\frac{1}{2}$  XY model and clarify the conditions for such a phase to emerge. The global phase diagram of the extended XY model with first-neighbor ( $J_1$ ), second-neighbor ( $J_2$ ) interactions, and a three-spin chiral term ( $J_\chi$ ) is identified using large scale DMRG method. We use the robust degeneracy pattern in the chiral entanglement spectrum as the fingerprint for the emergence of the CSL. This method has been proven to be an unbiased and accurate way to identify the CSL. The CSL emerges with finite chiral interactions and a finite spin gap, where the minimum  $J_\chi$  required appears in the highly frustrated regime of  $J_2/J_1$ . Our results demonstrate the importance of the interplay between magnetic frustration and chiral interactions, which leads to a rich phase diagram. Without the chiral interactions, the magnetic frustration in the xy-plane alone would only result in an antiferromagnetic order along the z-direction.

Experimentally, of all the honeycomb materials that are found to show a quantum-spin-liquid-like behavior, the Co-based compounds are mostly studied in the context of spin- $\frac{1}{2}$

XY model such as  $\text{BaCo}_2(\text{PO}_4)_2$  and  $\text{BaCo}_2(\text{AsO}_4)_2$ . Our numerical results provide a simple mechanism for the emergence of CSL via competing magnetic frustrations and chiral interactions in these materials. The chiral interactions may be generated by a  $\phi$  flux in every elementary honeycomb. On the other hand, the results of CSL may be tested in cold atoms experiments as the spin XY model could be mapped by the bosonic Kane-Mele model in the Mott regime.

In chapter 5, we provide some insight into the physics of the magic angle twisted bilayer graphene by using an unrelated model which is a two leg ladder with magnetic flux. Using DMRG, we show that the latter can help us understand the phenomenon in the former. Without the complex lattice structure and the Dirac dispersion, the two leg ladder only maintains one unique property from the magic angle twisted bilayer graphene, which is the quasi-flat band. When the Coulomb repulsive interactions are included in the Hamiltonian, the state becomes a ferromagnetic Mott insulator. Numerical results show that with increasing Coulomb interactions the phase transition occurs at the critical  $U$  with the interaction larger than the band width, but smaller than the band gap. Thus, the phase transition is not a result of mixing the two lowest bands. In addition, the ferromagnetic Mott state is not a  $4k_F$  density wave which often exists in 1D Hubbard model, but a commensurate density wave that does not depend on the Fermi momentum. The ferromagnetic Mott state changes into an antiferromagnetic Mott state as the band becomes wider, which is consistent with the antiferromagnetic ground state in the one dimensional Hubbard model at half filling.

The experiments of the twisted bilayer graphene has found that near the magic angle, the state becomes a correlated insulator. Some theoretical studies have proposed that the ground state should be ferromagnetic [172, 173] because of the unusual shape of the Wannier functions, but there are other numerical results that support an antiferromagnetic ground state [174]. It is interesting to observe a ferromagnetic insulating state in the auxiliary model

that mimics the twisted bilayer graphene at the single particle level.

In chapter 6, we revisit some of the properties for the Kondo impurity in a superconductor, and relate to other numerical studies of the quasi-particle states induced by the Kondo impurity which is known as the Yu-Shiba-Rusinov state. The state is a result of breaking a Cooper pair and forming a spin singlet state with the impurity spin. Other numerical studies have used the effective spin- $\frac{1}{2}$  impurity in a s-wave superconductor which is given by the BCS Hamiltonian, and we are able to reproduce most of the results at zero temperature including the singlet state to doublet state phase transition. However, our DMRG results show that there are correlations between the impurity spin and the electron spins even in the doublet state, indicating a partial screening in the ground state, which is not found by other studies. We believe that one of the reasons may be the non-uniform superconducting order in the presence of the impurity spin and open boundary. The study of Kondo impurity in a superconductor may be conducted on a realistic model with electron-electron interactions, like the Hubbard model in two dimensions which is shown to have superconducting ground state in the doped regime recently.

# Bibliography

- [1] Philip W Anderson. More is different. *Science*, 177(4047):393–396, 1972.
- [2] Thierry Giamarchi. *Quantum physics in one dimension*, volume 121. Clarendon press, 2003.
- [3] Jean-Paul Pouget, Pascale Foury-Leylekian, and Manuel Almeida. Peierls and spin-peierls instabilities in the per2 [m (mnt) 2] series of one-dimensional organic conductors; experimental realization of a 1d kondo lattice for m= pd, ni and pt. *Magnetochemistry*, 3(1):13, 2017.
- [4] Piers Coleman. New approach to the mixed-valence problem. *Physical Review B*, 29(6):3035, 1984.
- [5] Martin C Gutzwiller. Effect of correlation on the ferromagnetism of transition metals. *Physical Review Letters*, 10(5):159, 1963.
- [6] Alexander Weiß and Holger Fehske. Exact diagonalization techniques. In *Computational many-particle physics*, pages 529–544. Springer, 2008.
- [7] Eric Jeckelmann and Holger Fehske. Exact numerical methods for electron-phonon problems. *arXiv preprint cond-mat/0510637*, 2005.

- [8] Steven R White. Density matrix formulation for quantum renormalization groups. *Physical review letters*, 69(19):2863, 1992.
- [9] Steven R White. Density-matrix algorithms for quantum renormalization groups. *Physical Review B*, 48(14):10345, 1993.
- [10] FF Assaad and HG Evertz. Computational many-particle physics. *Lecture Notes in Physics*, 739:277, 2008.
- [11] Antoine Georges, Gabriel Kotliar, Werner Krauth, and Marcelo J Rozenberg. Dynamical mean-field theory of strongly correlated fermion systems and the limit of infinite dimensions. *Reviews of Modern Physics*, 68(1):13, 1996.
- [12] John Hubbard. Calculation of partition functions. *Physical Review Letters*, 3(2):77, 1959.
- [13] AI Larkin and J Sak. Boundary conditions for renormalization-group equations in one-dimensional fermi gas. *Physical Review Letters*, 39(16):1025, 1977.
- [14] HJ Schulz. Fermi liquids and non-fermi liquids. *arXiv preprint cond-mat/9503150*, 1995.
- [15] Eric Jeckelmann. Ground-state phase diagram of a half-filled one-dimensional extended hubbard model. *Physical review letters*, 89(23):236401, 2002.
- [16] Anders W Sandvik, Leon Balents, and David K Campbell. Ground state phases of the half-filled one-dimensional extended hubbard model. *Physical review letters*, 92(23):236401, 2004.
- [17] Satoshi Ejima and Satoshi Nishimoto. Phase diagram of the one-dimensional half-filled extended hubbard model. *Physical review letters*, 99(21):216403, 2007.

- [18] FC Zhang and TM Rice. Effective hamiltonian for the superconducting cu oxides. *Physical Review B*, 37(7):3759, 1988.
- [19] Elbio Dagotto and Jose Riera. Indications of  $d \times 2-y \ 2$  superconductivity in the two dimensional t-j model. *Physical review letters*, 70(5):682, 1993.
- [20] Aaron Szasz, Johannes Motruk, Michael P Zaletel, and Joel E Moore. Observation of a chiral spin liquid phase of the hubbard model on the triangular lattice: a density matrix renormalization group study. *arXiv preprint arXiv:1808.00463*, 2018.
- [21] Yi Zhou, Kazushi Kanoda, and Tai-Kai Ng. Quantum spin liquid states. *Reviews of Modern Physics*, 89(2):025003, 2017.
- [22] Steven R White and Ian Affleck. Dimerization and incommensurate spiral spin correlations in the zigzag spin chain: Analogies to the kondo lattice. *Physical Review B*, 54(14):9862, 1996.
- [23] Alexander Wietek and Andreas M Läuchli. Chiral spin liquid and quantum criticality in extended  $s=1 \ 2$  heisenberg models on the triangular lattice. *Physical Review B*, 95(3):035141, 2017.
- [24] Zhenyue Zhu, David A Huse, and Steven R White. Unexpected z-direction ising antiferromagnetic order in a frustrated spin-1/2  $j_1-j_2 \times y$  model on the honeycomb lattice. *Physical review letters*, 111(25):257201, 2013.
- [25] Shou-Shu Gong, Wei Zhu, DN Sheng, Olexei I Motrunich, and Matthew PA Fisher. Plaquette ordered phase and quantum phase diagram in the spin-1  $2 \ j_1-j_2$  square heisenberg model. *Physical review letters*, 113(2):027201, 2014.
- [26] F Duncan M Haldane. Continuum dynamics of the 1-d heisenberg antiferromagnet:

- Identification with the  $o(3)$  nonlinear sigma model. *Physics Letters A*, 93(9):464–468, 1983.
- [27] Leon Balents. Spin liquids in frustrated magnets. *Nature*, 464(7286):199, 2010.
- [28] R. Moessner and S. L. Sondhi. Resonating valence bond phase in the triangular lattice quantum dimer model. *Phys. Rev. Lett.*, 86:1881–1884, Feb 2001.
- [29] Sergei V Isakov, Matthew B Hastings, and Roger G Melko. Topological entanglement entropy of a bose–hubbard spin liquid. *Nature Physics*, 7(10):772, 2011.
- [30] Philip W Anderson. The resonating valence bond state in  $la_2cuo_4$  and superconductivity. *science*, 235(4793):1196–1198, 1987.
- [31] Daniel S Rokhsar and Steven A Kivelson. Superconductivity and the quantum hard-core dimer gas. *Physical review letters*, 61(20):2376, 1988.
- [32] Patrick A Lee, Naoto Nagaosa, and Xiao-Gang Wen. Doping a mott insulator: Physics of high-temperature superconductivity. *Reviews of modern physics*, 78(1):17, 2006.
- [33] Chetan Nayak, Steven H Simon, Ady Stern, Michael Freedman, and Sankar-Das Sarma. Non-abelian anyons and topological quantum computation. *Reviews of Modern Physics*, 80(3):1083, 2008.
- [34] Diptiman Sen and R Chitra. Large- $u$  limit of a hubbard model in a magnetic field: Chiral spin interactions and paramagnetism. *Physical Review B*, 51(3):1922, 1995.
- [35] Ryan V Mishmash, Matthew S Block, Ribhu K Kaul, DN Sheng, Olexei I Motrunich, and Matthew PA Fisher. Bose metals and insulators on multileg ladders with ring exchange. *Physical Review B*, 84(24):245127, 2011.

- [36] Jun Kondo. Resistance minimum in dilute magnetic alloys. *Progress of theoretical physics*, 32(1):37–49, 1964.
- [37] Kenneth G Wilson. The renormalization group: Critical phenomena and the kondo problem. *Reviews of modern physics*, 47(4):773, 1975.
- [38] Ph Nozieres and Annie Blandin. Kondo effect in real metals. *Journal de Physique*, 41(3):193–211, 1980.
- [39] Melvin A Ruderman and Charles Kittel. Indirect exchange coupling of nuclear magnetic moments by conduction electrons. *Physical Review*, 96(1):99, 1954.
- [40] Tadao Kasuya. A theory of metallic ferro-and antiferromagnetism on zener’s model. *Progress of theoretical physics*, 16(1):45–57, 1956.
- [41] Kei Yosida. Magnetic properties of cu-mn alloys. *Physical Review*, 106(5):893, 1957.
- [42] Ernst Bauer, Gerfried Hilscher, Herwig Michor, Ch Paul, EW Scheidt, A Griбанov, Yu Seropegin, H Noël, M Sigrist, and Peter Rogl. Heavy fermion superconductivity and magnetic order in noncentrosymmetric c e p t 3 s i. *Physical Review Letters*, 92(2):027003, 2004.
- [43] Hsin-Hua Lai, Sarah E Grefe, Silke Paschen, and Qimiao Si. Weyl–kondo semimetal in heavy-fermion systems. *Proceedings of the National Academy of Sciences*, 115(1):93–97, 2018.
- [44] Maxim Dzero, Kai Sun, Victor Galitski, and Piers Coleman. Topological kondo insulators. *Physical review letters*, 104(10):106408, 2010.
- [45] Philip Warren Anderson. Localized magnetic states in metals. *Physical Review*, 124(1):41, 1961.

- [46] Xiaoqun Wang and Tao Xiang. Transfer-matrix density-matrix renormalization-group theory for thermodynamics of one-dimensional quantum systems. *Physical Review B*, 56(9):5061, 1997.
- [47] Masuo Suzuki. Quantum monte carlo methods recent developments. *Physica A: Statistical Mechanics and its Applications*, 194(1-4):432–449, 1993.
- [48] Ulrich Schollwöck. The density-matrix renormalization group in the age of matrix product states. *Annals of Physics*, 326(1):96–192, 2011.
- [49] Frank Verstraete, Juan J Garcia-Ripoll, and Juan Ignacio Cirac. Matrix product density operators: simulation of finite-temperature and dissipative systems. *Physical review letters*, 93(20):207204, 2004.
- [50] Steven R White. Minimally entangled typical quantum states at finite temperature. *Physical review letters*, 102(19):190601, 2009.
- [51] EM Stoudenmire and Steven R White. Minimally entangled typical thermal state algorithms. *New Journal of Physics*, 12(5):055026, 2010.
- [52] Michael Zwolak and Guifré Vidal. Mixed-state dynamics in one-dimensional quantum lattice systems: a time-dependent superoperator renormalization algorithm. *Physical review letters*, 93(20):207205, 2004.
- [53] Adrian E Feiguin and Steven R White. Finite-temperature density matrix renormalization using an enlarged hilbert space. *Physical Review B*, 72(22):220401, 2005.
- [54] Jacob Jordan, Roman Orús, Guifre Vidal, Frank Verstraete, and J Ignacio Cirac. Classical simulation of infinite-size quantum lattice systems in two spatial dimensions. *Physical review letters*, 101(25):250602, 2008.

- [55] Lukasz Cincio and Guifré Vidal. Characterizing topological order by studying the ground states on an infinite cylinder. *Physical review letters*, 110(6):067208, 2013.
- [56] Z Hossain, M Schmidt, W Schnelle, H. S. Jeevan, C Geibel, S Ramakrishnan, J. A. Mydosh, and Y Grin. Coexistence of magnetic order and charge density wave in a kondo lattice: Yb<sub>5</sub>Ir<sub>4</sub>Si<sub>10</sub>. *Physical Review B*, 71(6):060406, 2005.
- [57] Akira Ochiai, Takashi Suzuki, and Tadao Kasuya. Heavy fermion behavior in extremely low carrier concentration system Yb<sub>4</sub>As<sub>3</sub>. *Journal of the Physical Society of Japan*, 59(11):4129–4141, 1990.
- [58] Le Wang, Zhaoming Fu, Jianping Sun, Min Liu, Wei Yi, Changjiang Yi, Yongkang Luo, Yaomin Dai, Guangtong Liu, Yoshitaka Matsushita, et al. Heavy fermion behavior in the quasi-one-dimensional kondo lattice CeCo<sub>2</sub>Si<sub>8</sub>. *npj Quantum Materials*, 2(1):36, 2017.
- [59] G. R. Stewart. Non-fermi-liquid behavior in *d*- and *f*-electron metals. *Rev. Mod. Phys.*, 73:797–855, Oct 2001.
- [60] S Doniach. The kondo lattice and weak antiferromagnetism. *Physica B+ C*, 91:231–234, 1977.
- [61] C. Lacroix and M. Cyrot. Phase diagram of the kondo lattice. *Phys. Rev. B*, 20:1969–1976, Sep 1979.
- [62] P Fazekas and E Müller-Hartmann. Magnetic and non-magnetic ground states of the kondo lattice. *Zeitschrift für Physik B Condensed Matter*, 85(2):285–300, 1991.
- [63] Hirokazu Tsunetsugu, Manfred Sigrist, and Kazuo Ueda. Phase diagram of the one-dimensional kondo-lattice model. *Physical Review B*, 47(13):8345, 1993.

- [64] Hirokazu Tsunetsugu, Manfred Sigrist, and Kazuo Ueda. The ground-state phase diagram of the one-dimensional kondo lattice model. *Reviews of Modern Physics*, 69(3):809, 1997.
- [65] <http://itensor.org/>.
- [66] Naokazu Shibata and Kazuo Ueda. The one-dimensional kondo lattice model studied by the density matrix renormalization group method. *Journal of Physics: Condensed Matter*, 11(2):R1, 1999.
- [67] Yosuke Nagaoka. Self-consistent treatment of kondo's effect in dilute alloys. *Physical Review*, 138(4A):A1112, 1965.
- [68] Naokazu Shibata, Kazuo Ueda, Tomotoshi Nishino, and Chikara Ishii. Friedel oscillations in the one-dimensional kondo lattice model. *Physical Review B*, 54(19):13495, 1996.
- [69] Robert Peters and Norio Kawakami. Ferromagnetic state in the one-dimensional kondo lattice model. *Physical Review B*, 86(16):165107, 2012.
- [70] Yixuan Huang, DN Sheng, and Chin-Sen Ting. Charge density wave in a doped kondo chain. *Physical Review B*, 99(19):195109, 2019.
- [71] Naokazu Shibata, Alexei Tsvelik, and Kazuo Ueda. One-dimensional kondo lattice model as a tomonaga-luttinger liquid. *Physical Review B*, 56(1):330, 1997.
- [72] Ilia Khait, Patrick Azaria, Claudius Hubig, Ulrich Schollwöck, and Assa Auerbach. Doped kondo chain, a heavy luttinger liquid. *Proceedings of the National Academy of Sciences*, page 201719374, 2018.

- [73] Takahiro Misawa, Junki Yoshitake, and Yukitoshi Motome. Charge order in a two-dimensional kondo lattice model. *Physical review letters*, 110(24):246401, 2013.
- [74] Yukitoshi Motome, Kyoya Nakamikawa, Youhei Yamaji, and Masafumi Udagawa. Partial kondo screening in frustrated kondo lattice systems. *Physical review letters*, 105(3):036403, 2010.
- [75] Toshihiro Sato, Fakher F Assaad, and Tarun Grover. Quantum monte carlo simulation of frustrated kondo lattice models. *Physical review letters*, 120(10):107201, 2018.
- [76] Robert Peters, Shintaro Hoshino, Norio Kawakami, Junya Otsuki, and Yoshio Kuramoto. Charge order in kondo lattice systems. *Physical Review B*, 87(16):165133, 2013.
- [77] J. E. Hirsch. Strong-coupling expansion for a kondo-lattice model. *Physical Review B*, 30(9):5383, 1984.
- [78] I. P. McCulloch, A Juozapavicius, Anders Rosengren, and Miklos Gulacsi. Localized spin ordering in kondo lattice models. *Physical Review B*, 65(5):052410, 2002.
- [79] N. D. Mermin and H. Wagner. Absence of ferromagnetism or antiferromagnetism in one- or two-dimensional isotropic heisenberg models. *Phys. Rev. Lett.*, 17:1133–1136, Nov 1966.
- [80] M Vekić and S. R. White. Smooth boundary conditions for quantum lattice systems. *Physical review letters*, 71(26):4283, 1993.
- [81] S. R. White, Ian Affleck, and Douglas J Scalapino. Friedel oscillations and charge density waves in chains and ladders. *Physical Review B*, 65(16):165122, 2002.

- [82] Thierry Giamarchi. *Quantum physics in one dimension*, volume 121. Oxford university press, 2004.
- [83] J. C. Xavier, R. G. Pereira, E Miranda, and I Affleck. Dimerization induced by the rkky interaction. *Physical review letters*, 90(24):247204, 2003.
- [84] Matthias Peschke, Roman Rausch, and Michael Potthoff. Frustrated quantum magnetism in the kondo lattice on the zigzag ladder. *Physical Review B*, 97(11):115124, 2018.
- [85] Alexei M Tsvelik and OM Yevtushenko. Physics of arbitrarily doped kondo lattices: From a commensurate insulator to a heavy luttinger liquid and a protected helical metal. *Physical Review B*, 100(16):165110, 2019.
- [86] J. C. Xavier and E. Miranda. One-dimensional kondo lattice model at quarter filling. *Phys. Rev. B*, 78:144406, Oct 2008.
- [87] Chisa Hotta and Naokazu Shibata. Absence of dimer order and the tomonaga–luttinger liquid properties of the quarter-filled one-dimensional kondo-lattice model. *Physica B: Condensed Matter*, 378:1039–1040, 2006.
- [88] Naokazu Shibata and Chisa Hotta. Boundary effects in the density-matrix renormalization group calculation. *Physical Review B*, 84(11):115116, 2011.
- [89] EL Green, JS Brooks, PL Kuhns, AP Reyes, LL Lumata, M Almeida, MJ Matos, RT Henriques, JA Wright, and SE Brown. Interaction of magnetic field-dependent peierls and spin-peierls ground states in (p e r) 2 [pt (m n t) 2]. *Physical Review B*, 84(12):121101, 2011.
- [90] Pasquale Calabrese and John Cardy. Entanglement entropy and quantum field theory. *Journal of Statistical Mechanics: Theory and Experiment*, 2004(06):P06002, 2004.

- [91] RT Henriques, L Alcacer, JP Pouget, and D Jérôme. Electrical conductivity and x-ray diffuse scattering study of the family of organic conductors (perylene)  $2m$  (mnt)  $2$ , ( $m = pt, pd, au$ ). *Journal of Physics C: Solid State Physics*, 17(29):5197, 1984.
- [92] RT Henriques, L Alcácer, D Jerome, C Bourbonnais, and C Weyl. Electrical conductivity of (perylene)  $2m$  (mnt)  $2$  ( $m = pt, au$ ) under pressure. *Journal of Physics C: Solid State Physics*, 19(24):4663, 1986.
- [93] C Bourbonnais, RT Henriques, P Wzietek, D Köngeter, J Voiron, and D Jérme. Nuclear and electronic resonance approaches to magnetic and lattice fluctuations in the two-chain family of organic compounds (perylene)  $2$  [ $m$  ( $s$   $2$   $c$   $2$  (cn)  $2$ )  $2$ ] ( $m = pt, au$ ). *Physical Review B*, 44(2):641, 1991.
- [94] Manuel Matos, Gregoire Bonfait, Rui T Henriques, and Manuel Almeida. Modification of the magnetic-field dependence of the peierls transition by a magnetic chain. *Physical Review B*, 54(21):15307, 1996.
- [95] V Gama, RT Henriques, G Bonfait, M Almeida, S Ravy, JP Pouget, and L Alcácer. The interplay between conduction electrons and chains of localised spins in the molecular metals (per)  $2m$  (mnt)  $2$ ,  $m = au, pt, pd, ni, cu, co$  and  $fe$ . *Molecular Crystals and Liquid Crystals Science and Technology. Section A. Molecular Crystals and Liquid Crystals*, 234(1):171–178, 1993.
- [96] G Bonfait, MJ Matos, RT Henriques, and M Almeida. Spin-peierls instability in per $2$  [ $m$  (mnt)  $2$ ] compounds probed by specific heat. *Le Journal de Physique IV*, 3(C2):C2–251, 1993.
- [97] Yakir Aharonov and David Bohm. Significance of electromagnetic potentials in the quantum theory. *Physical Review*, 115(3):485, 1959.

- [98] Daniel C Tsui, Horst L Stormer, and Arthur C Gossard. Two-dimensional magneto-transport in the extreme quantum limit. *Physical Review Letters*, 48(22):1559, 1982.
- [99] Robert B Laughlin. Anomalous quantum hall effect: an incompressible quantum fluid with fractionally charged excitations. *Physical Review Letters*, 50(18):1395, 1983.
- [100] Michael Levin and Xiao-Gang Wen. Detecting topological order in a ground state wave function. *Physical review letters*, 96(11):110405, 2006.
- [101] Alexei Kitaev and John Preskill. Topological entanglement entropy. *Physical review letters*, 96(11):110404, 2006.
- [102] T Senthil and O Motrunich. Microscopic models for fractionalized phases in strongly correlated systems. *Physical Review B*, 66(20):205104, 2002.
- [103] L. Balents, M. P. A. Fisher, and S. M. Girvin. Fractionalization in an easy-axis kagome antiferromagnet. *Phys. Rev. B*, 65:224412, May 2002.
- [104] D N Sheng and Leon Balents. Numerical evidences of fractionalization in an easy-axis two-spin heisenberg antiferromagnet. *Physical review letters*, 94(14):146805, 2005.
- [105] V Kalmeyer and R B Laughlin. Equivalence of the resonating-valence-bond and fractional quantum hall states. *Physical Review Letters*, 59(18):2095, 1987.
- [106] Shou Shu Gong, Wei Zhu, and D N Sheng. Emergent chiral spin liquid: Fractional quantum hall effect in a kagome heisenberg model. *Scientific reports*, 4:6317, 2014.
- [107] Bela Bauer, Lukasz Cincio, Brendan P Keller, Michele Dolfi, Guifre Vidal, Simon Trebst, and Andreas W W Ludwig. Chiral spin liquid and emergent anyons in a kagome lattice mott insulator. *Nature communications*, 5:5137, 2014.

- [108] Alexander Wietek, Antoine Sterdyniak, and Andreas M Läuchli. Nature of chiral spin liquids on the kagome lattice. *Physical Review B*, 92(12):125122, 2015.
- [109] Yin-Chen He, D N Sheng, and Yan Chen. Chiral spin liquid in a frustrated anisotropic kagome heisenberg model. *Physical review letters*, 112(13):137202, 2014.
- [110] W Zhu, S S Gong, and D N Sheng. Chiral and critical spin liquids in a spin-1 2 kagome antiferromagnet. *Physical Review B*, 92(1):014424, 2015.
- [111] Pierre Nataf, Miklós Lajkó, Alexander Wietek, Karlo Penc, Frédéric Mila, and Andreas M Läuchli. Chiral spin liquids in triangular-lattice su (n) fermionic mott insulators with artificial gauge fields. *Physical review letters*, 117(16):167202, 2016.
- [112] Shou-Shu Gong, W. Zhu, J.-X. Zhu, D. N. Sheng, and Kun Yang. Global phase diagram and quantum spin liquids in a spin- $\frac{1}{2}$  triangular antiferromagnet. *Phys. Rev. B*, 96:075116, Aug 2017.
- [113] Shou-Shu Gong, Wayne Zheng, Mac Lee, Yuan-Ming Lu, and D. N. Sheng. Chiral spin liquid with spinon fermi surfaces in the spin- $\frac{1}{2}$  triangular heisenberg model. *Phys. Rev. B*, 100:241111(R), Dec 2019.
- [114] Anne EB Nielsen, Germán Sierra, and J Ignacio Cirac. Local models of fractional quantum hall states in lattices and physical implementation. *Nature communications*, 4:2864, 2013.
- [115] Ji-Yao Chen, Laurens Vanderstraeten, Sylvain Capponi, and Didier Poilblanc. Non-abelian chiral spin liquid in a quantum antiferromagnet revealed by an ipeps study. *Phys. Rev. B*, 98:184409, Nov 2018.
- [116] Ciarán Hickey, Lukasz Cincio, Zlatko Papić, and Arun Paramekanti. Haldane-hubbard

- mott insulator: from tetrahedral spin crystal to chiral spin liquid. *Physical review letters*, 116(13):137202, 2016.
- [117] Tigran A Sedrakyan, Leonid I Glazman, and Alex Kamenev. Spontaneous formation of a nonuniform chiral spin liquid in a moat-band lattice. *Physical review letters*, 114(3):037203, 2015.
- [118] Rui Wang, Baigeng Wang, and Tigran A Sedrakyan. Chern-simons fermionization approach to two-dimensional quantum magnets: Implications for antiferromagnetic magnons and unconventional quantum phase transitions. *Physical Review B*, 98(6):064402, 2018.
- [119] Christopher N Varney, Kai Sun, Victor Galitski, and Marcos Rigol. Kaleidoscope of exotic quantum phases in a frustrated  $x y$  model. *Physical review letters*, 107(7):077201, 2011.
- [120] Juan Carrasquilla, Andrea Di Ciolo, Federico Becca, Victor Galitski, and Marcos Rigol. Nature of the phases in the frustrated  $x y$  model on the honeycomb lattice. *Physical Review B*, 88(24):241109(R), 2013.
- [121] Andrea Di Ciolo, Juan Carrasquilla, Federico Becca, Marcos Rigol, and Victor Galitski. Spiral antiferromagnets beyond the spin-wave approximation: Frustrated  $x y$  and heisenberg models on the honeycomb lattice. *Physical Review B*, 89(9):094413, 2014.
- [122] P H Y Li, R F Bishop, and Charles E Campbell. Phase diagram of a frustrated spin-1  $2 j 1-j 2 x x z$  model on the honeycomb lattice. *Physical Review B*, 89(22):220408(R), 2014.
- [123] Zhenyue Zhu and Steven R White. Quantum phases of the frustrated  $xy$  models on the honeycomb lattice. *Modern Physics Letters B*, 28(31):1430016, 2014.

- [124] Jaan Oitmaa and Rajiv R P Singh. Phase diagram of the frustrated quantum-x y model on the honeycomb lattice studied by series expansions: Evidence for proximity to a bicritical point. *Physical Review B*, 89(10):104423, 2014.
- [125] R F Bishop, P H Y Li, and Charles E Campbell. Frustrated spin-1/2 j<sub>1</sub>-j<sub>2</sub> isotropic x y model on the honeycomb lattice. *Physical Review B*, 89(21):214413, 2014.
- [126] Christopher N Varney, Kai Sun, Victor Galitski, and Marcos Rigol. Quantum phases of hard-core bosons in a frustrated honeycomb lattice. *New Journal of Physics*, 14(11):115028, 2012.
- [127] Takashi Nakafuji and Ikuo Ichinose. Phase diagrams of bose-hubbard model and antiferromagnetic spin-1/2 models on a honeycomb lattice. *Physical Review A*, 96(1):013628, 2017.
- [128] D N Sheng, Olexei I Motrunich, and Matthew P A Fisher. Spin bose-metal phase in a spin-1/2 model with ring exchange on a two-leg triangular strip. *Physical Review B*, 79(20):205112, 2009.
- [129] Kirill Plekhanov, Ivana Vasić, Alexandru Petrescu, Rajbir Nirwan, Guillaume Roux, Walter Hofstetter, and Karyn Le Hur. Emergent chiral spin state in the mott phase of a bosonic kane-mele-hubbard model. *Physical review letters*, 120(15):157201, 2018.
- [130] Yixuan Huang, Xiao-yu Dong, DN Sheng, and CS Ting. Global phase diagram and chiral spin liquids in the extended spin- $\frac{1}{2}$  honeycomb xy model. *arXiv preprint arXiv:1912.11156*, 2019.
- [131] Johannes Hauschild and Frank Pollmann. Efficient numerical simulations with Tensor Networks: Tensor Network Python (TeNPy). *SciPost Phys. Lect. Notes*, page 5, 2018. Code available from <https://github.com/tenpy/tenpy>.

- [132] Olexei I Motrunich. Orbital magnetic field effects in spin liquid with spinon fermi sea: Possible application to  $\kappa$ -(et)  $2\text{Cu}_2(\text{CN})_3$ . *Physical Review B*, 73(15):155115, 2006.
- [133] Ciarán Hickey, Lukasz Cincio, Zlatko Papić, and Arun Paramekanti. Emergence of chiral spin liquids via quantum melting of noncoplanar magnetic orders. *Physical Review B*, 96(11):115115, 2017.
- [134] Yin-Chen He, D N Sheng, and Yan Chen. Obtaining topological degenerate ground states by the density matrix renormalization group. *Physical Review B*, 89(7):075110, 2014.
- [135] Xiao-Liang Qi, Hosho Katsura, and Andreas W W Ludwig. General relationship between the entanglement spectrum and the edge state spectrum of topological quantum states. *Physical review letters*, 108(19):196402, 2012.
- [136] Frank Pollmann and Ari M. Turner. Detection of symmetry-protected topological phases in one dimension. *Phys. Rev. B*, 86:125441, Sep 2012.
- [137] L. Cincio and G. Vidal. Characterizing topological order by studying the ground states on an infinite cylinder. *Phys. Rev. Lett.*, 110:067208, Feb 2013.
- [138] Nobuyuki Ishibashi. The boundary and crosscap states in conformal field theories. *Modern Physics Letters A*, 4(03):251–264, 1989.
- [139] Philippe Francesco, Pierre Mathieu, and David Sénéchal. *Conformal field theory*. Springer Science & Business Media, 2012.
- [140] Xiao-Gang Wen. Chiral luttinger liquid and the edge excitations in the fractional quantum hall states. *Physical Review B*, 41(18):12838, 1990.

- [141] S Nakatsuji, K Kuga, K Kimura, R Satake, N Katayama, E Nishibori, H Sawa, R Ishii, M Hagiwara, F Bridges, et al. Spin-orbital short-range order on a honeycomb-based lattice. *Science*, 336(6081):559–563, 2012.
- [142] J. G. Cheng, G. Li, L. Balicas, J. S. Zhou, J. B. Goodenough, Cenke Xu, and H. D. Zhou. High-pressure sequence of  $\text{Ba}_3\text{NiSb}_2\text{O}_9$  structural phases: New  $s = 1$  quantum spin liquids based on  $\text{Ni}^{2+}$ . *Phys. Rev. Lett.*, 107:197204, Nov 2011.
- [143] J. A. Quilliam, F. Bert, A. Manseau, C. Darie, C. Guillot-Deudon, C. Payen, C. Baines, A. Amato, and P. Mendels. Gapless quantum spin liquid ground state in the spin-1 antiferromagnet  $\text{6hb-Ba}_3\text{NiSb}_2\text{O}_9$ . *Phys. Rev. B*, 93:214432, Jun 2016.
- [144] Hari Krishnan S Nair, J M Brown, E Coldren, G Hester, M P Gelfand, A Podlesnyak, Q Huang, and K A Ross. Short-range order in the quantum xxz honeycomb lattice material  $\text{BaCo}_2(\text{PO}_4)_2$ . *Physical Review B*, 97(13):134409, 2018.
- [145] Ruidan Zhong, Mimi Chung, Tai Kong, Loi T Nguyen, Shiming Lei, and Robert Joseph Cava. Field-induced spin-liquid-like state in a magnetic honeycomb lattice. *Physical Review B*, 98(22):220407(R), 2018.
- [146] Ruidan Zhong, Tong Gao, Nai Phuan Ong, and Robert J Cava. Weak-field induced nonmagnetic state in a co-based honeycomb. *arXiv preprint arXiv:1910.08577*, 2019.
- [147] Nathan Goldman, Jan Carl Budich, and Peter Zoller. Topological quantum matter with ultracold gases in optical lattices. *Nature Physics*, 12(7):639–645, 2016.
- [148] Monika Aidelsburger, Michael Lohse, Christian Schweizer, Marcos Atala, Julio T Barreiro, Sylvain Nascimbène, NR Cooper, Immanuel Bloch, and Nathan Goldman. Measuring the chern number of hofstadter bands with ultracold bosonic atoms. *Nature Physics*, 11(2):162, 2015.

- [149] Charles L Kane and Eugene J Mele. Quantum spin hall effect in graphene. *Physical review letters*, 95(22):226801, 2005.
- [150] JMB Lopes Dos Santos, NMR Peres, and AH Castro Neto. Graphene bilayer with a twist: Electronic structure. *Physical review letters*, 99(25):256802, 2007.
- [151] G Trambly de Laissardière, Didier Mayou, and Laurence Magaud. Localization of dirac electrons in rotated graphene bilayers. *Nano letters*, 10(3):804–808, 2010.
- [152] Rafi Bistritzer and Allan H MacDonald. Moiré bands in twisted double-layer graphene. *Proceedings of the National Academy of Sciences*, 108(30):12233–12237, 2011.
- [153] Yuan Cao, Valla Fatemi, Shiang Fang, Kenji Watanabe, Takashi Taniguchi, Efthimios Kaxiras, and Pablo Jarillo-Herrero. Unconventional superconductivity in magic-angle graphene superlattices. *Nature*, 556(7699):43–50, 2018.
- [154] Yuan Cao, Valla Fatemi, Ahmet Demir, Shiang Fang, Spencer L Tomarken, Jason Y Luo, Javier D Sanchez-Yamagishi, Kenji Watanabe, Takashi Taniguchi, Efthimios Kaxiras, et al. Correlated insulator behaviour at half-filling in magic-angle graphene superlattices. *Nature*, 556(7699):80, 2018.
- [155] Xiaobo Lu, Petr Stepanov, Wei Yang, Ming Xie, Mohammed Ali Aamir, Ipsita Das, Carles Urgell, Kenji Watanabe, Takashi Taniguchi, Guangyu Zhang, et al. Superconductors, orbital magnets and correlated states in magic-angle bilayer graphene. *Nature*, 574(7780):653–657, 2019.
- [156] Aaron L Sharpe, Eli J Fox, Arthur W Barnard, Joe Finney, Kenji Watanabe, Takashi Taniguchi, MA Kastner, and David Goldhaber-Gordon. Emergent ferromagnetism near three-quarters filling in twisted bilayer graphene. *Science*, 365(6453):605–608, 2019.

- [157] Matthew Yankowitz, Shaowen Chen, Hryhorii Polshyn, Yuxuan Zhang, K Watanabe, T Taniguchi, David Graf, Andrea F Young, and Cory R Dean. Tuning superconductivity in twisted bilayer graphene. *Science*, 363(6431):1059–1064, 2019.
- [158] Jian Kang and Oskar Vafek. Symmetry, maximally localized wannier states, and a low-energy model for twisted bilayer graphene narrow bands. *Physical Review X*, 8(3):031088, 2018.
- [159] Mikito Koshino, Noah FQ Yuan, Takashi Koretsune, Masayuki Ochi, Kazuhiko Kuroki, and Liang Fu. Maximally localized wannier orbitals and the extended hubbard model for twisted bilayer graphene. *Physical Review X*, 8(3):031087, 2018.
- [160] Yixuan Huang, Pavan Hosur, and Hridis K. Pal. Deconstructing magic-angle physics in twisted bilayer graphene with a two-leg ladder model. *arXiv preprint arXiv:2004.10325*, 2020.
- [161] Hridis K Pal, Steven Carter, and M Kindermann. Theory of twisted bilayer graphene near commensuration. *arXiv preprint arXiv:1409.1971*, 2014.
- [162] Ai A Abrikosov and L Pr Gor'kov. Contribution to the theory of superconducting alloys with paramagnetic impurities. *Zhur. Eksptl'. i Teoret. Fiz.*, 39, 1960.
- [163] YU LU. Bound state in superconductors with paramagnetic impurities. *Acta Physica Sinica*, 21(1):75, 1965.
- [164] Hiroyuki Shiba. Classical spins in superconductors. *Prog. Theor. Phys.*, 40(3):435–451, 1968.
- [165] A.I. Rusinov. On the theory of gapless superconductivity in alloys containing paramagnetic impurities. *JETP*, 29(6):1101, 1969.

- [166] A. V. Balatsky, I. Vekhter, and Jian-Xin Zhu. Impurity-induced states in conventional and unconventional superconductors. *Rev. Mod. Phys.*, 78:373–433, May 2006.
- [167] Ali Yazdani, B. A. Jones, C. P. Lutz, M. F. Crommie, and D. M. Eigler. Probing the local effects of magnetic impurities on superconductivity. *Science*, 275(5307):1767–1770, 1997.
- [168] Jun Kondo. Resistance minimum in dilute magnetic alloys. *Prog. Theor. Phys.*, 32(1):37–49, 1964.
- [169] Osamu Sakai, Yukihiro Shimizu, Hiroyuki Shiba, and Koji Satori. Numerical renormalization group study of magnetic impurities in superconductors. ii. dynamical excitation spectra and spatial variation of the order parameter. *Journal of the Physical Society of Japan*, 62(9):3181–3197, 1993.
- [170] Koji Satori, Hiroyuki Shiba, Osamu Sakai, and Yukihiro Shimizu. Numerical renormalization group study of magnetic impurities in superconductors. *Journal of the Physical Society of Japan*, 61(9):3239–3254, 1992.
- [171] Hong-Chen Jiang and Thomas P Devereaux. Superconductivity in the doped hubbard model and its interplay with next-nearest hopping  $t$ . *Science*, 365(6460):1424–1428, 2019.
- [172] Jian Kang and Oskar Vafek. Strong coupling phases of partially filled twisted bilayer graphene narrow bands. *Physical review letters*, 122(24):246401, 2019.
- [173] Masayuki Ochi, Mikito Koshino, and Kazuhiko Kuroki. Possible correlated insulating states in magic-angle twisted bilayer graphene under strongly competing interactions. *Physical Review B*, 98(8):081102, 2018.

- [174] Tongyun Huang, Lufeng Zhang, and Tianxing Ma. Antiferromagnetically ordered mott insulator and d+ id superconductivity in twisted bilayer graphene: A quantum monte carlo study. *Science Bulletin*, 64(5):310–314, 2019.